UNIVERSITY OF CALIFORNIA SAN DIEGO

On atmospheric turbidity, radiative cloud enhancement, and evaporation at very low Rayleigh numbers

A dissertation submitted in partial satisfaction of the
requirements for the degree
Doctor of Philosophy

in

Engineering Sciences (Aerospace Engineering)

by

Richard Headen Inman

Committee in charge:

Professor Carlos F. M. Coimbra, Chair
Professor Jennifer Burney
Professor Renkun Chen
Professor Jan Kleissl

2022

The dissertation of Richard Headen Inman is approved, and it is acceptable in quality and form for publication on microfilm and electronically.

University of California San Diego

2022

DEDICATION

To Whitney

For your unconditional patience and loving support.

EPIGRAPH

Sometimes it's the detours

which turn out to be the fruitful ideas.

—Roger Penrose

The first principle is that you must not fool yourself;

and you are the easiest person to fool.

—Richard Feynman

The human brain has 100 billion neurons,

each neuron connected to 10 thousand other neurons.

Sitting on your shoulders is the most complicated

object in the known universe.

—Michio Kaku

Prediction is very difficult, especially if it's about the future.

—Niels Bohr[1]

[1]The fourth volume of the multi-volume autobiography by Danish politician Karl Kristian Steincke titled "Farvel Og Tak" ("Goodbye and Thanks") [1] contains the earliest known reference to this quote. The proverb appeared in a section titled "Og saa til Slut et Par parlamentariske Sprogblomster" ("And finally a couple of parliamentary howlers") as: "*Det er vanskeligt at spaa, især naar det gælder Fremtiden.*"

TABLE OF CONTENTS

LIST OF FIGURES

LIST OF TABLES

ACKNOWLEDGEMENTS

Foremost, I would like to thank my advisor, Professor Carlos F. M. Coimbra, for his support and guidance through each stage of my graduate education. Without his kind mentorship, enthusiasm for research, patience with students, engineering wisdom, and extensive knowledge, this dissertation would not be possible. I will always respect his integrity as a scientist and his ability to see potential in me. I fondly remember my time in his lab at UC San Diego and the countless hours of invaluable guidance and exciting discussions. He is a fantastic mentor, and I feel incredibly privileged for the opportunity to study under his supervision. In addition, I would like to acknowledge the rest of the committee: Profs Jan Kleissl, Renkun Chen, and Jennifer Burney for their collective feedback and constructive suggestions during the preparation of my dissertation.

I would also like to acknowledge the exceptional support and collaboration of previous and present research group members. Primarily I'd like to thank Jéssica P. T. Medrado for the many years of collaboration, data collection, and general persistence in research and problem-solving. I'd also like to recognize Dr. Hugo T. C. Pedro for always being willing to help and opportunities to learn from his experience. Thanks to Dr. David P. Larson, Dr. Mengying Li, Dr. Charlie Chu, Dr. Jeremy R. Orosco, Dr. Lukas Nonnenmacher, Dr. Aman Kaur, and Dr. Athanassios Zagouras for their participation in my research and helpful feedback during group meetings. I also must thank James G. Edson, Lucas Coêlho, and Alexandre Leonelli for their assistance during their time at UC San Diego.

Finally, I want to thank Professor Sayantani Ghosh for encouraging me to pursue research as an undergraduate and Lana Jordan for sparking my initial interest in physics and engineering. A special thanks to my loving mother, Rose Mary, for a beautiful job raising my brother and me, as well as her loving support, my late father Richard for his insightful guidance and persistence, and my younger brother Ryan for bringing me back down to Earth in the way only he can. My gratitude also belongs to my wife, Whitney, for her unconditional support and encouragement; I

could not have done this without you.

Portions of Chapter 1 are taken, in part, from R. H. Inman, H. T. C. Pedro, and C. F. M. Coimbra (2013) "Solar Forecasting Methods for Renewable Energy Integration," *Progress in Energy and Combustion Science* (39) pp. 535-576. The dissertation author is the first author of this publication.

Chapter 2, in full, is a reprint of R. H. Inman, J. G. Edson and C. F. M. Coimbra (2015) "Impact of Local Broadband Turbidity Estimation on Clear Sky Models for Direct Normal Irradiance," *Solar Energy* (117) pp. 125–138. The dissertation author is the first author of this publication.

Chapter 3, in full, is a reprint of R. H. Inman, Y. Chu, and C. F. M. Coimbra (2016) "Cloud Enhancement of Global Horizontal Irradiance in California and Hawaii," *Solar Energy* (130) pp. 128–138. The dissertation author is the first author of this publication.

Chapter 4, in full, is in preparation as a manuscript for publication with my co-author Jéssica P. T. Medrado and advisor Professor Carlos F. M. Coimbra. The dissertation author is also the first author of this paper.

VITA

2010	B. S. in Mechanical Engineering, University of California Merced.
2010	B. S. in Physics, University of California Merced.
2012	M. S. in Engineering Sciences (Aerospace Engineering) University of California, San Diego
2022	Ph. D. in Engineering Sciences (Aerospace Engineering), University of California San Diego

PUBLICATIONS

Y. K. Verma, R. H. Inman, C. G. L. Ferri, H. Mirafzal, S. N. Ghosh, D. F. Kelley, L. S. Hirst, S. Ghosh and W. C. Chin, "Electrical modulation of static and dynamic spectroscopic properties of coupled nanoscale GaSe quantum dot assemblies," *Physical Review B*, 82(16), 2010

L. S. Hirst, J. Kirchhoff, R. Inman and S. Ghosh, "Quantum dot self-assembly in liquid crystal media," *Proceedings of SPIE*, 7618, 2010

S. Ghosh, G. Shcherbatyuk, R. Inman and J. Clayton, "Nanostructured, luminescent solar concentrators" (invited article), *SPIE Newsroom: Solar and Alternative Energy*, 2010

G. V. Shcherbatyuk, R. H. Inman, R. Winston and S. Ghosh, "Design and performance of nanostructure-based luminescent solar concentrators ," *Proceedings of SPIE*, 7769, 2010

G. V. Shcherbatyuk, R. H. Inman, C. Wang, R. Winston and S. Ghosh, "Viability of using near infrared PbS quantum dots as active materials in luminescent solar concentrators ," *Applied Physics Letters*, 96, 191901, 2010

C. Wang, G. Shcherbatyuk, R. Inman, D. Pelka, W. Zhang, Y. Rodriguez, S. Carter, R. Winston and S. Ghosh, "Efficiency improvement by near infra red quantum dots for luminescent solar concentrators," *Proceedings of SPIE*, 7772, 7720G, 2010

R. H. Inman, G. V. Shcherbatyuk, D. Medvedko, A. Gopinathan and S. Ghosh, "Cylindrical luminescent solar concentrators with near-infrared quantum dots," *Optics express*, 19, 24, 24308, 2011

G. V. Shcherbatyuk, R. H. Inman and S. Ghosh, "Anomalous photo-induced spectral changes in CdSe/ZnS quantum dots," *Journal of Applied Physics*, 110, 053518, 2011

C. G. L. Ferri, R. H. Inman, B. Rich, A. Gopinathan, M. Khine and S. Ghosh, "Plasmon-induced enhancement of intra-ensemble FRET in quantum dots on wrinkled thin films," Optical Materials Express, 3, 383, 2013

R. H. Inman, H. T. C. Pedro and C. F. M. Coimbra, "Solar forecasting methods for renewable energy integration," *Progress in Energy and Combustion Science*, 39, 535-576, 2013

A. Zagouras, R. H. Inman and C. F. M. Coimbra,"On the determination of coherent solar microclimates for utility planning and operations," *Solar Energy*, 102, 173-188, 2014

Y. Chu, L. Nonnenmacher, R. H. Inman, Z. Liao, H. T. C. Pedro and C. F. M. Coimbra, "A Smart Image-Based Cloud Detection System for Intra-Hour Solar Irradiance Forecasts," *Journal of Atmospheric and Oceanic Technology*, 31 (9), 1995-2007, 2014

R. H. Inman, J. G. Edson and C. F. M. Coimbra, "Impact of local broadband turbidity estimation on clear sky models for direct normal irradiance," *Solar Energy*, 117, 125–138, 2015

R. H. Inman, Y. Chu and C. F. M. Coimbra, "Cloud Enhancement of global horizontal irradiance in California and Hawaii," *Solar Energy*, 130, 128–138, 2016

H. T. C. Pedro, R. H. Inman and C. F. M. Coimbra, "Mathematical Methods for Optimized Solar Forecasting, Chapter 4," *Renewable Energy Forecasting, Woodhead Publishing Series in Energy*, Elsevier, Editor: G. Kariniotakis, ISBN: 978-0-08-100504-0, 2017

J. P. T. Medrado, R. H. Inman, C. F. M. Coimbra, "Pool evaporation under low Grashof number downward convection," *International Journal of Heat and Mass Transfer*, 181, 122021, 2021

J. P. T. Medrado, R. H. Inman, C. F. M. Coimbra, "Isothermal and near-isothermal free evaporation of water from open tubes in air," *International Journal of Heat and Mass Transfer*, 189, 122687, 2022

ABSTRACT OF THE DISSERTATION

On atmospheric turbidity, radiative cloud enhancement, and evaporation at very low Rayleigh numbers

by

Richard Headen Inman

Doctor of Philosophy in Engineering Sciences (Aerospace Engineering)

University of California San Diego, 2022

Professor Carlos F. M. Coimbra, Chair

Clear-sky modeling is critical for the accurate determination of Direct Normal Irradiance (DNI), which is the relevant component of solar irradiance for concentrated solar energy applications. Accurate clear-sky modeling of DNI is typically best achieved through the separate consideration of water vapor and aerosol concentrations in the atmosphere. Highly resolved temporal measurements of such quantities are generally unavailable unless a meteorological station is close. When this type of data is not available, attenuating effects on the direct beam are modeled by Linke turbidity-equivalent factors, which can be obtained from broadband observations of DNI under cloudless skies. We present a novel algorithm that allows for a time-resolved estimation of

the average daily Linke turbidity factor from ground-based DNI observations under cloudless skies. This requires a method of identifying clear-sky periods in the observational time series (to avoid cloud contamination) and a broadband turbidity-based clear-sky model for implicit turbidity calculations. While the method can be applied to the correction of historical clear-sky models for a given site, the true value lies in DNI forecasting under cloudless skies through the assumption of persistence of average daily turbidity. This technique is applied at seven stations spread across California, Washington, and Hawaii while using several years of data from 2010 to 2014. Performance of the forecast is evaluated by way of the relative Root Mean Square Error (rRMSE) and relative Mean Bias Error (rMBE), both as a function of solar zenith angle, and benchmarked against monthly climatologies of turbidity information. Results suggest that rRMSE and rMBE of the method are typically smaller than 5% for both historical and forecasted CSMs, which compare favorably against the 10–20% range that is typical for monthly climatologies.

Clouds significantly attenuate ground-level solar irradiance causing a substantial reduction in photovoltaic power output capacity. However, partly cloudy skies may temporarily enhance local Global Horizontal Irradiance (GHI) above the clear-sky ceiling and, at times, the extraterrestrial irradiance. Such enhancements are referred to here as Cloud Enhancement Events (CEEs). In this work, we study these CEEs and quantitatively assess the occurrence of resulting coherent Ramp Rates (RRs). We analyze a full year of ground irradiance data recorded at the University of California, Merced, as well as nearly five months of irradiance data recorded at the University of California, San Diego, and Ewa Beach, Hawaii. Our analysis shows that approximately 4% of the data points qualify as potential CEEs, which corresponds to nearly 3.5 full days of such events per year if considered sequentially. The surplus irradiance enhancements range from 18 W m^{-2} day^{-1} to 73 W m^{-2} day^{-1}. The maximum recorded GHI of 1,400 W m^{-2} occurred in San Diego on May 25, 2012, nearly 43% higher than the modeled clear-sky ceiling. Wavelet decomposition coupled with fluctuation power index analysis shed light on the time scales on cloud-induced variability and CEEs. Results suggest that while cloud fields tend to generate variability most

strongly at the 30 min time scale, they have the potential to cause CEEs that influence variability on time scales of several minutes. This analysis demonstrates that CEEs are indicators for periods of high variability and therefore provide helpful information for solar forecasting and integration.

Finally, we report on experimental results for natural convection evaporation from a free surface of water into air at low Rayleigh numbers. Experiments were performed for air maintained between 285 K and 310 K, water surface temperatures ranging from 284-308 K, and relative humidity (RH) values ranging from 15-85%. During an experiment, no external heat was added to the liquid requiring the ambient to provide the energy required for evaporation. A geometry-independent length scale is employed, and we compare results to various other geometries and conditions. The combination of parameters (length scale, temperature, and relative humidity) results in Rayleigh numbers near zero (both positive and negative). Rayleigh numbers near zero have historically been challenging to measure because the driving potentials are relatively small, and several transfer mechanisms are of comparable magnitudes resulting in transfer rates that are generally unstable. Empirical results suggest that two distinct flow regimes exist, which we attribute to the presence or absence of a dominant recirculation zone over the evaporative pool. These distinct flow regimes can be accurately described by the following simple correlation. When a recirculation zone exists the correlation is

$$Sh_{\mathscr{L}} = 0.179\left(Ra_{\mathscr{L}} + 52.5\right)^{1/2},$$

and in the absence of a recirculation zone, the correlation is

$$Sh_{\mathscr{L}} = 0.206\left(Ra_{\mathscr{L}} + 55.3\right)^{1/2},$$

where $\mathscr{L} = A/P$. A discussion on the effect of flow recirculation zones that lead to the bifurcation of the Sherwood number correlations above is also presented.

Chapter 1

Introduction

1.1 Solar forecasting as an enabling technology

The global demand for renewable energy integration to the power grids highlights the importance of economic and technological issues associated with growing levels of flat-panel PhotoVoltaic (PV), Concentrated Solar Power (CSP), and Concentrated PV (CPV) penetrations into the power grid. These concerns arise from the variable nature of the solar resource, seasonal deviations in production and load profiles, the high cost of energy storage, and the balance between grid flexibility and reliability [7]. As a result, solar plant operators typically install ancillary generators as a backup for periods of high solar variability, which increases solar generation's capital and operational costs. Accurate solar forecasts over several time horizons are required so that Independent System Operators (ISOs) or equivalent grid balancing authorities can successfully integrate increased solar power production levels while maintaining reliability [7]. Solar forecasts on multiple time horizons become increasingly relevant as solar penetration increases for grid regulation, load-following production, power scheduling, and unit commitment. Short-term, intra-hour solar forecasts benefit power plant operations, grid balancing, real-time unit dispatching, automatic generation control (AGC), and trading. For more extended time horizons,

forecasts are of interest to utilities and ISOs for unit commitment, scheduling, and improving balance area control performance.Ultimately, a spectrum of solar forecasts is required to address the planning, operational, and balancing needs of both the distribution and the transmission grids, see Fig. 1.1. As a result, solar forecasting is a technology that enables an ever-increasing level of solar penetration into the grid because it improves the quality of the energy delivered to the grid and reduces the ancillary costs associated with weather dependency. The combination of increased renewable energy quality and reduced integration costs enabled by solar forecasting has been the driving motivation for developing a complex field of research. This research aims at producing better solar forecasting capabilities for the solar resource at the ground level and for the power output from different solar technologies that depend on the variable irradiance at the ground level. Solar, wind, and load forecasting have become integral parts of the so-called 'smart grid concept'.

To date, high-fidelity, robust solar forecast systems that work for widely different micro-climates remain evasive. The problem is of great complexity due to cloud motion's non-linear and chaotic relationship to solar irradiance at the ground level. However, the recent literature contains several promising approaches, and the incipient research field of solar meteorology for renewable energy generation has grown considerably by aggregating diverse areas of knowledge such as atmospheric physics, solar instrumentation, machine learning, forecasting theory, and remote sensing in its quest to increase predictive skills. According to a review published by a group of domain experts [8] (five associate/subject editors of Solar Energy), amongst various top papers, the review paper by Inman et al. [7] received the most citations (536 as of March 2022 according to the Web of Science [9]), and reading this review would be a good starting point for any scientist willing to research solar forecasting. This review presents an overview of the forecasting methods for solar resourcing and power generation and the theoretical basis for the most promising methods, followed by a discussion of their applications and effectiveness in operational use and serves as the basis of the work in what follows.

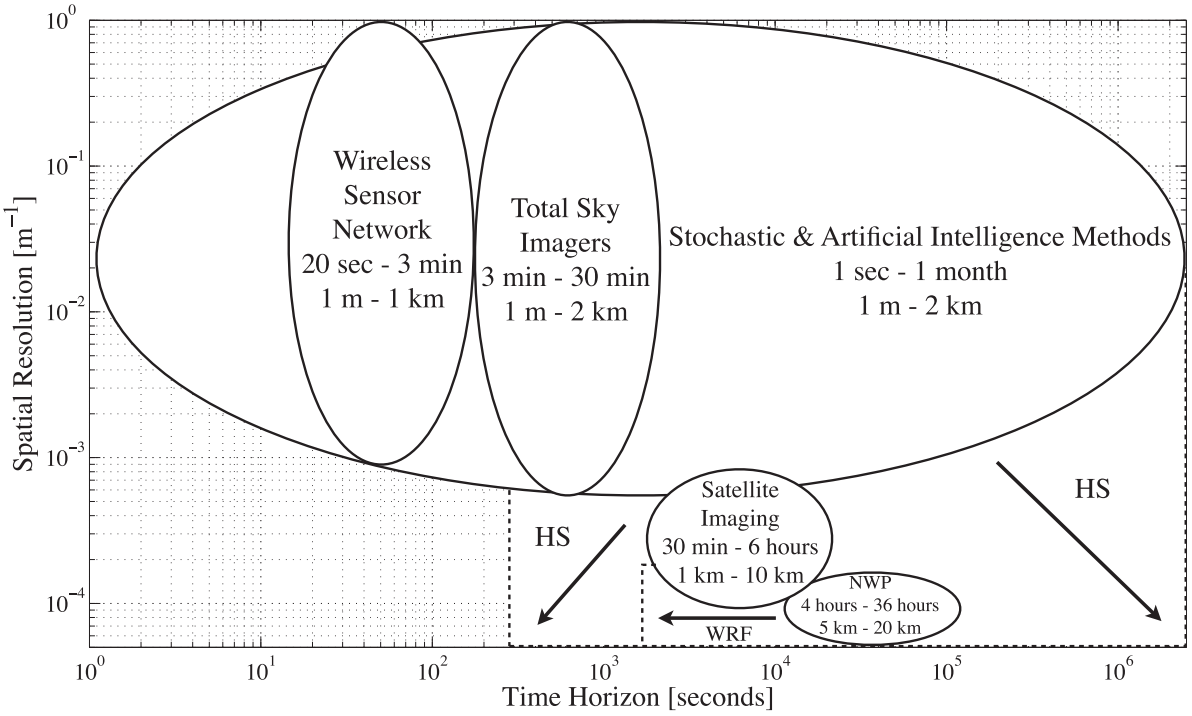

Figure 1.1: Comparison of time horizon and spatial resolution for solar forecasting approaches. Solid lines indicate current limits of techniques, while the dashed lines and arrows indicate the future progress of work. Artificial Intelligence (AI) techniques will continue to include local, mesoscale, and global meteorological data, allowing shorter time horizons and greater areas of interest. In addition, recent trends in Numerical Weather Predictions (NWP) suggest that shorter time horizons will be available through the development of the WRF models. Adapted, with permission, from [7].

1.2 Local clear sky model inputs

As discussed in the review by Inman et al. [7] local cloud cover results in a stochastic variability in ground-level solar irradiance, which, in general, drives forecast uncertainties. However, it is well known that, under cloudless skies, aerosol particles and water vapor become the most critical factors influencing the intensity of ground-level DNI [10, 11]. The literature refers to a cloudless sky as a "clear-sky," and many solar irradiance forecasting techniques employ so-called *clear-sky models* (CSMs) to estimate the attenuation of extraterrestrial solar irradiance resulting from aerosol particles suspended in the atmosphere and atmospheric water vapor content. Typically, these CSMs depend on one of several Radiative Transfer Models (RTMs) and require local meteorological inputs such as ozone and water vapor content or Linke turbidity in conjunction with solar geometry as inputs. A summary of the most widely used models can be found in the review by Inman et al. [7].

These models are scientifically sound; however, like any model, their accuracy is inversely proportional to the magnitude of the input data errors. In sparse data environments, where local telemetry of atmospheric data or solar irradiance data is not available, solar engineers typically reference global maps of monthly or seasonal variations in meteorological data generated from remote sensing, see, for example, [3, 12, 13], and Fig. 2.3. While these meteorological maps' monthly/seasonal resolution is convenient for most solar resourcing activities, local conditions frequently deviate from historical averages in both space and time, see Fig 2.4. These deviations in local meteorological properties from their expectation values introduce uncertainties that, in turn, tend to impact operational strategies negatively. In particular, these deviations in local conditions significantly increase uncertainties of CSMs for DNI, which depend strongly on atmospheric water vapor content and aerosol loading. Furthermore, when the power production technology depends strongly on DNI, such as CSP, these errors may be critical to optimal operational strategies for plant managers. The Ivanpah Solar Electric Generating System (ISEGS), a CSP plant with a

gross capacity of 392 MW, located in California's Mojave Desert, is one such example of a large CSP plant that would benefit from improvements in CSM models for DNI [14].

Let us consider an example to illustrate. Frequently, solar power farm designs, including that of the ISEGS, include carbon fuel-based generators to offset variability in DNI and improve plant operation economics. Suppose, however, forecasts predict reduced irradiance shortly after sunrise due to increased atmospheric turbidity or morning clouds, followed by relatively cloudless skies for the remainder of daylight hours. In that case, operators of CSP plants may opt to dispatch these carbon-based generators shortly after sunrise to ramp up the plant's production. Contrastingly, policy predominantly incentivizes plant operators to minimize carbon-based fuel consumption at renewable power plants. Moreover, the impact of atmospheric turbidity on DNI is most significant shortly after sunrise and before sunset, when the airmass is near $\pi/2$ (90°). Therefore, increases in the accuracy of DNI estimation in the early daylight hours allow operators to make better-informed decisions regarding fossil fuel dispatch, which reduces operational expenses. The previous example is just one of many ways reduced uncertainty in local atmospheric turbidity can help make CSP plants more profitable to operate. However, this approach nevertheless requires some method of estimating local atmospheric turbidity.

Fortunately, operators typically outfit solar power plants, such as ISEGS, with pyranometers and pyrheliometers on trackers to directly measure GHI and DNI, respectively, or else, pyranometers and pyranometers outfitted with shade kits for direct measurement of GHI and indirect calculation of DNI, respectively. Assuming plant operators calibrate these irradiance sensors correctly, the local observation of DNI when clouds do not obscure the circumsolar region allows for the estimation of bulk atmospheric turbidity indexes, such as Linke turbidity, through the inversion of any CSM for DNI based on such a bulk index. This technique allows for a much higher sampling of atmospheric turbidity than relying on historical averages or remote telemetry, see Appendix A. Ultimately, suppose plant operators can identify when clouds do not obscure the circumsolar region. In that case, DNI observations during these times provide local estimates of

atmospheric turbidity that operators can use to reduce forecasting uncertainties and, as a result, improve operational strategies.

The first chapter of this dissertation presents a novel algorithm that allows for a time-resolved estimation of the average daily Linke turbidity factor from ground-based DNI observations when clouds do not obscure the circumsolar region. The algorithm uses a filter to identify periods in observational time-series when clouds do not obscure the circumsolar region. The algorithm then uses periods of observational data that pass through this filter to estimate local atmospheric turbidity implicitly through the inversion of a turbidity-based CSM for DNI. While this method can reduce errors in CSMs for DNI at a given site, the actual value lies in forecasting DNI under cloudless skies through the assumption of persistence of average daily turbidity. We present results from this algorithm for several years of data from 2010 to 2014 from seven stations spread across California, Washington, and Hawaii. We evaluate the performance of the forecast by way of the relative Root Mean Square Error (rRMSE) and relative Mean Bias Error (rMBE), both as a function of solar zenith angle, and benchmark against monthly climatologies of turbidity. Results suggest that rRMSE and rMBE of the proposed method are typically smaller than 5% for historical and forecasted CSMs, which compare favorably against the typical 10-20% range for monthly climatologies.

1.3 The interpretability of model parameters

The previous discussion regarding the sampling of DNI when clouds do not obscure the circumsolar region naturally implies that there are times when clouds *do* obscure the circumsolar region. Indeed, solar forecasting technologies' primary focus is to predict the stochastic variability in ground-level solar irradiance induced by clouds during these non-clear periods, to which we previously alluded. Moreover, the literature contains numerous techniques scientists have employed for solar forecasting, and, for further details, readers are referred to the review by Inman

et al. [7], which discusses the following six classes of solar forecasting: (1) regressive methods; (2) artificial intelligence techniques, also known as machine learning; (3) remote sensing models; (4) numerical weather prediction; (5) local sensing; and (6) hybrid systems. More recently, the review by Yang et al. [8] classified solar forecasting methods based on frequently-used abbreviations into the following five groups: (1) time series: (2) regression; (3) numerical weather prediction; (4) machine learning; and (5) image-based forecasting. While each of these classes of forecasting span a particular spatial resolution and typical forecast horizon, see Fig. 1.1, the review by Yang et al. [8] concluded that machine learning (ML) is perhaps the most widespread approach in solar forecasting. The authors attribute machine learning's popularity in solar forecasting to its wide range of available methods, including supervised learning (classification and regression) and unsupervised learning (clustering). Moreover, machine learning also supports a large number of applications and variants, including, but not limited to, consensus learning, fuzzy logic, gradient boosted regression, hidden Markov models, k-nearest neighbor, random forest, support vector machines, support vector regression, evolutionary algorithms, and artificial neural networks.

Although these applications are various, the concept of learning patterns and model parameters from the data, where learning indicates classification, regression, and prediction, is at the core of all machine learning algorithms [8]. While these machine learning techniques are well suited to solar forecasting, which consists of creating predictive models based on historical data, machine learning model definitions typically contain numerous parameters and configuration hyper-parameters that must be optimized, rendering the training of such models a computationally intensive task [15]. In addition, this complexity, explicitly the many learnable parameters, makes it difficult for practitioners of machine learning models to understand and articulate the relationships between a model's predictors (parameters) and its output. This measure of a human's ability to determine how a model arrives at its predictions is referred to as the model's *interpretability*. In the case of linear models, which are highly interpretable, these relationships are evident directly in the model coefficients. However, for modern machine learning models, which are less

interpretable, additional advanced techniques must be overlaid to understand these relationships. To demonstrate, let us examine a popular machine learning technique, the feed-forward ANN, or multi-layer perceptron, applied to one of the most straightforward of non-linear problems, the XOR operator, which linear partitioning cannot solve, see Fig. 1.2 and Fig. 1.3.

The rules for the XOR operator are, given an input,

$$\vec{x} = \begin{bmatrix} x_1, & x_2 \end{bmatrix} \tag{1.1}$$

where,

$$x_1 \in \{0,1\} \quad \text{and} \quad x_2 \in \{0,1\}, \tag{1.2}$$

the resulting output Z also satisfies,

$$Z \in \{0,1\}, \tag{1.3}$$

such that,

$$Z = 0 \quad \text{if} \quad x_1 = x_2 \quad \text{else} \quad Z = 1. \tag{1.4}$$

Since the XOR problem is not linearly partitionable, see Fig. 1.2, an artificial neural network capable of successfully partitioning the solution space would require a minimum of one hidden layer with a non-linear activation function; more information regarding commonly used activation functions and their derivatives can be found in [7]. As we will see, this hidden layer in the XOR regressor results in a minimum of nine parameters to be tuned, see Fig. 1.3. Specifically, four weights for the hidden layer and two weights for the output layer,

$$\mathbf{W}^{(1)} = \begin{bmatrix} w_{11}^{(1)} & w_{12}^{(1)} \\ w_{21}^{(1)} & w_{22}^{(1)} \end{bmatrix} \quad \text{and} \quad \mathbf{W}^{(2)} = \begin{bmatrix} w_{11}^{(2)} \\ w_{21}^{(2)} \end{bmatrix} \tag{1.5}$$

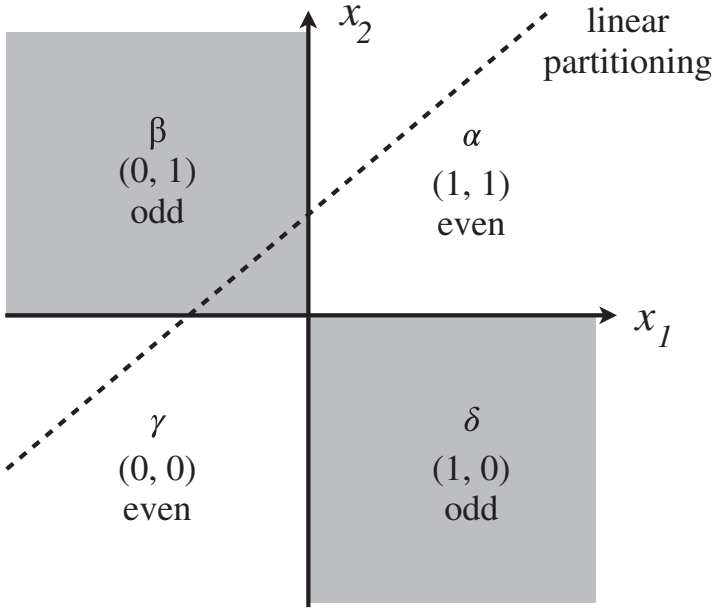

State	Quadrant	Inputs		Output z	Parity
		x_1	x_2		
α	1	1	1	0	Even
β	2	0	1	1	Odd
γ	3	0	0	0	Even
δ	4	1	0	1	Odd

$(x_1 \text{ or } x_2) \cap (\overline{x}_1 \text{ or } \overline{x}_2)$, where $\overline{x} \equiv \text{not}(x)$.

Figure 1.2: Illustrating the XOR problem visually and systematically. The top portion of the figure shows a visual representation of the XOR and illustrates that linear partitioning cannot sufficiently partition the solution space. The lower portion of the figure shows the XOR state table and denotes the state, quadrant, associated inputs, output, and parity. Reproduced, with permission, from [7].

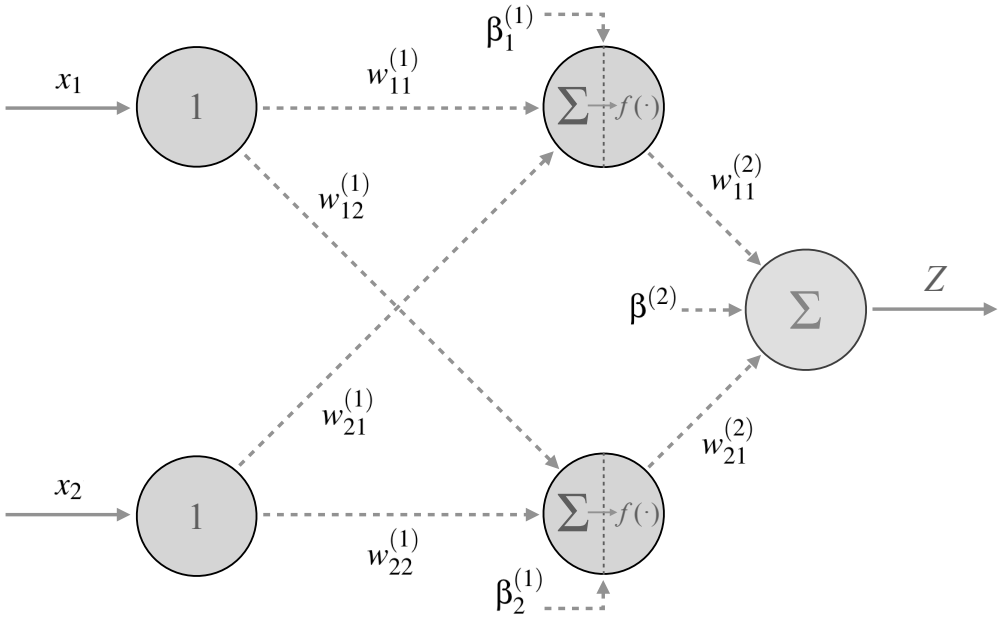

Figure 1.3: Depicting the multi-layer perceptron ANN applied to the non-linear XOR problem. The following variables are indicated in the diagram: input variables x_i, weights between neurons in each layer $x_{i,j}^{(\ell)}$, biases for neurons in each layer $\beta_i^{(\ell)}$, and the output Z, where i indexes each neuron, j indexes neurons upstream, and (ℓ) denotes the layer. The input layer passes the inputs x_i through with unity activation function. Each neuron in the hidden layer $\ell = (1)$ passes the sum of the weighted inputs, including a bias $\beta_i^{(\ell)}$, to the activation function, which in this example is the hyperbolic tangent. Finally, the output layer $\ell = 2$ adds up the weighted inputs, including a bias but has a unity activation function. One can interpret the output of the network Z as the probability that the XOR output should be one rather than zero.

and the biases of the hidden layer and output layer,

$$\vec{\beta}^{(1)} = \begin{bmatrix} \beta_1^{(1)} & \beta_2^{(1)} \end{bmatrix} \quad \text{and} \quad \beta^{(2)} = \psi, \tag{1.6}$$

where ψ denotes a scalar.

Considering the specific case where the activation function of the neurons in this XOR regressor's hidden layer is the hyperbolic tangent, a closed-form of the model is expressed

$$Z = w_{11}^{(2)} \tanh\left(x_1 w_{11}^{(1)} + x_2 w_{21}^{(1)} + \beta_1^{(1)}\right) + w_{21}^{(2)} \tanh\left(x_1 w_{12}^{(1)} + x_2 w_{22}^{(1)} + \beta_2^{(1)}\right) + \beta^{(2)} \tag{1.7}$$

where the output Z is the probability that the parity of the inputs, x_1 and x_2, is odd. For completeness, one solution of such an XOR regressor with hyperbolic tangent activation functions in its hidden layer is:

$$\mathbf{W}^{(1)} = \begin{bmatrix} 1.039 & 1.222 \\ 0.993 & 1.164 \end{bmatrix} \quad \text{and} \quad \mathbf{W}^{(2)} = \begin{bmatrix} -1.567 \\ 1.461 \end{bmatrix} \tag{1.8}$$

$$\vec{\beta}^{(1)} = \begin{bmatrix} -1.914 & -0.179 \end{bmatrix} \quad \text{and} \quad \beta^{(2)} = -1.241 \tag{1.9}$$

where it is clear that there are more parameters (nine) than there are inputs (two) or outputs (one), which is often the case with machine learning models.

Readers will quickly recognize from Eqn. (1.7) that the output of this simple XOR regressor is nothing more than a linear combination of a pair of two-dimensional hyperbolic tangent surfaces spanning the Cartesian input domain from the origin to positive unity, see Fig 1.4. It is important to note that, while continuous functions are plotted in Fig 1.4, valid inputs for the XOR regressor only exist at the extremes of this domain; i.e., (0, 0), (0, 1), (1, 0) and (1, 1), see the table in Fig 1.2. These two non-linear activation functions in the single hidden layer of the regressor sufficiently partition the solution space into even and odd parity

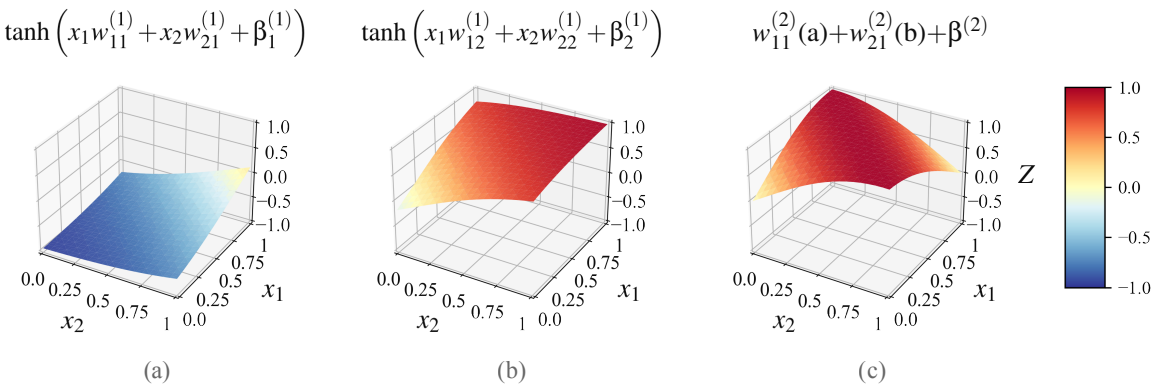

Figure 1.4: Demonstrating the application of a multi-layer perceptron to the XOR problem. The output of the multi-layer perceptron XOR regressor is the linear combination of a pair of two-dimensional hyperbolic tangent surfaces spanning the Cartesian domain from zero to positive unity; however, valid inputs of the XOR regressor only exist at the extremes of this domain; i.e., (0, 0), (0, 1), (1, 0) and (1, 1), see the table in Fig 1.2. (a) Output of the first hidden neuron (Fig. 1.3 top neuron in hidden layer). (b) Output of the second hidden neuron (Fig. 1.3 bottom neuron in hidden layer). (c) Output Z of the multi-layer perceptron XOR regressor, which represents the probability that the parity of the inputs, x_1 and x_2, is odd, see Fig. 1.2.

with nine somewhat interpretable parameters. However, networks employed in production and research solar forecasts typically require more complex architectures than the XOR regressor. The architecture of these networks inherently contains more hidden layers consisting of additional non-linear mappings, defined by model parameters that machine learning training algorithms must learn. Naturally, as the dimensionality of the artificial neural network increases, so does the parameter space, resulting in an anticipated decrease in the interpretability of parameters. Regretfully, solar forecasting research's pursuit of ever-increasing predictive skill associated with the widespread adoption of machine learning techniques has, at times, sacrificed the physical interpretability of the model predictors and the relationship between model predictors and model outputs, which has historically been at the foundation of physics and engineerings sciences. However, this insight reveals an opportunity in solar forecasting research to develop models with more physically interpretable parameters, particularly parameters physically associated with cloud-induced variability in ground-level solar irradiance.

As mentioned before, clouds tend to attenuate ground-level solar irradiance resulting in a reduction in solar generating power output capacity. However, partially cloudy skies may temporarily enhance local GHI above the clear-sky ceiling and, at times, the extraterrestrial irradiance of approximately 1,360 W m^2 [16]. Such enhancements are referred to here as Cloud Enhancement Events (CEE), and they offer a unique opportunity to analyze the timescales on which clouds most strongly induce variability. The second chapter of this work describes how these CEEs can provide solar forecasting and integration insights. This chapter presents the analysis of a full year of ground irradiance data recorded at the University of California, Merced, as well as nearly five months of irradiance data recorded at the University of California, San Diego, and Ewa Beach, Hawaii. The analysis shows that approximately 4% of all data qualify as potential CEEs, which corresponds to nearly 3.5 full days of such events per year if considered sequentially. The surplus irradiance enhancements range from 18 W m^2 day^{-1} to 73 W m^2 day^{-1}. The maximum recorded GHI of 1,400 W m^2 occurred in San Diego on May 25, 2012, which was nearly 43% higher than the modeled clear-sky ceiling. Wavelet decomposition coupled with fluctuation power index analysis shed light on the timescales on which cloud-induced variability and CEEs operate. Results suggest that while cloud fields tend to induce variability most strongly at the 30-minute timescale, they have the potential to cause CEEs that induce variability on timescales of several minutes. This analysis demonstrates that CEEs are an indicator for periods of high variability and, as a result, provide practical information for solar forecasting and integration [17].

1.4 Moving past passive forecasting

We have discussed local clear-sky model inputs and the interpretability of model parameters concerning solar forecasting as an enabling technology. However, with cutting-edge solar forecasting errors approaching the limit of irreducibility , and increased storage leading to the

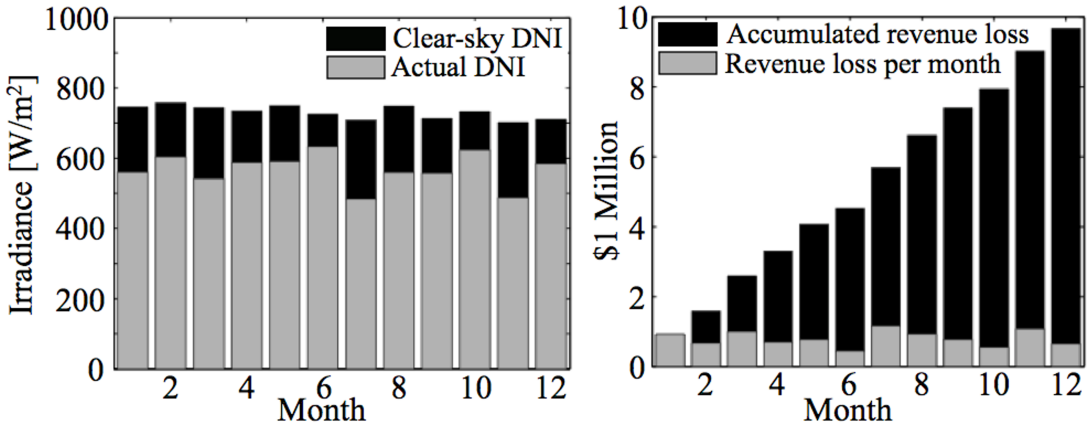

Figure 1.5: Detailing potential energy and revenue losses associated with clouds. Clear-sky and measured DNI for Desert Rock, Nevada, for the year 2013 [18]. For a CSP plant with a nominal capacity of 100 MW and an assumed price of \$0.10 kW^{-1}, the unrealized revenue due to weather effects could amount to approximately \$10 million per year.

decoupling of energy supply and demand , we can expect in the future a situation where grid regulators will know in advance precisely how much renewable solar energy will be available. While such a scenario would be satisfactory from the point of view of a grid manager, it does not address the inherent coupling of ground-level irradiance and the phase transformations of water that cause much of what we experience on Earth as the weather. The unrealized revenue due to the reduction of the solar resource can amount to millions of dollars per year, see Fig. 1.5, which leaves room to implement new technologies that could fundamentally change how solar engineers view weather's effects on solar energy production.

One such approach is the modification of atmospheric structures for the generation of visible 'clearing zones', specifically, the use of a radiation field to induce cloud particle phase transformations. The modification of atmospheric structures has been studied since the late 1940s, when the impact of fogs on visibility for critical maneuvers such as take-off and landing for commercial and military aviation served as the impetus of fog and cloud clearing technology. The most effective clearing technologies have typically been thermally driven; however, this thermal heating results in an increased capacity to hold water vapor and reduced static stability of fog [19].

Fog dissipation systems such as the Turboclair fog dispersal developed in the early 1970s relied on the use of hot gases to evaporate condensed water droplets [20], while other systems have employed the burning of fuel as a mode of thermal input [21]. The difficulty of concentrating heating to a chosen volume and the addition of water vapor through the combustion process, leading to a more significant energy requirement, especially at lower temperatures, have imposed critical limitations on thermal fog-clearing technologies, [19].

Many of the limitations of earlier thermal fog-clearing technologies are solved by developments in laser technologies. Laser energy can be focused on the desired volume and contributes no additional by-products such as those released by combustion, which significantly reduces energy consumption. Mullaney et al. [22] first proposed dispersion of fogs by an intense CO_2 laser in 1968. Considerable experimental and theoretical efforts were placed on clearing fogs and clouds by lasers from the late 1960s to the early 1990s. Theoretical analysis of evaporation of droplets and creating clear zones in cloud medium along with some experimental results were presented by Volkovitsky et al. [23]. Carmana et al. presented simplified mathematical models, and experimental results of high-intensity CO_2 lasers showing the dissipation of both water droplets and ice crystals [24]. These works show the feasibility of creating a clear zone in clouds using a CO_2 laser. The intensity of laser employed by the previous researchers varies, ranging from 0.2-10 W/cm^2 for gradually evaporating droplets and 50-500 kW/cm^2 for rapidly exploding droplets.

More recently, Brewster has studied the evaporation and condensation of water in the air with radiation using the self-similar Spalding model [25], and the effect of thermal radiation from, for example, a CO_2 laser or shortwave solar flux [26]. However, a review of the literature concerning the evaporation of water into quiescent air, the majority of research has focused on refinements of single-mechanism natural convection or else combined heat and mass transfer in buoyancy regions associated with *parallel flow evaporation*, see Fig. 4.1 (a), rather than regions of *contra-flow* evaporation, see Fig. 4.1 (b), where the thermal and concentration processed oppose

each other. Furthermore, experimental conditions associated with elevated relative humidity, particularly relevant to air saturation with water vapor at tropospheric conditions, have not been studied. These conditions are often difficult to maintain and result in reduced driving potentials (low Rayleigh numbers) that, in turn, require careful measurement.

We report on experimental results for natural convection evaporation from a free surface of water into air at low Rayleigh numbers. We performed experiments for air maintained between 285 K and 310 K, for water surface temperatures ranging from 284-308 K, and relative humidity (RH) values ranging from 15-85%. No external heat was added to the liquid during an experiment so that it varies according to evaporation rates during the experiments. A geometry independent length scale is employed, comparing results to those of various other geometries and conditions. The combination of parameters (length scale, temperature, and relative humidity) results in Rayleigh numbers near zero (both positive and negative) that are particularly difficult to measure because several transfer mechanisms are of comparable magnitudes, and therefore, transfer rates are generally unstable. Two distinct flow regimes were observed depending on the existence of a dominant recirculation zone over the evaporative pool. The following simple correlation can accurately describe these distinct flow regimes. When a recirculation zone exists, the correlation is,

$$Sh_{\mathscr{L}} = 0.179\left(Ra_{\mathscr{L}} + 52.5\right)^{1/2},$$

and in the absence of a recirculation zone, the correlation is,

$$Sh_{\mathscr{L}} = 0.206\left(Ra_{\mathscr{L}} + 55.3\right)^{1/2},$$

where $\mathscr{L} = A/P$, A is the area of the free surface, and P is the perimeter of the free surface. A discussion on the effect of flow recirculation zones that lead to the bifurcation of the Sherwood number correlations above is also presented.

1.5 Acknowledgement

Portions of this chapter are taken, in part, from R. H. Inman, H. T. C. Pedro, and C. F. M. Coimbra (2013) “Solar Forecasting Methods for Renewable Energy Integration,” *Progress in Energy and Combustion Science* (39) pp. 535-576. The dissertation author is the first author of this publication

Chapter 2

Impact of Local Broadband Turbidity Estimation on Clear Sky Models for Direct Normal Irradiance

2.1 Introduction

Knowledge of clear-sky irradiance plays a critical role in several solar engineering applications, including the definition of clear-sky indices, the development of smart persistence forecasts, the normalization of information retrieved from satellite data, and the calculation of forecasting skill metrics, [7]. In particular, clear-sky modeling is essential for the accurate determination of Direct Normal Irradiance (DNI) under cloudless skies. DNI is the critical component of the solar irradiance for Concentrated Solar Power (CSP) applications, such as the recently completed Ivanpah Solar Electric Generating System located in the Mojave Desert of California, which at the time of writing is the largest solar thermal project in the world (329 MW). Although CSP technologies currently represent only a small fraction of renewable energy portfolios on a global scale, the International Energy Agency projects annual energy generated from such technologies

to exceed 50 TWh by 2025 [27].

Increased CSP market share will require further policy action to tackle technical and financing challenges that currently hinder deployment [27]. One approach to lower the cost of grid integration is the application of DHI/CSP forecasting, which makes CSP plants more financially attractive to deploy. These forecasts are used to determine optimal operational strategies that maximize profit by minimizing penalty charges resulting from differences between plant output and forecasted output. As a result of CSP plants being driven by DNI, the determination of such optimal operational strategies for CSP plants depends strongly on the accuracy of DNI forecasting. In general, forecast uncertainties are driven by variability in cloud cover. However, under cloudless skies, aerosol particles and water vapor become the most important factors influencing the intensity of ground-level DNI [10, 11].

The term *aerosol* is used to describe either liquid or solid particles that are suspended in the atmosphere with sized ranging from 1 to 10^5 nm in radius [28]. The net effect of aerosols on local microclimates depend on three primary mechanisms: direct radiative forcing as a result of scattering and absorption of visible and infrared radiation in the atmospheric boundary layer, indirect radiative forcing associated with changes in the microphysical and optical properties of cloud fields, and local heating in the cloud formation layer due to highly absorbent aerosols such as black carbon. Although it is clear that DNI attenuation under cloudless skies is driven by aerosol variability, the magnitude of these influences is poorly constrained as a result of the highly spatial-temporal variability of aerosol particles in the atmosphere as well as the fragmentary knowledge of the processes which control the physical, chemical, and optical properties of aerosol distributions [29, 30, 31].

Several methods for the quantification of atmospheric aerosol loading are available in the literature, including both ground-based and remote sensing techniques (see §2.2). While current satellites provide daily multi-wavelength AOD data for nearly any location on the planet, their quality is questionable at times due to missing pixels in AOD retrievals and cloud contamination.

On the other hand, ground-based pyrheliometers are typically located at CSP sites and offer a highly resolved temporal signal of DNI, which is under cloudless skies is related to atmospheric aerosol loading. Therefore, highly temporally resolved ground-based observations of DNI under clear skies allow for a robust sampling of local turbidity, specifically at locations of interest to CSP plant operators.

Several authors have examined the derivation of atmospheric aerosol loading from broadband irradiance measurements. More specifically, Louche et al. [32] assigned a fixed value to the Ångström exponent α (see §2.2) and calculated the Ångström turbidity coefficient β from DNI observations over Ajaccio (France). Gueymard and Vignola [33] developed a semi-empirical model that demonstrated the utility of the diffuse component of broadband irradiance for estimating atmospheric turbidity. Cañada et al. [34] also assigned a fixed value to α to estimate β in Valencia (Spain) and compared the results with those from Ajaccia, Avignon, and Dhahran. Ineichen [35] presented a conversion function between T_{LI}, the atmospheric water vapor, and urban aerosol content that also accounts for the altitude of the application site.

More recently, Polo et al. [36] proposed a method to estimate the daily Linke turbidity factor by using global irradiance measurements at solar noon. Gueymard [37] provided an efficient method to derive Aerosol Optical Depth (AOD) information from broadband DNI measurements and addressed several critical issues, including instrument error, the impact of model performance, propagation of errors due to incorrect precipitable water, elimination of cloudy conditions, and evaluation of α. Gueymard [38] also evaluated the impact of on-site atmospheric water vapor estimation methods on the accuracy of local solar irradiance predictions. Bilbao et al. [39], proposed a method for deriving Ångström's turbidity coefficient and the AOD at 550 nm from broadband DNI observations over Castilla y León (Spain), from July 2010 to December 2012.

In addition to the implicit calculation of aerosol loading from irradiance observations, detailed algorithms exist in the literature that produces aerosol forecasts for aerosol fields using remote sensing techniques and transport models, see, for example, Masmoudi et al. [40]. However,

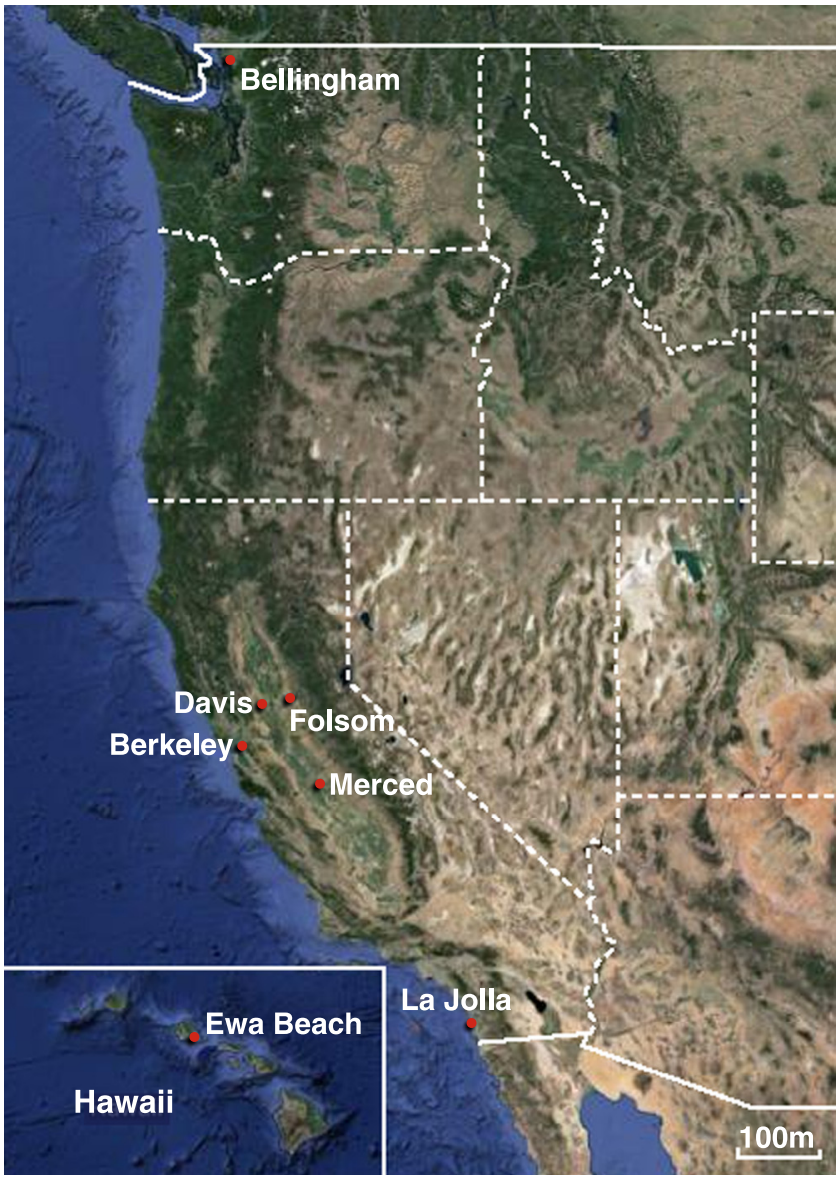

Figure 2.1: Map of the relative location of the stations used in [2].

this contribution demonstrates the utility of ground-based estimations of average daily turbidity for the day-ahead forecasting of broadband clear-sky DNI at a specific site. Because of CSP's dependence on broadband DNI, this irradiance component tends to be measured on-site, resulting in readily available broadband turbidity information at such locations. An endogenous clear-sky detection algorithm for DNI is developed, which is based on the work of Reno et al. [6], and applied to nearly ten site-years of data from seven stations spread across the states of California, Washington, and Hawaii (see Fig. 2.1). These data represent several widely varying microclimates that are used to speak to the robustness of the algorithm. Observations of clear-sky DNI are subsequently used to calculate the daily average air mass-independent Linke turbidity factor T_{LI}. A day ahead forecast of clear-sky DNI is then issued under the persistence assumption of average daily turbidity. The observed DNI under clear skies can then be used to calculate the forecast's error. To demonstrate the value of using daily values of turbidity, the method is compared against the monthly climatologies from Remund et al. [3].

Section 2.2 describes the quantification of aerosol loading, Section 2.3 details the experimental data, Section 2.4 covers the endogenous clear-sky detection algorithm, Section 2.5 describes the methodology, Section 2.6 describes the metrics used for comparison, and Sections 2.7 and 2.8 contain the results and conclusions respectively.

2.2 Aerosol loading

While many formulations exist in the literature for the quantification of aerosol loading, this is typically achieved through the use of Ångström's Law,

$$\tau(\lambda) = \beta\lambda^{-\alpha} \tag{2.1}$$

where $\tau(\lambda)$ is the monochromatic aerosol attenuation coefficient, or Aerosol Optical Depth (AOD); β is the Ångström turbidity coefficient, which represents the AOD at a wavelength of 1 μm; λ

denotes the wavelength (μm); and α is the Ångström exponent, which is a function the size distribution of the aerosols. The Ångström turbidity coefficient does not incorporate the optical depth of water vapor or other participating gasses and therefore provides an uncontaminated measure of atmospheric aerosol loading. However, α and β are known to exhibit daily fluctuations driven by atmospheric processes such as photo-chemical activity, local emissions, mesoscale circulation, wind ventilation, and temperature changes resulting from phase changes in the atmosphere [39]. As a result, capturing the intra-daily variability in AOD requires highly resolved temporal data of AOD, typically not available without a ground-based sun-photometer nearby (e.g., NASA's Aeronet network).

Other sources of spectrally resolved AOD and water vapor data exist, specifically, those that involve remote sensing (e.g., MODIS onboard NASA's AQUA/TERRA). However, it is known that such data may contain significant errors, especially over regions of low turbidity and high albedo, such as the southwest US [37, 41]. Furthermore, due to the nature of the Polar Low-Earth Orbit (PLEO) of the TERRA and AQUA satellites, which descend/ascend across the equator at about 10:30 a.m. and 1:30 p.m. local time respectfully, a strict sampling is imposed. Often clouds are present during a satellite's pass over a location (see Appendix A), which can result in cloud contamination or missing pixels in AOD retrievals, particularly at high spatial and temporal resolutions. It should be noted that these issues are typically addressed by combining aerosol fields retrieved from both TERRA and AQUA MODIS imagery to produce a more complete data set of sufficiently relaxed spatial resolution (e.g., $1^\circ \times 1^\circ$ used by MODIS). Until the launch of new generation instruments on geostationary satellites that provide a constant full-field view, such as GOES-R, the sampling rate of remote sensing techniques may be unsuitable for the accurate determination of highly resolved intra/inter-daily turbidity information. As a result, it may be desirable to use other sources of data with higher sampling rates, such as broadband DNI observations at ground level, which are typically co-located with CSP plants.

Ground-based observations of broadband DNI under clear-skies can characterize the

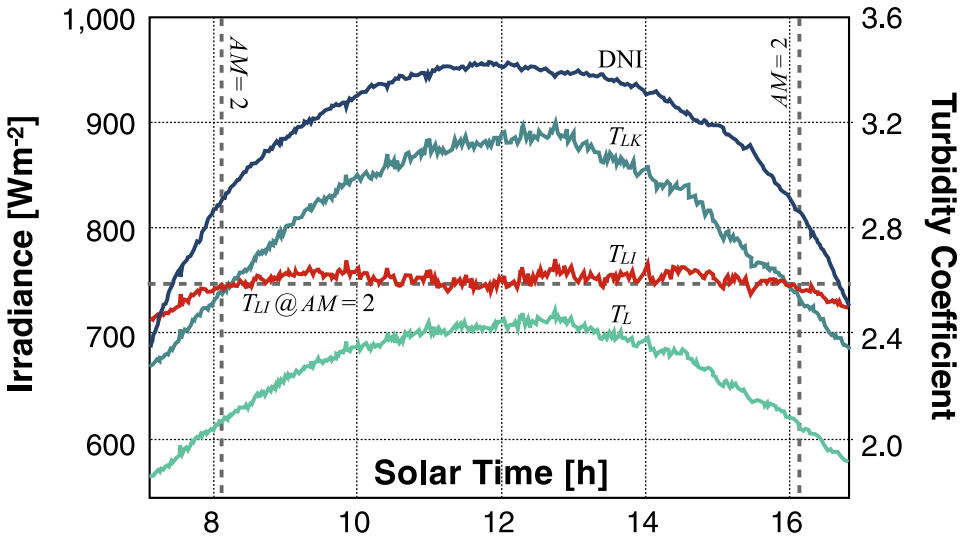

Figure 2.2: Evolution of broadband Direct Normal Irradiance (DNI) at 30 s resolution measured with a Normal Incidence Pyrheliometer (NIP) and SMT-3 solar tracker (available from the Eppley Laboratory, Inc) as well as T_L, T_{LK}, and T_{LI} during the 3rd of April 2011 at the University of California, Merced.

behavior of an aerosol and moisture-laden atmosphere through broadband turbidity indices, which quantify the atmosphere's overall level of opacity to broadband solar radiation. While this method offers a less accurate broadband quantification of aerosol and water loading, it is much simpler to implement, and its errors are acceptable for day-ahead clear-sky DNI forecasts. The most commonly used broadband turbidity coefficients are the Unsworth–Monteith turbidity coefficient τ_a, and the Linke turbidity factor T_L. Unsworth and Monteith [42] defined τ_α using the following expression

$$D_c(\tau_a) = D_0 \exp(-\tau_a m), \tag{2.2}$$

which relates the measured clear-sky direct normal irradiance $D_c(\tau_a)$ to the direct irradiance calculated for a dust-free atmosphere D_0 where the air mass is m. Similarly, Linke [43, 44] defined his turbidity factor as the number of clean, dry atmospheres required to reproduce the

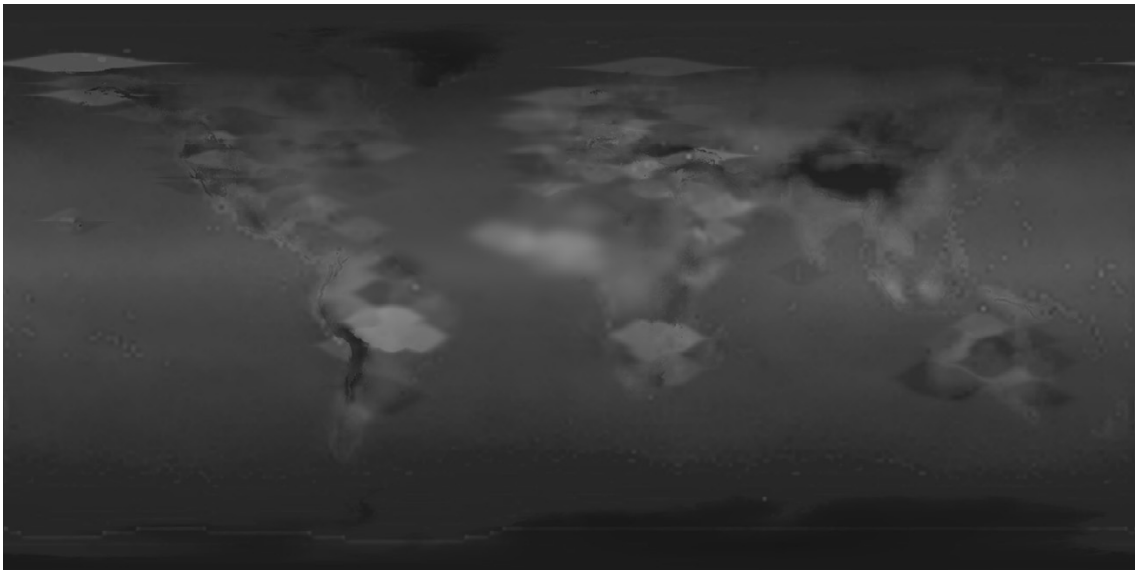

Figure 2.3: Example of one of the monthly maps of Linke turbidity for the world developed by Remund et al. [3]. The maps can be downloaded from either the Solar Radiation Data website [12].

attenuation of extra-terrestrial radiation caused by the real atmosphere as

$$D_c(T_L) = I_0 \exp(-\delta_{cda} T_L m), \tag{2.3}$$

where $D_c(T_L)$ is the observed DNI under cloudless skies, I_0 is the sun-earth distance corrected extraterrestrial irradiance, δ_{cda} is the optical thickness of a clear and dry atmosphere, and m is the air mass. It is known that τ_a and T_L are marginally dependent on air mass m [45]. More recently, however, Ineichen and Perez [46] developed an airmass independent formulation of Linke turbidity factor T_{LI}, which provides greater stability throughout the day, (see Fig. 2.2). Unlike the rigid sampling rate of remote sensing techniques, the increased stability of T_{LI} allows for a flexible sampling of atmospheric turbidity at any time that clouds do not obscure the circumsolar region.

The Linke turbidity factor has also become a key input for a number of Clear Sky Models (CSMs) [47, 48, 49, 50, 13, 4]. Based on the widespread use of the Linke turbidity factor for

clear-sky modeling, several regional and worldwide maps of monthly/seasonal Linke turbidity have become available in the literature [50, 3], an example of which is shown in Fig. 2.3. While the monthly/seasonal resolution of these maps are convenient for locations where no ground truth exists and are typically sufficient for the clear-sky modeling of GHI [6], they are not suitable for the accurate modeling of DNI, which demonstrates increased sensitivity to variability in aerosol loading.

In general, the scattering caused by aerosols under cloudless skies increases the local Diffuse Horizontal Irradiance (DHI) and commensurately decreases the DNI. This exchange between DHI and DNI effectively buffers the impact of aerosols on clear-sky Global Horizontal Irradiance (GHI), which defines in the closure equation,

$$G = D\cos\theta_z + d \tag{2.4}$$

where the global horizontal irradiance G is defined as the geometric sum of the direct normal irradiance D and diffuse horizontal irradiance d, and θ_z is the solar zenith angle. This buffering is the reason aerosol loading is known to attenuate DNI in the range of 30–100% as opposed to GHI, where the attenuation is significantly lower at approximately 10% [51, 52, 53]. Furthermore, Gueymard [54] showed that DNI exhibits an Aerosol Sensitivity Index (ASI), which relates the magnitude of relative variations in irradiance to absolute variations in aerosol optical depth, that is 2–4 times greater than that for GHI. The difference in intensity reduction between GHI and DNI is one key reason why GHI forecasting techniques have been reviewed extensively in the literature [55, 10, 6], should not be directly applied to DNI forecasting. Therefore, it is desirable to calculate spatially and temporally local Linke turbidity information through ground-based observations of broadband DNI under clear skies.

The Linke turbidity factor T_L is, among others, a turbidity index, which is calculated by inverting a model that estimates broadband DNI under cloudless skies and thus refers to the

spectrally integrated attenuation [32, 56]. As a result, T_L incorporates the optical depth of water vapor and is not a pure turbidity coefficient [45]. Nevertheless, because T_L is empirically derived from DNI measured at many meteorological stations, its use remains widespread.

The turbidity factor defined by Linke [43, 44] can be expressed explicitly by solving Eq. (2.3) for T_L,

$$T_L = \frac{1}{\delta_{cda}\, m} \ln\left(\frac{I_0}{D_c}\right), \tag{2.5}$$

where it is clear that T_L is dependent upon the theoretical value of δ_{cda} employed. Later, Kasten [57] made use of a series of spectral data tables published by Feussner and Dubois [58] to develop the widely used pyrheliometric formula:

$$\delta_{cda} = (9.4 + 0.9m)^{-1}, \tag{2.6}$$

which gave rise to the definition of the *Linke turbidity factor as corrected by Kasten* T_{LK}:

$$T_{LK} = \frac{9.4 + 0.9m}{m} \ln\left(\frac{I_0}{D_c}\right) \tag{2.7}$$

More recently, Ineichen and Perez [46] showed that both T_L and T_{LK} exhibit diurnal variations and are a function of air mass even when the aerosol optical depth remains relatively constant. As a result, Ineichen and Perez [46] proposed an air mass-independent Linke turbidity factor T_{LI}, where similar to the work of Rigollier et al. [49], T_{LK} at $m = 2$ was used as a reference. The Linke turbidity factor, as corrected by Ineichen T_{LI}, is obtained by inverting the following model for DNI under clear skies:

$$D_c = b I_0 \exp\left[-0.09\, m\, (T_{LK}^{m=2} - 1)\right] \tag{2.8}$$

where

$$b = 0.644 + \frac{0.163}{\exp(-h/8000)} \tag{2.9}$$

has been adopted from Kasten [59] and h is the elevation in meters. Seasonal trends of T_{LK} were evaluated with (2.7) at $m = 2$ under cloudless skies after which the expression in (2.8) was inverted to give T_{LI} as:

$$T_{LI} = \frac{11.1}{m} \ln\left(\frac{bI_0}{D_c}\right) + 1 \tag{2.10}$$

which has the advantages of (1) being independent of the air mass and (2) matching T_{LK} at air mass two.

Fig. 2.2 shows the evolution of broadband DNI at 30 s resolution measured with a Normal Incidence Pyrheliometer (NIP) and SMT-3 solar tracker (both available from the Eppley Laboratory, Inc) as well as T_L; T_{LK}, and T_{LI} during the 3rd of April 2011 at the University of California, Merced. It is important to pause here and discuss the significantly different magnitudes for the three determinations of the Linke turbidity factor, which were also shown by Ineichen and Perez [46]. Contrarily to AOD, the Linke turbidity factor does not represent a pure optical characteristic of aerosol extinction but is also affected by the parasitic effects of air mass and water vapor. In addition, Linke turbidity cannot be measured directly; it must be derived from DNI measurements by inverting an appropriate solar radiation model. As a result, any published value of Linke turbidity is more or less dependent on the water vapor columnar amount and model used. However, a formulation of turbidity that does not vary with relatively uniform aerosol loading is desirable as it can be used to obtain a representative turbidity value under cloudless skies at any air mass. It is clear from Fig. 2.2 that $T_{LI} = T_{LK}$ @ $m = 2$ and the stability of T_{LI} throughout the day is much better than T_L and T_LK. It is on this basis that T_LI is employed in this work.

2.3 Experimental data

Data is used from seven stations spread across the states of California, Washington and Hawaii spanning the years 2011–2014. The locations of these stations possess varying latitudes, and microclimates; including:

- Bellingham, WA; latitude, 48.8°N; longitude, 122.5°W; altitude, 6 m; temporal resolution, 60 s; instrumentation, Irradiance Inc. RSR2.
- Berkeley, CA; latitude 37.9°N; longitude 122.3°W; altitude, 109 m; temporal resolution, 60 s; Yankee Environmental Systems, Inc. MFR-7.
- Davis, CA; latitude, 38.5°N; longitude, 121.7°W; altitude, 19 m; temporal resolution, 60 s; Yankee Environmental Systems, Inc. MFR-7.
- Ewa Beach, HI; latitude, 21.3°N; longitude, 158.0°W; altitude, 10 m; temporal resolution, 60 s; instrumentation, Irradiance Inc. RSR2.
- Folsom, CA; latitude, 38.6 °N; longitude, 121.4°W; altitude, 97 m; temporal resolution, 60 s; instrumentation, Irradiance Inc. RSR2.
- La Jolla, CA; latitude, 32.9°N; longitude, 117.2°W; altitude, 106 m; temporal resolution, 30 s; Eppley Laboratory, Inc. NIP on SMT tracker and PSP.
- Merced, CA; latitude, 37.3°N; longitude, 120.4°W; altitude, 65 m; temporal resolution, 30 s; Eppley Laboratory, Inc. NIP on SMT tracker and PSP.

Each of the databases contains anywhere from 9 to 26 months of measurements of all three irradiance components at either a 30 or 60 s sampling rate. The duration of the data acquisition as well as the instrumentation used to take observations are listed in Fig. 2.4.

The LI-COR LI-200SZ utilized in the rotating shadow-band radiometer head unit of the RSR2 (Irradiance Inc.) is a relatively simple device that requires software to correct for

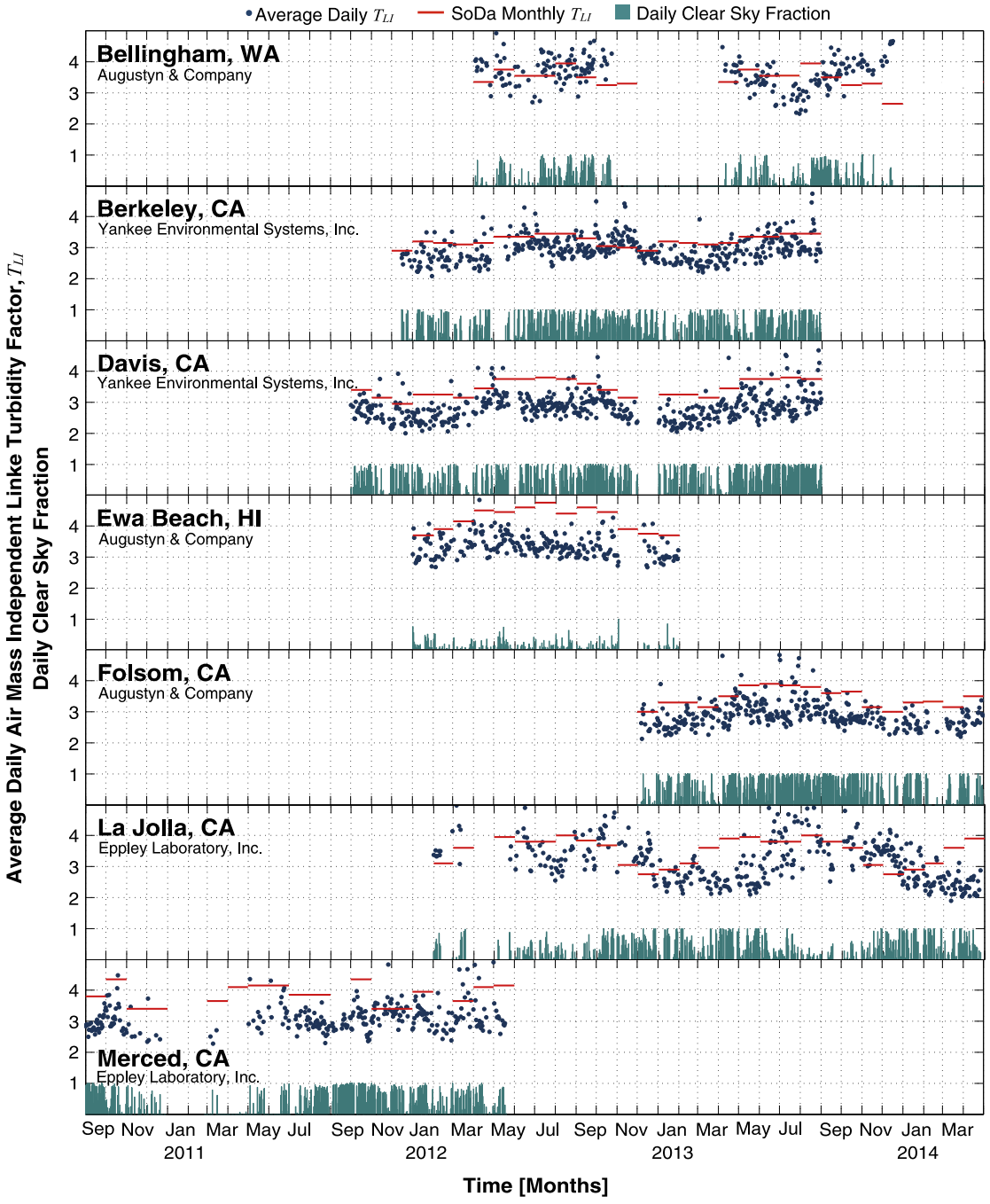

Figure 2.4: Plot of the observed average daily T_{LI} for days when clear skies were detected, the tabulated monthly average from Remund and Page [4], and the fraction of measurements classified as clear for the entire data set used in this work.

cosine errors. This sensor has a typical cosine error of less than 5% up to an 80° angle of incidence. For sun plus sky at a sun elevation of 30° (60° angle of incidence), the error is ≈2%. Similarly, the MFR-7 has a novel input optic with excellent cosine response and long term stability. The individual MFR-7 cosine response, supplied with each instrument, is used by YESDAS system software to correct, in real-time, for deviations from the ideal cosine response. Similar to the LI-200SZ, the error is typically ≤2% at a 60° angle of incidence. The Eppley NIP pyrheliometer (mounted on SMT tracker) and PSP pyranometer are secondary standard instruments with uncertainties of less than 1.5% and 3.5%, respectively. At all of the stations, GHI was observed independently from DNI, which allows for enhanced quality control using the summation method to obtain global irradiance [60]. Observations where the ratio of calculated GHI, using Eq. (2.4), and observed GHI differs from unity by more than 20% were excluded as they typically correspond to an error in at least one of the irradiance components.

2.4 Clear sky detection

Clear-sky detection through cloud filtering is vital to the methodology's success, such that only DNI observations that represent clear-sky conditions within the field of view of the radiometer are used. Typically, two approaches have been employed: (1) direct filtering of cloud conditions in the DNI time-series or (2) back-end filtering where all DNI data is used and observations that provide physically un-reasonable clear-sky conditions are eliminated.

Long and Ackerman [61] have implemented the first approach; however, the Fortran files and executables of the algorithm have been found to be slow and cumbersome to use [37]. The second approach was adopted by AERONET for cloud-screening from sunphotometric observations by Smirnov et al. [62] and more recently Gueymard [37] employed a similar technique based on five independent requirements.

In this work, rather than directly implementing the Long filter or adopting a back-end

filtering, clear-sky detection is performed using an endogenous statistical model originally developed by Reno et al. [6] for GHI observations. This method uses five criteria to compare a period containing N observations of GHI to a corresponding CSM for the same period. The period is deemed "clear" if threshold values (whose values vary with N) for each criterion are met.

In this work, the criteria include the mean value of irradiance I (global and direct) during the time period,

$$\bar{G} = \frac{1}{N}\sum_{t=1}^{N} I(t), \tag{2.11}$$

the maximum irradiance value M in the time series

$$M = \max[I(t)] \quad \forall \quad t \in \{1,2,\ldots,N\}, \tag{2.12}$$

the length L of the line connecting the points in the time series that, unlike L defined in [6], does not account for the length of the time-step,

$$L = \sum_{t=1}^{N} \sqrt{[I(t+\Delta t) - I(t)]^2}, \tag{2.13}$$

the variance of changes in the time series; specifically, the normalized standard deviation σ of the slope between sequential points,

$$\sigma = \frac{\sqrt{\frac{1}{N-1}\sum_{t=1}^{N-1}(s(t)-\bar{s})^2}}{\frac{1}{N}\sum_{t=1}^{N} I(t)} \tag{2.14}$$

where

$$s(t) = I(t+\Delta t) - I(t), \quad \forall \quad t \in \{1,2,\ldots,N\} \tag{2.15}$$

$$\bar{s} = \frac{1}{N-1}\sum_{t=1}^{N-1} s(t) \tag{2.16}$$

and, S the maximum deviation from the clear-sky slope s_c,

$$S = \max\{|s(t) - s_c(t)|\} \quad \forall \quad t \in \{1, 2, \ldots, N\} \tag{2.17}$$

where

$$s_c(t) = I_c(t + \Delta t) - I_c(t). \tag{2.18}$$

Similar to Reno et al. [6], in this work, a 10-min sliding window is employed to determine if an observation is identified as "clear". The five clear-sky criteria ($\bar{G}$, M, L, σ, and S) are evaluated for both the CSM and observational time series for each 10-min window. The window then progresses forward in time by one time step each iteration. Accordingly, for a 1 min sampling rate, each irradiance measurement would be evaluated ten times as the window steps forward in time. A measurement is identified as clear as long as it is within at least one coherent window declared as clear during the evaluations. In other words, the sliding window checks every combination of ten contiguous observations, and if at least one window meets all five criteria, all ten measurements in that window must be clear. In this way, each observation may be classified as clear or cloudy [6]. Fig. 2.5 shows the observed GHI, the observed DNI, the CSMs calculated from SoDa turbidity values, and the values of the metrics centered on each of the ten minute sliding windows. It is clear that the variability caused by clouds violates at least one of the criteria in all cases and that the clear periods meet all five criteria.

Both DNI and GHI data were available from all stations, and, as a result, in this work, both are used to determine clear-sky criteria. Each measurement is classified as clear only if threshold values for all five of the clear-sky criteria are met for both the DNI and GHI time series in at least one coherent window. This approach results in a more robust clear-sky determination protocol as it is known that the global irradiance is less sensitive to thin clouds that act as diffusers. The threshold values from Reno et al. [6], as well as the values used in this work, are listed in Table 2.1. In addition, the fraction of the daytime irradiance measurements classified as clear,

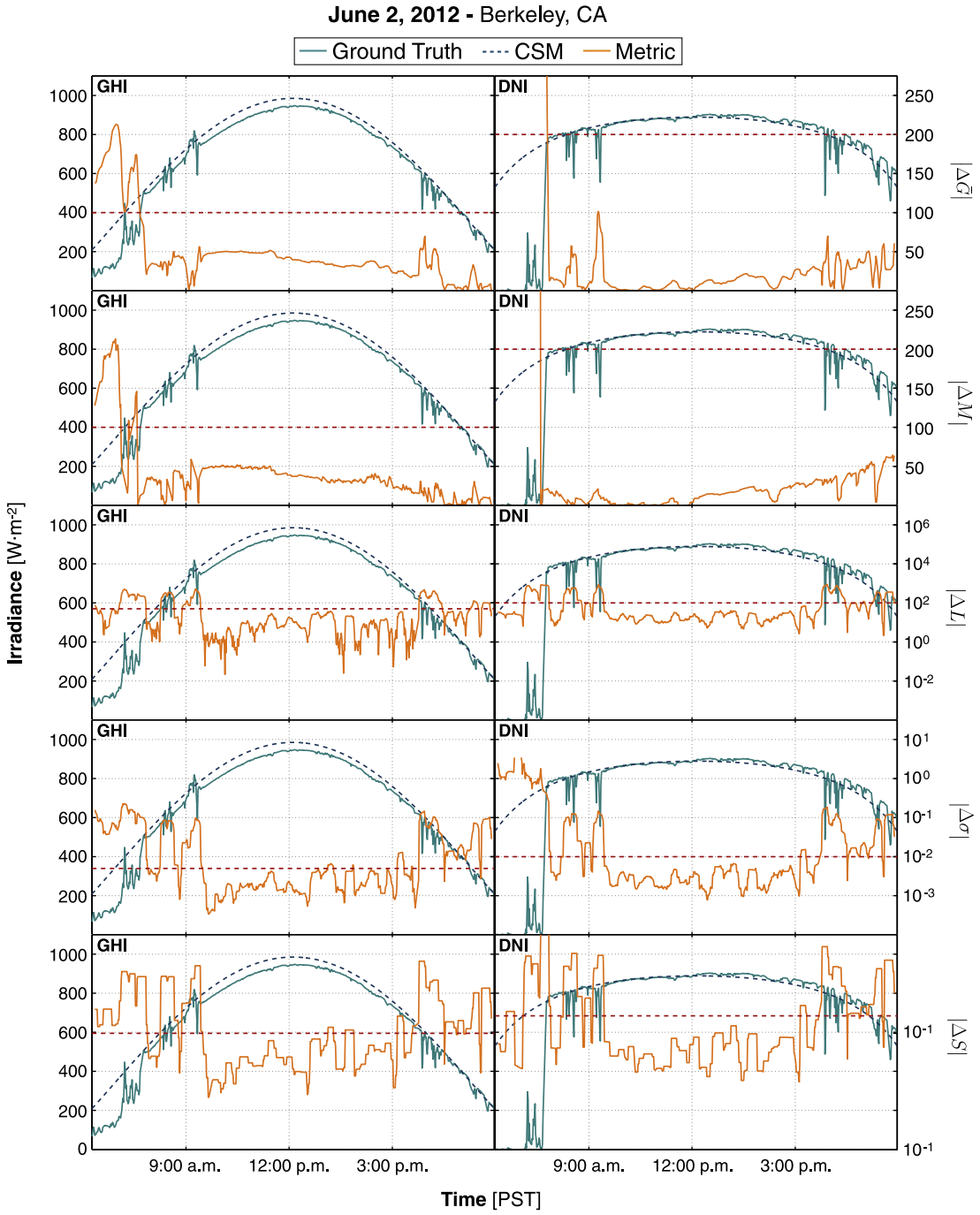

Figure 2.5: Observed GHI and DNI, the CSMs calculated from persistence turbidity values and the value of the metric centered at the ten-minute sliding window. It is clear that the variability caused by clouds violates at least one of the criteria in all cases and that the clear periods meet all five criteria.

Table 2.1: Clear sky criteria threshold values from Reno et al. [6] (GHI_R) as well as the values used in this work (GHI_I and DNI_I). The thresholds for DNI were slightly relaxed as a result of increased variability in the observational DNI time series.

	GHI_R	GHI_I	DNI_I
$\bar{G}$	± 75 Wm^{-2}	± 100 Wm^{-2}	± 200 Wm^{-2}
M	± 75 Wm^{-2}	± 100 Wm^{-2}	± 200 Wm^{-2}
L	-5 to 10	± 50	± 100
σ	< 0.005	< 0.01	< 0.015
S	< 8 Wm^{-2}	< 10 Wm^{-2}	< 15 Wm^{-2}

and the calculated average daily T_{LI} are given for each day in Fig. 2.4. It should be noted that clear-sky DNI observations are required for the calculation of T LI and, consequently, no turbidity information is available for days that lack clear-sky observations.

2.5 Method

It is well known that under cloudless skies, the presence of aerosol particles and water vapor in the atmosphere are among the most important factors affecting the attenuation of downwelling irradiance, particularly in the case of DNI which is highly sensitive to the optical properties of the atmospheric column. It is the highly variable nature of aerosol particles and water vapor in the atmosphere that serves as motivation for including spatially and temporally local broadband turbidity information for the reduction of DNI forecasting errors. In order to achieve this a number of techniques are employed.

First, it should be noted that observations corresponding to solar zenith angle greater than 75° were removed from the data set so that only daylight hours with reasonable air mass are included. For each month in the data set, the location's turbidity information is looked up from the monthly SoDa world maps of Linke turbidity [4]. This monthly turbidity approximation is then used as an input to calculate the DNI CSM for the entire month using Eq. (2.8) and assuming

that $T_{LI} = T_{LK}^{m=2}$ as well as the GHI CSM from Ineichen and Perez [46], see Fig. 2.6(a). The airmass independent Linke turbidity factor T_{LI} is calculated from DNI measurements, which is equal to Kasten's Linke turbidity factor T_{LK} at $m = 2$, see Fig. 2.6(b). After this initial CSM and T_{LI} are calculated, its general shape is used to perform a binary clear-sky detection as described in Section 2.4, see Fig. 2.6(c). For each of the partially clear days, an average T_{LI} is calculated, which is then used as an input to Eq. (2.8) to re-calculate the CSM, see Fig. 2.6(d). Each of the average daily T_{LI} is shown in Fig. 2.4 for days where clear-sky observations exist.

A day-ahead DNI clear-sky forecast is then issued under the assumption of the persistence of the average daily T_{LI}. For days when no clear-sky observations exist, the most recent historical clear-sky observation is used to calculate the forecast allowing for the investigation of errors associated with lagged turbidity data. Because forecasting models are often tuned for specific microclimates, the distribution of parameters such as T_{LI} provides valuable insight into which methods should be employed for such climates. For example, climates with a broader distribution of turbidity values would perform worse under the persistence assumption. As a result, histograms of the clear-sky T_{LI} are also provided. Finally, the performance of the day ahead forecast is evaluated as a function of the zenith angle using two metrics described in the next section in conjunction with the clear-sky observations of DNI at the seven stations.

2.6 Metrics

To evaluate the performance of the CSMs, both the Root Mean Square Error (*RMSE*) and Mean Bias Error (*MBE*) as a function of the solar zenith angle will be calculated. However, in many contexts, the relative error is more commonly desired than absolute error, especially for users in the utility industry [7]. Following Hoff et al. [63], simplified reporting approaches for relative (percent) versions of *RMSE* and *MBE* are used in this work. The *rRMSE* is normalized

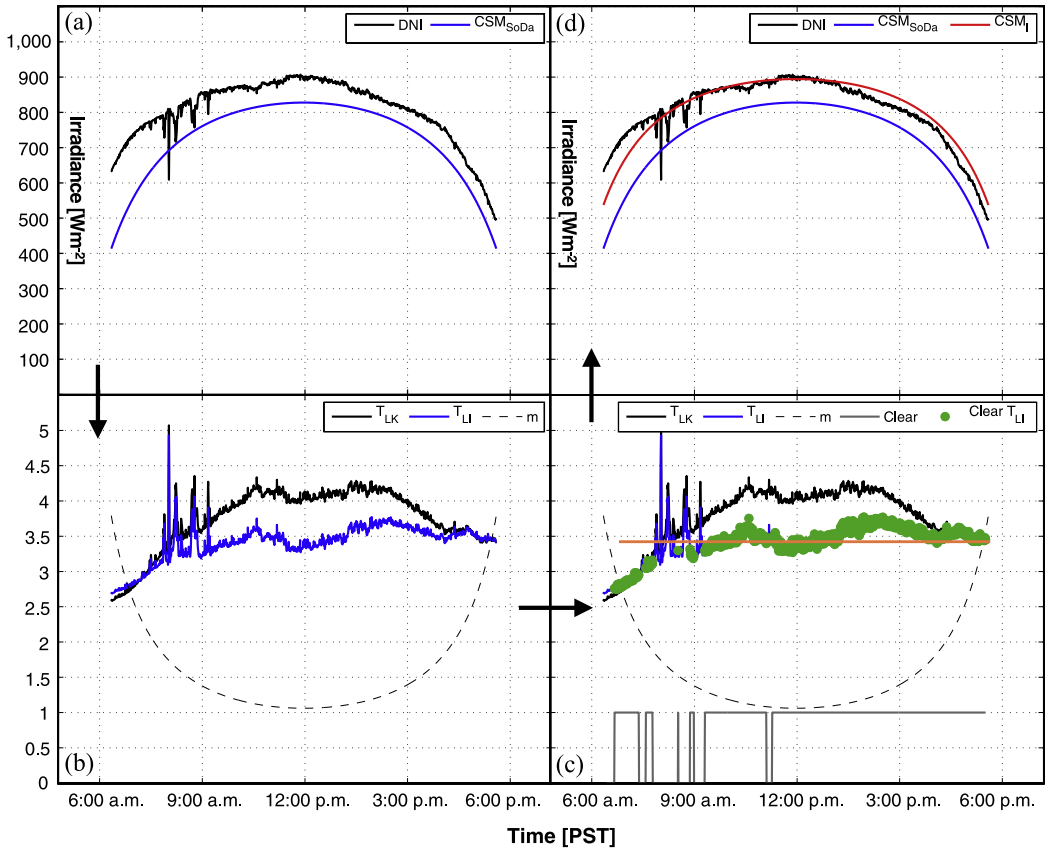

Figure 2.6: Illustration of methodology: (a) for each month in the data set, turbidity information for the location is looked up from the monthly SoDa world maps of Linke turbidity [4]. This monthly turbidity approximation is then used as an input to calculate the DNI CSM for the entire month using Eq. (2.8), assuming that $T_{LI} = T_{LK}^{m=2}$. (b) The airmass independent Linke turbidity factor T_{LI} is calculated from DNI measurements, which is equal to Kasten's Linke turbidity factor T_LK at $m = 2$. (c) After the initial CSM is calculated, its general shape is used to perform binary clear-sky detection as described in Section 2.4. (d) For each of the partially clear days an average T_{LI} is calculated which is then used to as an input to Eq. (2.8) to estimate the CSM.

with the average value of the observed clear-sky irradiance at that zenith angle

$$rRMSE = \frac{\sqrt{\frac{1}{N}\sum_{t=1}^{N}(\hat{I}(t) - I(t))^2}}{\frac{1}{N}\sum_{t=1}^{N} I(t)} \tag{2.19}$$

Similarly, the *rMBE*, which has the advantage of being independent of the number of observations and being easy to understand, is also obtained through a normalization of the *MBE* by the average value of the irradiance

$$\begin{aligned} rMBE &= \frac{\frac{1}{N}\sum_{t=1}^{N}(\hat{I}(t) - I(t))}{\frac{1}{N}\sum_{t=1}^{N} I(t} \\ &= \left(\frac{1}{\sum_{t=1}^{N} I(t)}\right)\sum_{t=1}^{N}(\hat{I}(t) - I(t)). \end{aligned} \tag{2.20}$$

It is important to pause here and note that as a result of the metrics being calculated as a function of zenith angle, the average value in (2.19) and (2.20) correspond to the average value at a given zenith angle, rather than the average value over the entire time series. Furthermore, as a point of clarification, observations were separated in bins of equal zenith angle rounded to the nearest degree, before calculating the metrics at each zenith angle. While this comes with an additional computational expense, the impact is insignificant compared to the implementation of the method itself.

2.7 Results

As mentioned in Section 2.5, the calculated average daily T_{LI} for days with clear-sky observations, the monthly SoDa T_{LI}, and the fraction of each day classified as clear using the method described in Section 2.4 are shown in Fig. 2.4. Fig. 2.4 illustrates that, except Bellingham and La Jolla, the calculated average daily T_{LI} for all stations was typically 15–30% less than the monthly SoDa values for T_{LI} indicating that the SoDa database for T_{LI} tends to underestimate

Table 2.2: Table listing days included in the study, observations that met the closure equation quality control, percentage of the observations classified as clear, average airmass independent Linke turbidity factor T_{LI}, and standard deviation of the distribution of T_{LI} for each site.

	Days	Total Obs.	% Clear	$\bar{T_{LI}}$	Std.
Oahu	397	215,746	9.78	3.34	0.37
Bellingham	760	366,050	19.51	3.43	1.02
La Jolla	820	629,576	28.02	3.09	0.82
Berkeley	701	353,210	44.19	2.90	0.62
Davis	670	366,391	44.60	2.81	0.54
Merced	608	596,327	46.15	2.94	0.88
Folsom	516	262,896	52.59	2.79	0.72

DNI for the particular CSM employed in this work. It is also clear from Fig. 2.4 that Folsom, Davis, Merced, and Berkeley (all located within $\sim$160 km from each other) were characterized by a significant fraction of clear days. The remaining sites exhibited significantly fewer clear-sky observations with tropical Ewa Beach, HI, showing the fewest followed by Bellingham, WA, which is consistently overcast, and coastal La Jolla, CA, with its volatile marine layer. Table 2.2 lists the total number of days that included in the study, the total observations that met the closure equation quality control, percentage of the observations classified as clear, the average airmass independent Linke turbidity factor, and the standard deviation of the T_{LI} distribution for each site.

The relative (or percent) versions of the *RMSE* and *MBE* described in Section 2.6 were also calculated as a function of the solar zenith angle. Again, we compare the CSM obtained from the monthly SoDa maps of T_{LI} with the experimental method and persistence forecast described in Section 2.5. The statistics are based on days where at least 10% of the observations are clear to ensure accurate sampling of the attenuation caused by the atmospheric column. Overall, this set of validation metrics is presented in Fig. 2.7. The *rRMSE* for the method applied to the same day is typically less than 5% and can be as low as 0.5% for zenith angles less than 30°; except Bellingham, WA, whose *rRMSE* exceeds 5% for zenith angles greater than 60°. The $rRMSE_{Pers}$ of the forecasted persistence T_{LI} CSM had a similar shape to the *rRMSE* with an additional

1–3% error while the monthly SoDa T_{LI} produced an $rRMSE_{SoDa}$ of a comparable shape with an additional 3–5% error over the $rRMSE_{Pers}$.

Fig. 2.7 also shows that the *rMBE* of the monthly SoDa T_{LI} is consistently negative for all zenith angles, which is also in agreement with the results presented in Fig. 2.4 and again suggests that the SoDa input data in conjunction with the CSM employed in this work consistently underestimates DNI through an overestimation of T_{LI}. It should be noted that the $rMBE_{Pers}$ was similar to the *rMBE* of the improved CSM for all of the sites, including Bellingham, WA. The relatively small ($\sim$1–2%) and *positive rMBE* of the improved and forecasted CSMs also indicate a slight overestimation of DNI rather than the notable underestimation provided by the monthly SoDa T_{LI} data, which is typically desirable of CSMs.

Fig. 2.8 shows the histograms of the average daily T_{LI} for each of the seven stations. It is clear that, except for Bellingham and La Jolla, a general trend is apparent in the distribution of T_{LI}. Most of the sites exhibit an almost normal distribution centered near $T_{LI} = 3$. Bellingham, however, has a distribution that is shifted to the right and centered near 3.75. This value is characteristic of its marine oceanic climate, strongly influenced by the Cascade Range to the east that retains marine temperature influences and the Olympic Mountains to the southwest that provide a strong-rain shadow effect. On the other hand, La Jolla's distribution is significantly broader, with no apparent peak. This distribution is characteristic of the wind dominated weather pattern in La Jolla. Typically, eastwardly winds are cooled as they pass over the Pacific Ocean and advect a thick marine layer of fog that dissipates near mid-day. Occasionally, however, the westward Santa Ana winds will increase aerosol loading as they pass over the desserts to the east and push temperatures to nearly 40°C, well above the average annual high of approximately 20°C. These marine layer climatologies may explain some of the decreased performance at Bellingham apparent in Fig. 2.7.

Finally, a general trend is apparent in Fig. 2.7, which should be taken into account. For all of the stations included in this study, errors increase in magnitude with the zenith angle,

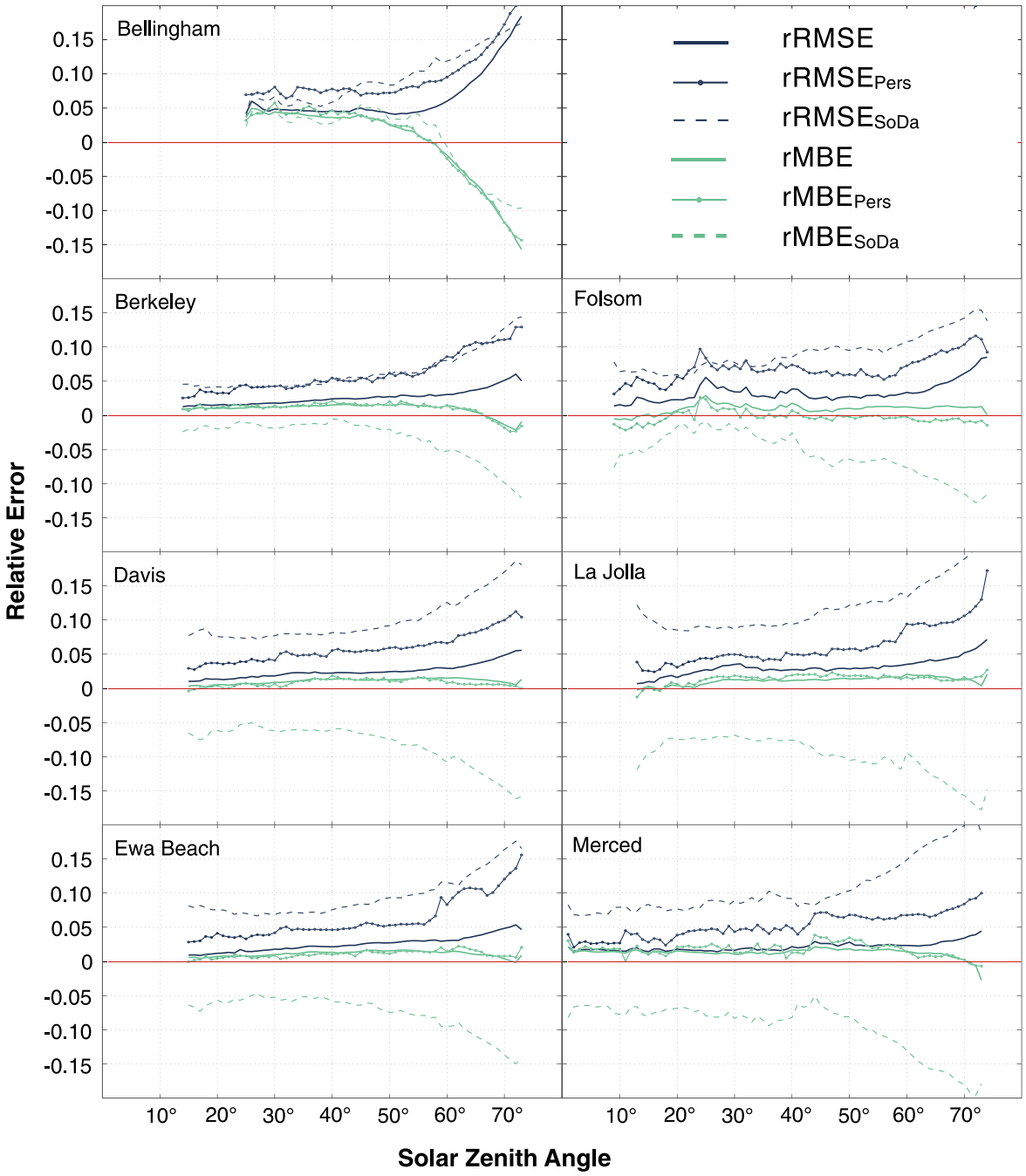

Figure 2.7: Comparison of clear-sky *rRMSE* and *rMBE* as a function of zenith angle for the monthly SoDa turbidity maps, the experimental method, and persistence forecast described in Section 2.5. The extensive decrease of both *rRMSE* and *rMBE* of the improved DNI CSM over a wide range of zenith angles suggest that increased accuracy is achievable with minimal resources.

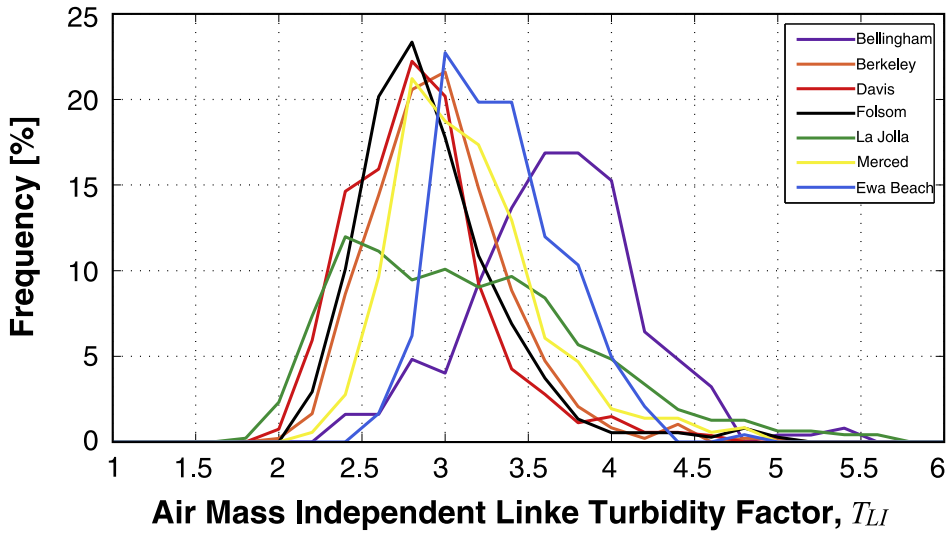

Figure 2.8: Histograms of the average daily T_{LI} for each of the seven stations. Except for Bellingham and La Jolla, all stations exhibit a nearly normal distribution centered near three.

suggesting that the DNI CSM and consequently the definition of T_{LI} still has some dependence on airmass.

2.8 Conclusions

This study focus on the sensitivity of day-ahead DNI forecasts under clear skies to local fluctuations in turbidity. An endogenous clear-sky detection algorithm for DNI was developed based on the recent work of Reno et al. [6], which was then used to determine average daily air mass-independent Linke turbidity T_{LI} information. Average daily T_{LI} factors were then used to correct temporally and spatially local aerosol loading and water vapor content. Compared to monthly climatologies, the *rRMSE* and *rMBE* of CSMs that used daily climatologies were lower by approximately one order of magnitude. This result suggests that daily turbidity information should be used for DNI clear-sky modeling, which is in agreement with the findings of Remund et al. [3].

While remote sensing techniques are available for turbidity calculation (MODIS aboard

NASA's AQUA/TERRA), the strict sampling rate of PLEOs may not be sufficient for accurate DNI clear-sky modeling; see Appendix A. It should be noted that this issue may be solved by new generation instrumentation on future geosynchronous satellite campaigns, e.g. GOES-R scheduled for launch in 2016. In this work, a persistence forecast, which employed lagged turbidity information, resulted in an *rRMSE*, which increased by 2 with respect to daily climatologies. The *rMBE* remained unchanged, which is a result of the persistence turbidity time-series being unbiased in its error distribution. As a result, we recommend that CSP plants use existing broadband pyrheliometers and endogenous cloud filtering techniques to correct local turbidity fluctuations.

Error analysis of the ground bases sensing CSM as a function of zenith angle suggests that the *rRMSE* is typically bounded by 5% (50 W m^{-2}) and can be as low as 0.5% (5 W m^{-2}) for solar zenith angles less than 30°. Also, the positive and notably small magnitude (1–3%) of the *rMBE* of the improved model suggests that the algorithm only slightly overestimates DNI which is typically desirable for CSMs which should provide an outer envelope of available irradiance and can also be used in the detection of cloud enhancement of irradiance [64]. The substantial reduction of *rRMSE* and *rMBE* of the improved DNI CSM over a wide range of solar zenith angles indicates that increased accuracy is achievable with minimal resources. The improvement appeared to be very weakly dependent on location, as we observed similar improvements in nearly all micro-climates. The proposed approach is, therefore, simple to implement, computationally inexpensive, and geographically robust.

Although the CSM employed in this work is based on an inversion of the definition of T_{LI}, the algorithm applies to any turbidity-based CSM. The key to the improvement is the observation of the inverted parameter under clear-skies, which is then assumed to persist.

2.9 Acknowledgement

This chapter, in full, is a reprint of R. H. Inman, J. G. Edson and C. F. M. Coimbra (2015) “Impact of Local Broadband Turbidity Estimation on Clear Sky Models for Direct Normal Irradiance,” *Solar Energy* (117) pp. 125–138. The dissertation author is the first author of this publication.

Chapter 3

Cloud Enhancement of Global Horizontal Irradiance in California and Hawaii

3.1 Introduction

The total extraterrestrial beam irradiance incident on the earth's atmosphere I_0 fluctuates about an average value of approximately 1360 W m^{-2} [16]. This incident radiation negotiates its way to ground level attenuation occurs through a complex series of multiple reflections, absorptions, and re-emissions due to interactions with atmospheric constituents [65]. These interactions result in the division of the incident extraterrestrial beam radiation into two distinct components; Direct Normal Irradiance (DNI) and Diffuse Horizontal Irradiance (DHI), the geometric sum of which is the Global Horizontal Irradiance (GHI), defined by the closure equation (2.4), see Fig 3.1. In addition to the partitioning of the radiation, atmospheric cloud-formation can cause a pronounced decrease in the intensity of solar irradiance components. The attenuation of incoming solar radiation by clouds is routinely more significant than any other atmospheric component [7]. Furthermore, the driving effects of clouds on radiative energy budgets include short wave cooling, as a result of absorption of incoming solar radiation, and

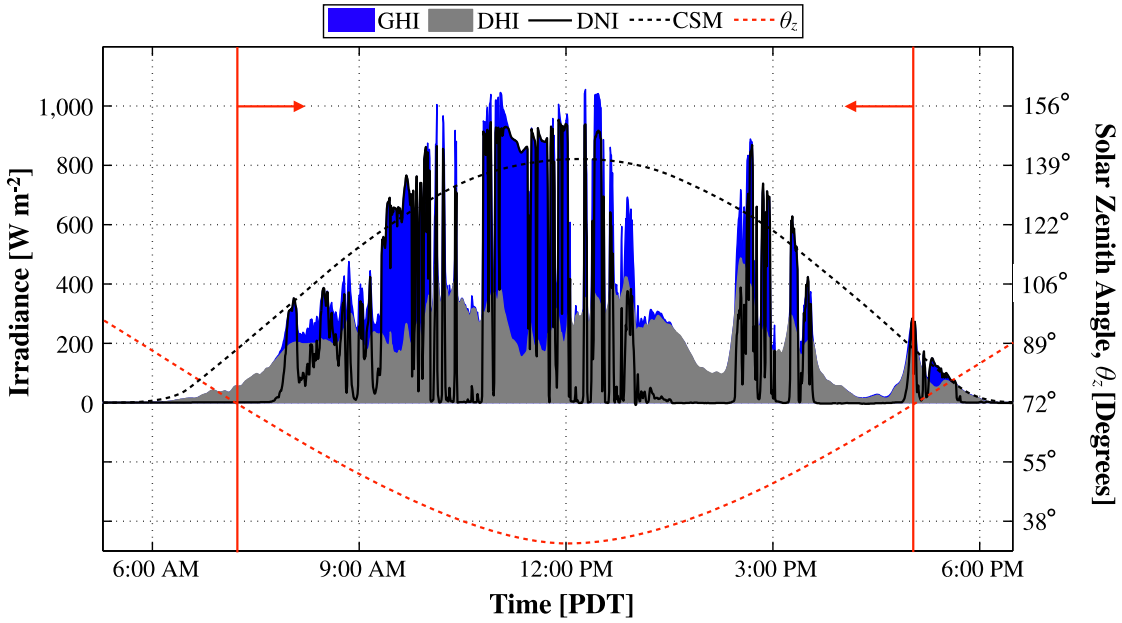

Figure 3.1: Components of solar irradiance sampled every 30 s at the University of California, Merced, on March 21, 2011. Global Horizontal Irradiance (GHI) was measured with a Precision Spectral Pyranometer (PSP), manufactured by the Eppley Laboratory, Inc. Direct Normal Irradiance (DNI) was measured using a Normal Incidence Pyrheliometer (NIP) and 2-axis automatic solar tracker (SMT-3), both of which are also available from the Eppley Laboratory, Inc. Diffuse Horizontal Irradiance (DHI) was measured using an additional PSP and SMT-3 with accompanying Shade Disk Kit (SDK). Solar zenith angle is also plotted and observations with $\cos\theta_z \leq 0.3$ ($\theta_z \geq 72.5°$), shown outside solid red-lines, being excluded from the study. The Clear-Sky Model (CSM) used in this figure is explained in detail in Section 3.3.2. (For interpretation of the references to color in this figure legend, the reader is referred to the web version of this article.)

longwave heating, due to reduced emission of thermal radiation by relatively cool cloud tops [66]. However, partly cloudy skies may lead to the reverse; i.e., multiple scatterings and reflections of short wave radiation by cloud fields may lead to increased irradiance from a portion of the sky above the corresponding cloud-free value [67, 68, 69, 70, 71, 72]. On rare occasions, these enhancements can cause the local GHI to instantaneously exceed the extraterrestrial solar constant I_0 [73, 64]. We refer to such enhancement of GHI above the corresponding clear-sky value as Cloud Enhancement Events (CEEs).

Except for two studies, one by Luoma et al. [74] and a second by Tapakis and Charalambides [64], little work has been done in the realm of CEEs concerning PhotoVoltaic (PV) power generation. In this work, we do not intend to suggest a new mechanism by which CEEs occur, but rather investigate the coherent Ramp Rates (RRs) associated with CEEs and their potential impact on the quality of PV power generation. Specifically, we define a coherent CEE RR as a series of monotonically increasing or decreasing GHI observations whose maximum value exceeds the expected clear-sky value by a given threshold. These CEEs and their associated RRs are of interest for several reasons: current models typically do not consider the ability of clouds to increase the locally available irradiance, these events commonly precede or follow periods of lower than normal irradiance associated with the presence of passing opaque clouds leading to relatively large RRs, large RRs can cause voltage flicker that in turn trigger tap chargers on distribution feeders increasing operations cost for utilities, and therefore the successful forecasting of these events could lead to an effective control scheme to reduce the cost associated with high levels of variability in photovoltaic power generation.

Analysis of the amplitude, persistence, and frequency of occurrence of ground-level irradiance fluctuation requires a decomposition of the input time-series into a set of orthogonal sub-signals, each representing a specified timescale of fluctuation. Due to the stochastic and nonperiodic nature of the atmospheric processes that drive ground-level fluctuations in clearness, Fourier analysis is typically not suitable. Alternatively, the literature contains examples of spectral

analysis of high frequency (e.g., 1 s to 1 min) irradiance time-series on a wavelet basis rather than a periodic basis can. Kawasaki et al. [75] decomposed 2- years of 1-min irradiance data from 9 sites in a 4×4 km grid using the Daubechies 4 wavelet [76]. Woyte et al. [77] applied the Haar wavelet [78] to clearness index time-series and defined a fluctuation power index (fpi) that quantified the amplitude and frequency occurrence of variability on specified timescales. Perpiñán and Lorenzo [79] analyzed several days of 1 s irradiance time-series using the MOD-WT wavelet. They later used wavelet transform correlations to study fluctuations of the electrical power generated by an ensemble of 70 DC/AC inverters from a 45.6 MW PV plant [80]. Lave et al. [81] applied wavelet transforms to clear-sky index time-series from a single site to the average of six sites and showed a strong reduction in variability at short timescales (i.e., shorter than 5-min) with lesser reductions at longer timescales. Lave et al. [82] also developed a wavelet-based variability model for PV plant output, and employed the wavelet-based model to study the impact of cloud speed on solar variability scaling. Similarly, Peled and Appelbaum [83] used statistical tools and wavelet analysis to develop estimators for the magnitude of voltage and power variations within PV systems due to climatic conditions.

These events operate on timescales ranging from seconds [66], to 15–30 min [84, 64], and occasionally as long as hours [85]. Here we employ a wavelet decomposition using the top-hat wavelet to show that while the CEE RRs typically only last a few minutes, they correlate with variability on longer time-scales associated with the passing of cloud fields.

This study uses a full year of irradiance data recorded at the University of California, Merced. We also use nearly five months of irradiance data recorded at the University of California, San Diego, and South Oahu, Hawaii, see Section 3.2. We describe methods in Section 3.3, which includes descriptions of the clear-sky model, statistical analysis, ramp rate calculation, wavelet decomposition, and fluctuation power index analysis. We cover the results and conclusions of these analyses in Sections 3.4 and 3.6, respectively.

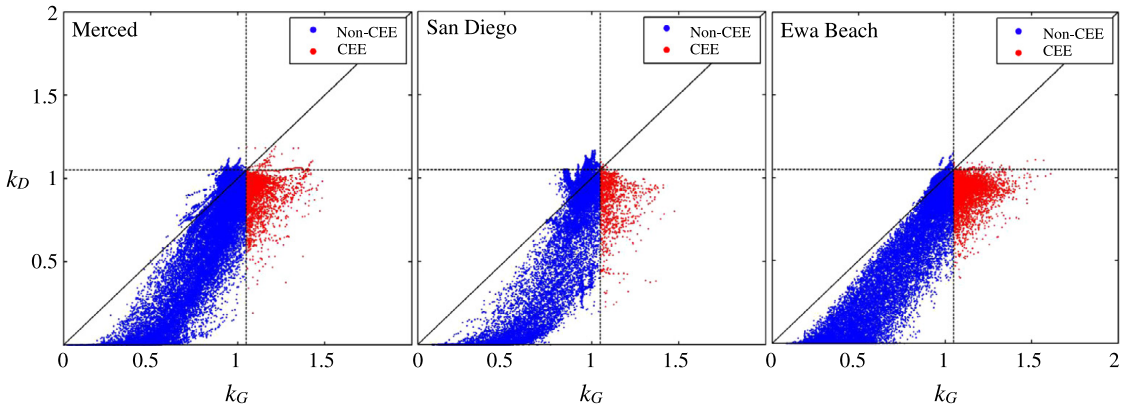

Figure 3.2: Scatter plots of k_D versus k_G for irradiance measurements in Merced, CA (left); San Diego, CA (center); and Ewa Beach, HI (right). Each marker stands for a single observation. Red markers represent GHI CEE cases and the dashed lines represent the 1.05 threshold for both k_D and k_G. (For interpretation of the references to color in this figure legend, the reader is referred to the web version of this article.)

3.2 Data

3.2.1 Irradiance data

We collected irradiance data at three locations characterized by different micro-climates: Merced California (continental), San Diego California (coastal), and Ewa Beach Hawaii (island). We used a broadband (285–2800 nm) Eppley Precision Spectral Pyranometer (PSP) and Normal Incidence Pyrheliometer (NIP) in Merced (March 21, 2011, to June 19, 2012) to collect GHI and DNI data, respectively. Two Multi-Filter Rotating Shadowband Radiometers (Model MFR-7), available from Yankee Environmental Systems (YES), which measure both GHI and DNI are used to collect irradiance data in San Diego and Ewa Beach during the period from January 27, 2012, to June 17, 2012. A Campbell Scientific CR-1000 data-logger logs all data at a sampling rate of 30 s. It is important to note that due to the 30 s sampling rate used in this study, the observed RRs are likely lower than those associated with an increased sampling rate; see, for example, [86, 87, 88].

Table 3.1: Table listing total number of days included in the study, observations that met the closure equation quality control, percentage of the observations classified as clear, average airmass independent Linke turbidity factor T_{LI}, and standard deviation of the distribution of T_{LI} for each site.

	Correlation coefficient		
	Overall	Non-CEE	CEE
Merced	0.9	0.92	0.07
San Diego	0.9	0.91	-0.16
Ewa Beach	0.94	0.95	-0.03

3.2.2 Selection of GHI

This work focuses on GHI rather than DNI due to the nature of the cloud enhancement process. CEEs are necessarily observable in the diffuse component of irradiance and, as a result of Eq. (2.4)Manifest in the global component of irradiance. This is because CEEs result from clouds elevating short wave diffuse irradiance above that of the corresponding clear-sky value with little or no change in DNI, which is illustrated through an analysis of DNI clear-sky indices,

$$k_D(t) = \frac{D(t)}{D_{clr}(t)} \tag{3.1}$$

and GHI clear-sky indices

$$k_G(t) = \frac{G(t)}{G_{clr}(t)} \tag{3.2}$$

where we generate D_{clr} and G_{clr} from the Clear-Sky Model (CSM) described in Section 3.3.2. As shown in Fig. 3.2, k_D generally increases with k_G for non-CEE periods and typically results in correlation coefficients greater than 0.9, which is expected (see Table 3.1). On the other hand, during CEE periods, the correlation between k_D and k_G is low, and in some cases, negative (see Table 3.1). It is also clear that during CEE periods, k_G is typically in the range of 1.05 to 1.5, while k_D tends to occupy the range from 0.5 to 1.0. It is also important to note that there are some

occasions where k_D did exceed 1.05; however, such enhancement was found to result from errors in the DNI CSM at elevated zenith angles under cloudless skies and, as a result, were excluded from the study.

3.3 Methods

3.3.1 Data quality

We exclude data from the early morning and late afternoon from the analysis. There are several motivations for their removal: primarily, the cosine response of pyranometer measurements are typically maximized for $\theta_z \geq 70^\circ$; secondly, times when $\theta_z \geq 70^\circ$ are associated with a relatively high airmass resulting in a large fraction of GHI originating from the diffuse component; and finally, the high solar zenith angle in combination with an elevated airmass results in rather low photovoltaic power production. To this end, a threshold is applied to the solar zenith angle θ_z according to,

$$\cos\theta_z \geq 0.3, \tag{3.3}$$

with data not satisfying Eq. (3.3), which corresponds to $\theta_z \geq 72.5^\circ$, being removed from the data set, see Fig. 3.1.

Furthermore, in order to avoid erroneous observation of CEEs resulting from reflections from local surfaces, a quality filter based on the summation method to obtain GHI was used [60]. This filter calculates GHI from Eq. (2.4) and compares it against the independently observed GHI. We excluded observations where the ratio of calculated and observed GHI differ from 1.0 by more than 0.2 as they typically correspond to an error in the observation of at least one irradiance component.

3.3.2 Clear-sky model

In addition to the measured irradiance data, a Clear-Sky Model (CSM) is used to characterize events that exceed the clear-sky ceiling. We model the clear-sky GHI using the CSM developed by Ineichen and Perez [46], which requires Linke Turbidity as an input. Maps of monthly average Linke Turbidity developed by Remund et al. [3] were used. These maps account for seasonal changes of aerosol content in the atmosphere, and their performance has been confirmed internally by Sandia National Laboratories [6]. We calibrated the CSM with several clear days and used a linear fit to ensure agreement between measured and modeled values.

3.3.3 Statistical analysis

We carried out statistical analysis to characterize the individual events that exceed the CSM into bounded ranges. Only GHI measurements that exceed the CSM by at least 5% and satisfy Eq. (3.3) are considered potential CEEs. We then grouped potential CEEs by the degree to which they exceed the CSM (5–10%, 10–15%, etc.). Statistical analysis of these subsets of CEEs provides insight into the distribution and probability of GHI measurements as a function of the degree to which they exceed the CSM.

3.3.4 Ramp rate analysis

Analysis of the RRs uses the same GHI data from the statistical study, excluding those violating Eq. (3.3) or the quality filter. As was done in Section 3.3.3, only events which exceed the CSM by a threshold of at least 5% are considered potential CEEs. However, rather than grouping the individual measurements by the range with which they exceed the clear-sky model (5– 10%, 10–15%, etc.), the present study employs a sliding lower bound which classifies coherent ramps by the amount with which their maximum value exceeds the CSM (>5%, >10%, etc.), see Fig. 3.3.

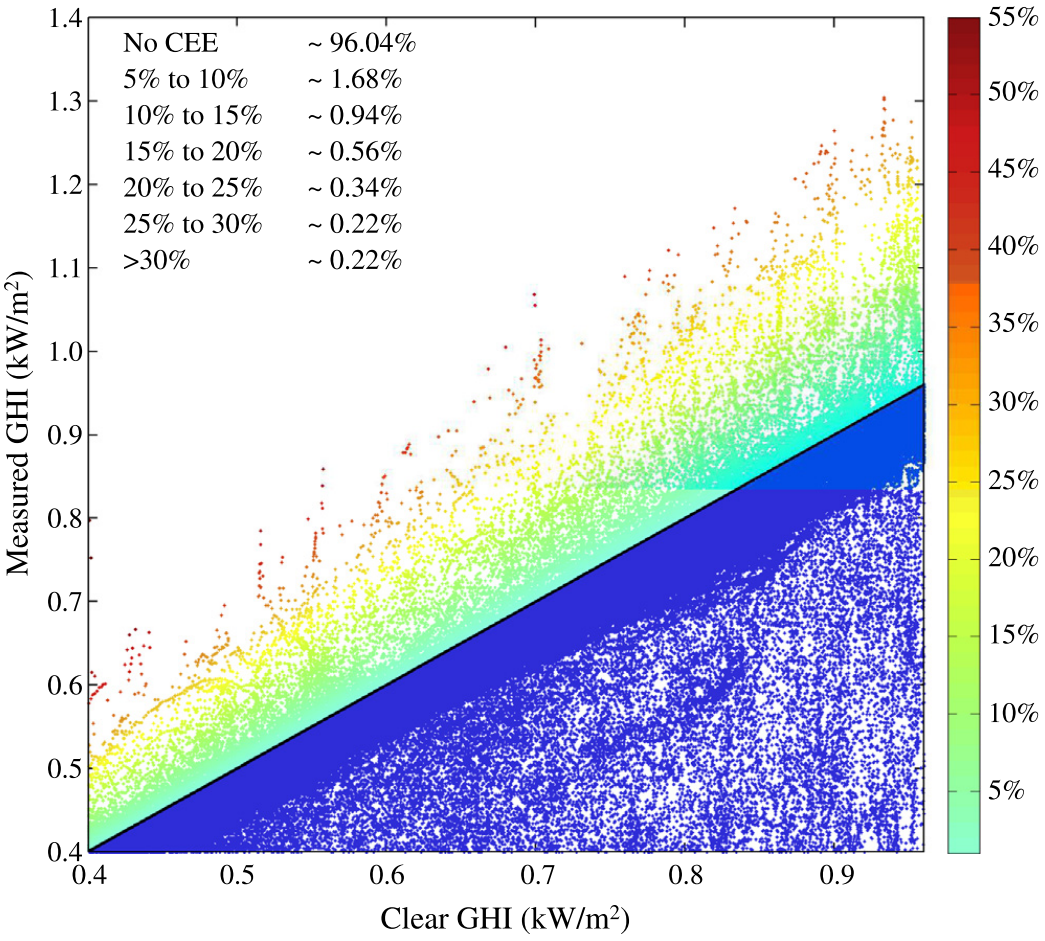

Figure 3.3: Plot of the entire year of GHI data from Merced as a function of the expected clear-sky value illustrating the set of potential CEEs.

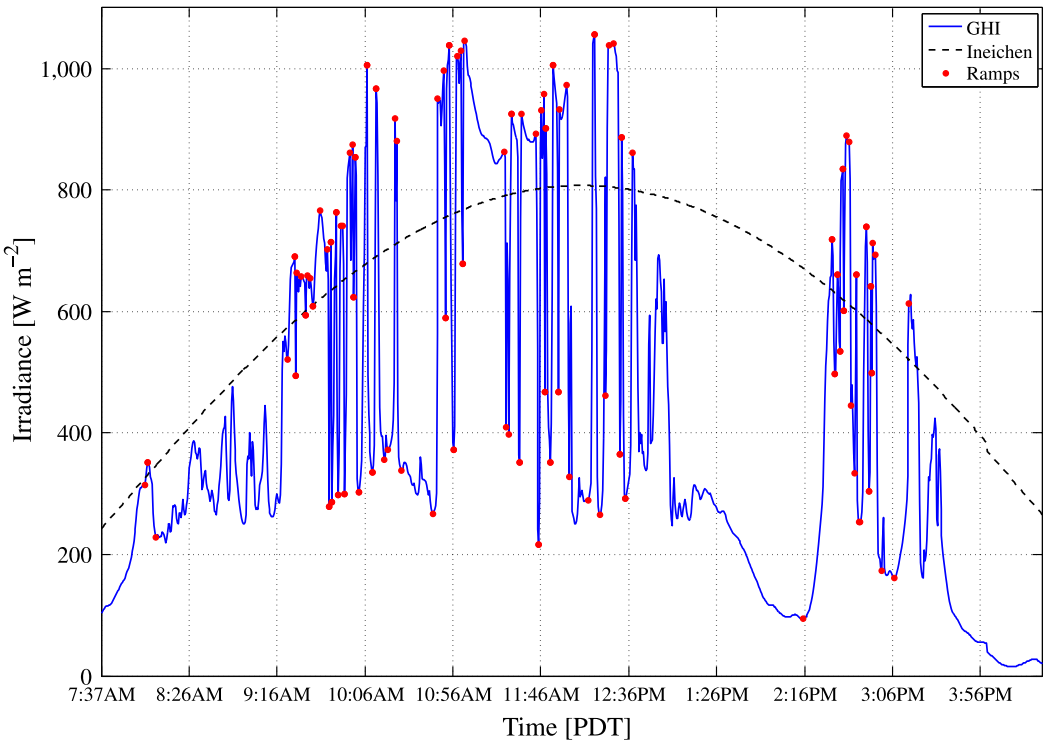

Figure 3.4: Ineichen clear-sky model as well as GHI data from the Eppley PSP located in Merced for the portion of March 21, 2011, satisfying Eq. (2.4). The local maxima and minima of the coherent ramps associated with CEEs are highlighted in red. Coherent CEE ramps are a set of monotonically increasing or decreasing irradiance observations whose maximum exceeds the CSM by a specified threshold. (For interpretation of the references to color in this figure legend, the reader is referred to the web version of this article.)

In order to study the coherent CEE RRs, characteristic events must be located and quantified. We accomplish this through the identification of successive measurements that lie on opposite sides of the CSM. We then extrapolate these points to their respective local maxima and minima. This is illustrated in Fig. 3.4 in which the ramps associated with CEEs, along with their local maxima and minima, have been identified in the Eppley PSP data from March 21, 2011, in Merced. It is important to note that while we used raw GHI data to locate potential CEEs (and the degree to which they exceed the CSM) the calculation of the RRs themselves ignores deterministic diurnal variations through the removal of the CSM values as described below,

$$|RR| = \frac{(G_{\max} - G_{\mathrm{csm,max}}) - (G_{\min} - G_{\mathrm{csm,min}})}{\Delta t} \tag{3.4}$$

3.3.5 Wavelet analysis

Wavelet analysis allows for the decomposition of nonperiodic time-series into sets of orthogonal sub-signals representing fluctuations on specific time-scales, see for example [89]. In the present study, a wavelet similar to the top-hat wavelet employed by Lave et al. [81, 82] is also used here. The top-hat wavelet used here is centered at zero and is defined as,

$$\psi(t) = \begin{cases} 1 & \text{if} \quad -1/4 < t < 1/4 \\ -1 & \text{if} \quad -1/2 < t < -1/4 \quad \bigvee \quad 1/4 < t < 1/2 \\ 0 & \text{else} \end{cases} \tag{3.5}$$

so that the dictionary of top-hat atoms can be written,

$$\mathcal{D} = \left\{ \psi_{\tau,2^j}(t) = \frac{1}{\sqrt{2^{j+1}}}\, \psi\left(\frac{t-\tau}{2^j}\right) \right\}_{\tau \in \mathbb{R},\ j \in \mathbb{Z}^+} \tag{3.6}$$

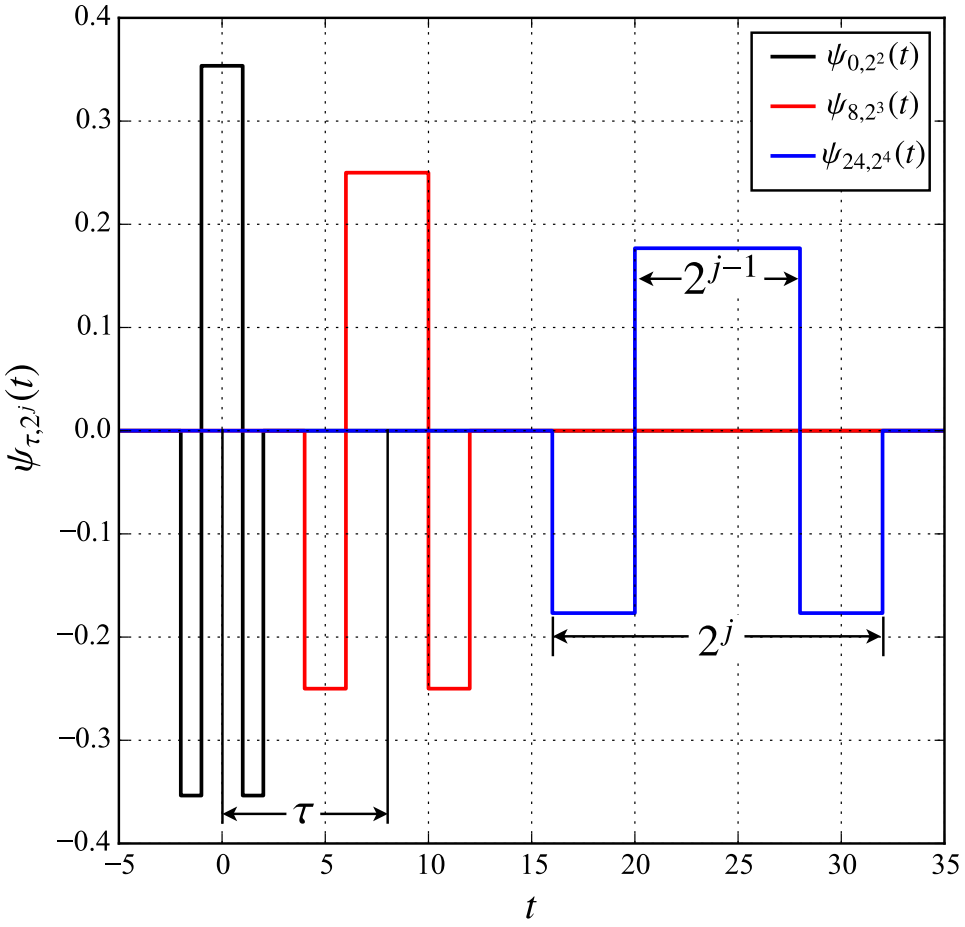

Figure 3.5: Illustration of the $\psi_{0,2^2}(t)$ top-hat wavelet centered at zero as well as two scaled, dilated and translated versions of the wavelet $\{\psi_{8,2^3}(t), \psi_{24,2^4}(t)\}$.

where the wavelet has been offset by τ and scaled by $1/\sqrt{2^{j+1}}$ to compensate for the length of the wavelet. The corresponding wavelet transform is written

$$\Psi f(\tau, 2^j) = \frac{1}{\sqrt{2^{j+1}}} \int_{-\infty}^{\infty} f(t)\, \psi\left(\frac{t-\tau}{2^j}\right) dt \tag{3.7}$$

To illustrate, Fig. 3.5 shows the $\psi_{0,2^2}(t)$ top-hat wavelet centered at zero and two scaled, dilated, and translated versions of the wavelet $\left\{\psi_{8,2^3}(t), \psi_{24,2^4}(t)\right\}$. These wavelets, which have a length of 2^j, when applied to a stationary time-series of irradiance measurements, would capture clear periods of length 2^{j-1} surrounded by overcast periods or vice versa.

In order to determine the power contained in each of the time-series $\Psi f(\tau, 2^j)$, a wavelet periodogram $I_j(\tau)$ is calculated. In analogy to the Fourier periodogram as well as the work by Woyte et al. [77] and Lave et al. [81, 82] we define the wavelet periodogram as the square of the wavelet transform, normalized by the period of the wavelet,

$$I_j(\tau) = \frac{\left[\Psi f(\tau, 2^j)\right]^2}{2^{j+1}} \tag{3.8}$$

However, information regarding the variability from the wavelet periodograms are inconvenient to examine periods longer than a day. To remedy this, we use a fluctuation power index as described by Woyte et al. [77] and employed by Lave et al. [81] here to characterize the amount of power included in each time-scale. We define the fluctuation power index (fpi) as,

$$\text{fpi}(j) = \frac{1}{T_j} \int_0^{T_j} \frac{\left[\Psi f(\tau, 2^j)\right]^2}{2^{j+1}} d\tau \tag{3.9}$$

where T_j is the total duration of the wavelet periodogram $I_j(\tau)$. Readers should note that while all of the definitions concerning wavelet transforms have been written in the continuous sense, our dataset is discrete. Therefore, we must employ discrete forms of Eqs. (3.6)-(3.9). The discrete

forms are,

$$\mathcal{D} = \left\{ \psi_{\tau,2^j}(t) = \frac{1}{\sqrt{2^{j+1}}} \psi\left(\frac{t-\tau}{2^j}\right) \right\}_{\tau \in \mathbb{N},\, j \in \mathbb{Z} \geq 2}, \tag{3.10}$$

$$Wf(\tau, 2^j) = \frac{\Delta t}{2\sqrt{2^{j+1}}} \left[f(0)\psi\left(\frac{-\tau}{2^j}\right) + f(N)\psi\left(\frac{N-\tau}{2^j}\right) + 2\sum_{t=1}^{N} f(t)\,\psi\left(\frac{t-\tau}{2^j}\right) \right], \tag{3.11}$$

$$I_j(\tau) = \frac{\left[Wf(\tau, 2^j)\right]^2}{2^{j+1}}, \tag{3.12}$$

and

$$\text{fpi} = \frac{\Delta t}{2T_j\sqrt{2^{j+1}}} \left[I_j(0) + I_j(T_j) + 2\sum_{t=1}^{T_j-1} I_j(t) \right], \tag{3.13}$$

respectively, where $\mathbb{N}$ represents integers between 2^{j-1} and $N - 2^{j-1}$.

3.4 Results

3.4.1 Statistics

A plot of the entire year of GHI data from Merced and suspected cloud enhancement events where the measured GHI exceeds the modeled clear-sky ceiling are shown in Fig. 3.3. Allowing for errors in the measurement of GHI and modeling of clear-sky irradiance ceiling, potential enhancement events are associated with measured values which exceed the clear-sky model by at least 5%. Our analysis shows that 10,228 of the 262,281 data points, corresponding to approximately 4potential CEEs. Multiplying the number of potential data points by 30 s time-steps corresponds to over 3.5 full days of these events per year if considered sequentially. The surplus irradiance enhancements range from 18 W m^{-2} day^{-1} to 73 W m^{-2} day^{-1}. We measured the maximum GHI in Merced on May 8th, 2011, at 12:08 p.m. ($\theta_z = 20.5^\circ$) with a value of 1,365 W m^{-2}, or approximately equal to the extraterrestrial beam irradiance I_0. This value is nearly 40% higher than the modeled clear-sky ceiling suggesting substantial gains may result from these events.

Table 3.2: Statistical results for CEE analysis for an entire time period (456 days) in Merced, CA.

Threshold	Mean	Standard deviation	Occurrence	Probability	Surplus energy	
	(W m^{-2})	(W m^{-2})	(-)	(%)	(W h m^{-2})	(W h m^{-2} day^{-1})
5-10\5	53	16	4238	1.62	1850	4.06
10-15%	91	21	2660	1.01	2010	4.41
15-20%	125	25	1483	0.57	1540	3.38
20-25%	157	37	890	0.34	1170	2.57
25-30%	195	46	575	0.22	930	2.04
≥30%	249	56	382	0.15	790	1.73
Total	95	58	10228	3.9	8300	18.19

Table 3.3: Statistical results of CEEs at three observatories for the time period when all data from all sites was available (142 days).

Location	Range	Mean	Std dev	Probability	Surplus energy		Frac of total GHI
	(-)	(W m^{-2})	(W m^{-2})	(%)	(W h m^{-2})	(W h m^{-2} day^{-1})	(%)
Merced	Jan 29-Jun 19, 2012	104	60	6.07	6430	45.3	1.2
San Diego	Jan 29-Jun 17, 2012	92	51	5.59	5370	38.4	1.0
Hawaii	Jan 27-Jun 17, 2012	101	52	10.71	10350	72.9	1.3

Statistical results from the data in Merced as well as similar results for data sets collected in San Diego and Ewa Beach, are shown in Tables 3.2 and 3.3, respectively, all of which recorded maximum values of GHI $\geq I_0$. The maximum recorded GHI in San Diego of 1396 W m^{-2}, which is 42.7% higher than the modeled clear-sky ceiling, occurred on May 25, 2012, at 12:45 p.m. ($\theta_z = 17.6^\circ$). Similarly, a maximum recorded value of 1380 W m^{-2}, which is 32.95% higher than the modeled clear-sky ceiling occurred on April 29, 2012, in Hawaii at 12:18 p.m. ($\theta_z = 7.2^\circ$). It is beneficial to note that the magnitude, mean, and deviation of these potential enhancement events across all three observatories do not vary significantly. Also, Merced's cloud enhancements are seasonally dependent and are more likely to occur in the spring months. Moreover, there are very few potential cloud enhancement events during the summer months when the skies are relatively cloudless over Merced. Due to the local climatology difference between Hawaii and California, there are fewer clear skies per year in Hawaii. Consequently, cloud enhancement events are more likely to occur and provide higher surplus local energy than the other two observatories during the same season, see Table 3.3.

3.4.2 Ramp rate probabilities

Cumulative Distribution Functions (CDFs) of the previously defined coherent CEE RRs are shown in Fig. 3.6. The CDF for the entire data set satisfying Eq. (3.3) is also shown for reference and labeled as 'Day Values.' Readers should note that, as a result of varying climates, cloud induced RRs vary by location. Cloud induced RRs resulting in a change of at least 5% in k_G for Merced, San Diego, and Hawaii account for 6.86%, 15.6% and 44.3% of the data, respectively. It is clear from Fig. 3.6 that the CEE RR distributions corresponding to increasing thresholds are quite similar. Also, one can see that CEEs are associated with elevated RRs. Fig. 3.6 also includes a horizontal line corresponding to $P = 0.95$. The intersection of this line with the CDFs represents the RR magnitude which is exceeded 5% of the time. This intersection occurs at approximately 76 W m^{-2} min^{-1} for the Day Values and an average value of 633 W m^{-2} min^{-1} for the CEE RR distributions. This suggests a significant increase in the probability of inflated RRs associated with CEEs. The inset of Fig. 3.6 shows the PDF of the 10% CEE RR case and the PDF for the Day Values. The PDF is included to show the symmetry of the CEE RR distribution. This symmetry indicates that each ramp is associated with a corresponding ramp of similar magnitude and opposite sign. This is to be expected from the passing of a discrete and opaque cloud field. This behavior is also clear from a careful examination of Fig. 3.4 and is summarized in Table 3.4. Only the 10% PDF case is shown for clarity, however, it should be noted that the remaining distributions are quite similar.

3.5 Wavelet decomposition

The wavelet transforms and periodograms from the clear-sky index for Merced at each time-scale, j = 1–7 for the entire year of data separated into days with and without CEEs of increasing thresholds were calculated. As mentioned in Section 3.3.5, it is important to note

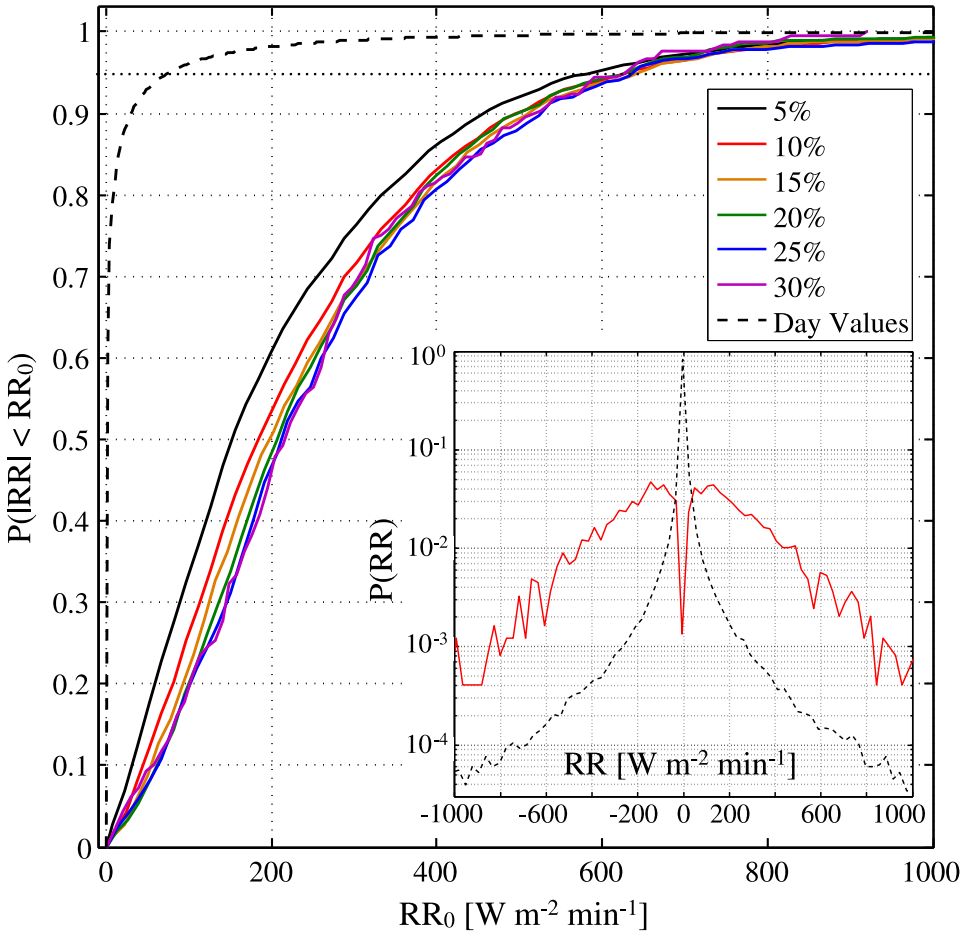

Figure 3.6: Cumulative Distribution Functions (CDFs) of the coherent Ramp Rates (RRs) whose maximum values exceed the CSM by an increasing threshold and are associated with Cloud Enhancement Events (CEEs). The CDF of the entire year of data that satisfy Eq. (3.3) is also shown for comparison and labeled as 'Day Values'. Intersection of the P = 0.95 line and the Day Values CDF occurs at 76 W m^{-2} min^{-1} and an average value of 633 W m^{-2} min^{-1} for the CEE RRs. Inset: Probability Distribution Function (PDF) of the Day Values as well the 10% threshold distribution showing the symmetry of RR associated with the passing of opaque clouds as well as the increased probability of elevated RRs.

Table 3.4: Data used in the calculation of $P(RR)$ separated into both up ramping events and down ramping events.

	$\sum_i \Delta t$ (Up RRs) (h)	$\sum_i \Delta t$ (Down RRs) (h)	$\sum_i \Delta t$ (CRR RRs) (h)
5%	67.81	66.36	134.2
10%	45.61	44.00	89.60
15%	29.11	29.54	58.65
20%	18.01	18.39	36.40
25%	12.11	11.88	23.98
30%	6.77	6.60	13.37
Year	3160		

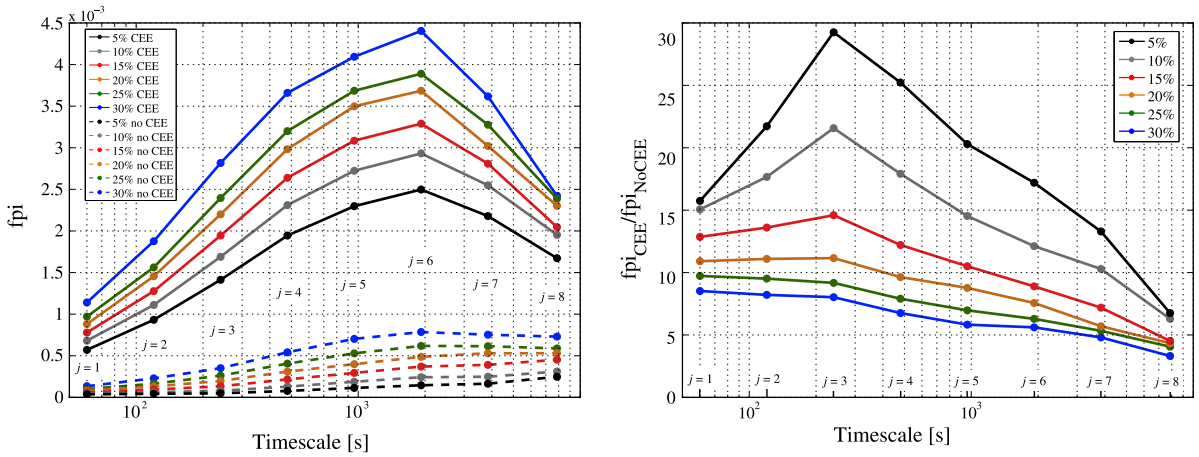

Figure 3.7: (a) Average annual fluctuation power indices as a function of time-scale and CEE threshold. Days without CEEs tend to possess fluctuation power indices that are typically 5–15 times lower in magnitude. Regardless of the time-scale (mode) all of the fluctuation power indices for a particular threshold are maximum at a time-scale of approximately 30 min ($j = 6$), suggesting that this is the dominant time-scale of clouds that are in turn responsible for CEEs. (b) Ratios of annual average fluctuation power indices of CEE to non-CEE days as a function of CEE threshold. Unlike (a), which show a peak at the $j = 6$ mode associated with approximately 30 min, the ratios show a peak at the $j = 3$ mode which is associated with a time-scale of approximately 4 min, suggesting that while the clouds that are responsible for creating CEEs tend to introduce variability on the order 30 min, the CEEs themselves tend to operate on time-scales about one eighth as long ($\sim$4 min).

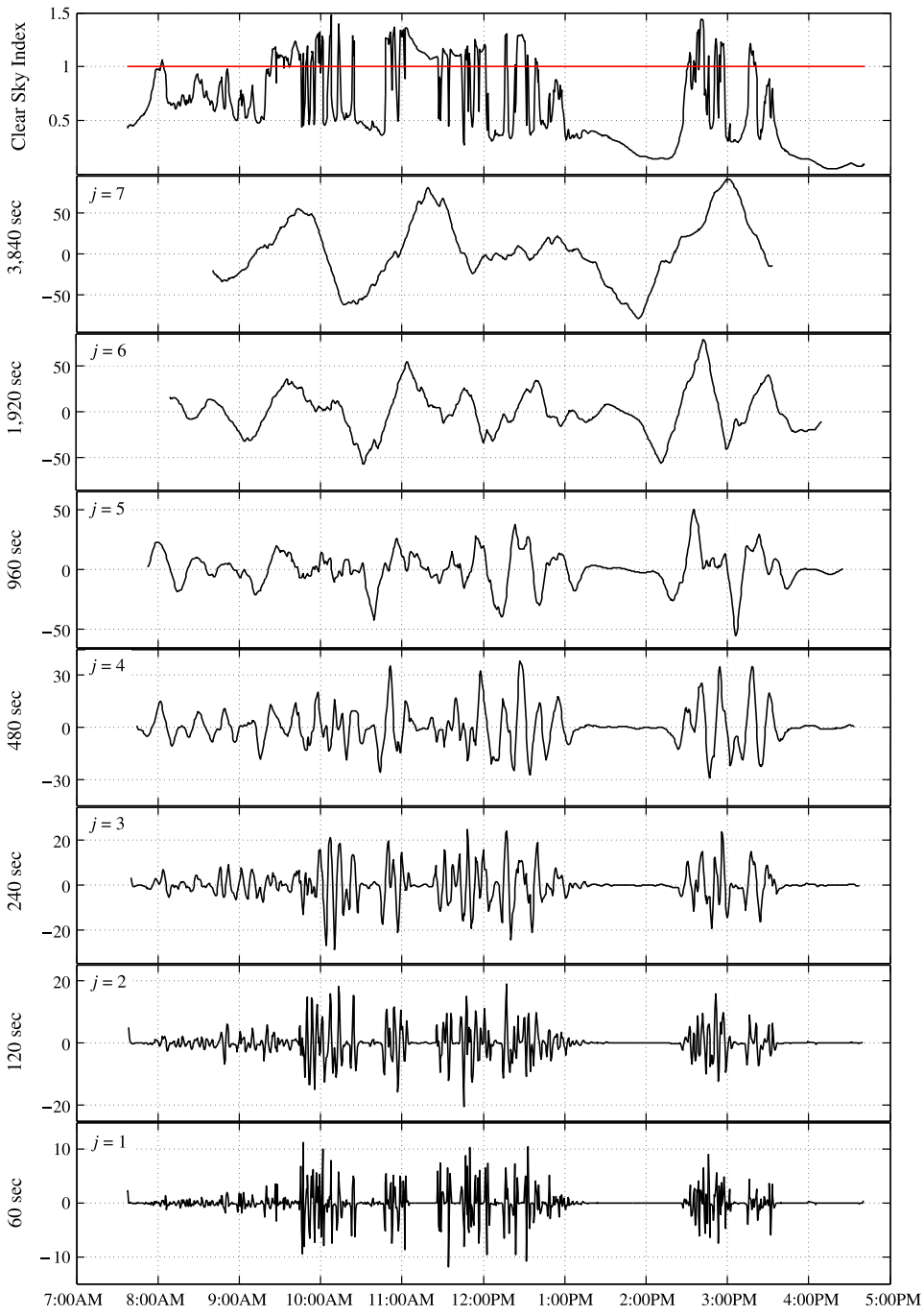

Figure 3.8: The wavelet transforms from the clear-sky index for Merced at each time-scale, $j = 1$ to 7 for the entire day of March 21, 2011 satisfying Eq. (3.3).

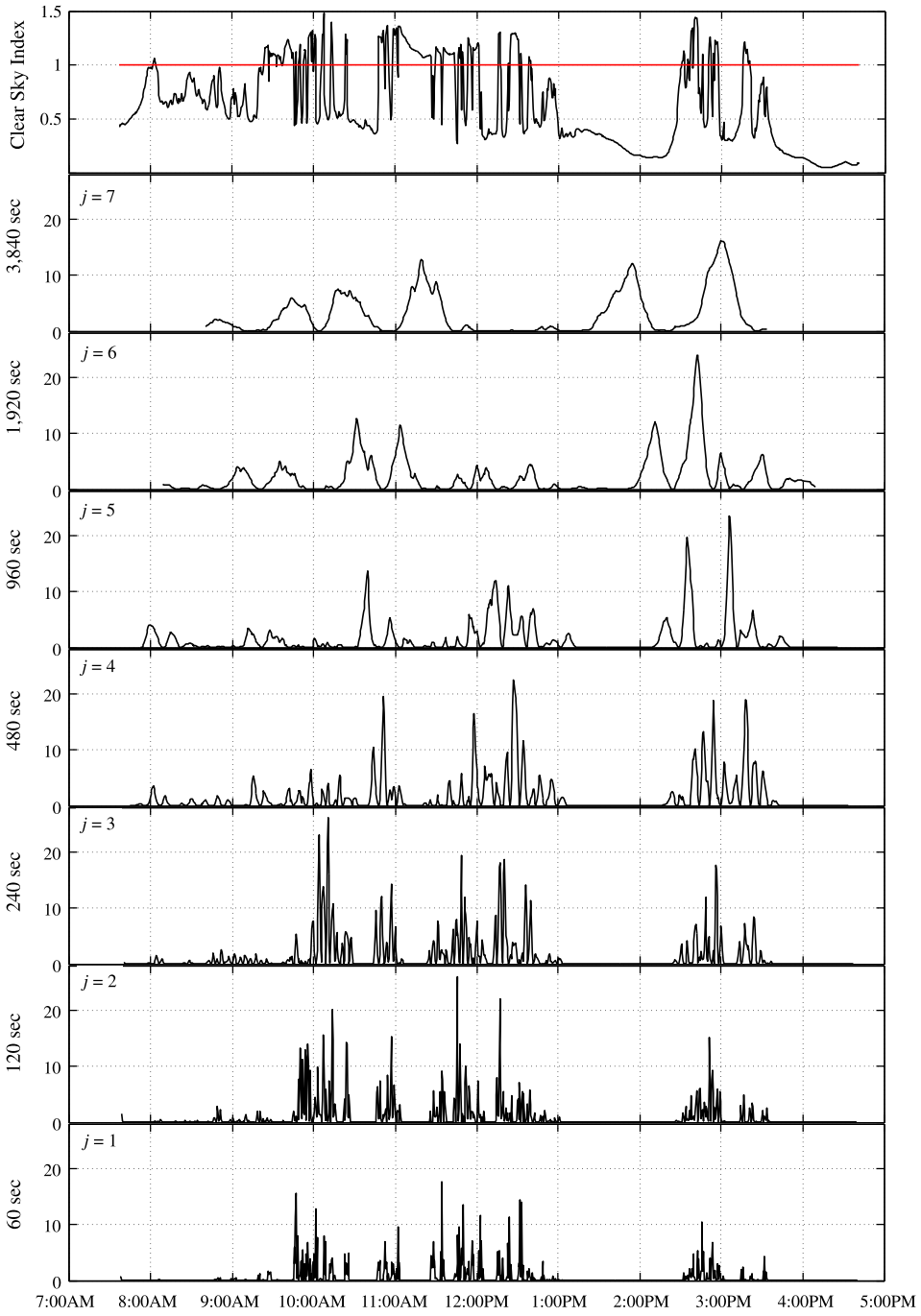

Figure 3.9: The wavelet periodogram from the clear-sky index for Merced at each time-scale, j = 1 to 7 for the entire day of March 21, 2011 satisfying Eq. (3.3).

that when the top-hat wavelet of time-scale j is applied to a stationary time-series of irradiance measurements, it captures clear periods of length 2^{j-1} surrounded by overcast periods or vice versa. The wavelet transform and periodogram for March 21, 2011 over modes $j = 1$ (60 s) to $j = 7$ (about an hour) are shown in Figs. 3.8 and 3.8, respectively. This day was chosen not only because it was used to illustrate the previous concepts but also because it has transitions between clear and cloudy periods at several time-scales, which would be detected by the top-hat wavelet transform. Upon inspection, it is clear from Fig. 3.8 that the wavelet transforms tend to be zero for times when no variability is present and increase in amplitude as fluctuations at the time-scale in question increase, as is to be expected. This is illustrated with clarity during the period from approximately 1:00–2:00 PM, where only the $j = 7$ mode has a non-zero amplitude while all other modes, i.e., $j = 1$–6 are nearly zero. This is a result of the cloudy period that lasts on the order of an hour with very little variability on shorter time-scales. This result is even more evident upon inspection of the periodograms in Fig. 3.9, where the periodogram is a non-negative number that increases in amplitude with the fluctuations at the time-scale in question.

As described in Section 3.3.5 the average annual fluctuation power indices are plotted as a function of time-scale (mode) and CEE threshold in Fig. 3.7(a). It is clear that days without CEEs tend to possess fluctuation power indices that are typically 5–15 times lower in magnitude, which is to be expected from the increased variability associated with the passing of cloud fields. However, regardless of the time-scale (mode) all of the fluctuation power indices for a particular threshold are maximum at the $j = 6$ time-scale, suggesting that this is the dominant time-scale of cloud-fields/weather-systems that are in turn responsible for CEEs. To clarify, this mode corresponds to a clear period of 15 min surrounded by overcast periods or vice versa, which is in agreement with the results from Kassianov et al. [90], which suggest that the typical decorrelation time for sky-cover is on the order of 15 min.

The ratio of the annual average fluctuation power indices of CEE to Non-CEE days are shown in Fig. 3.7(b) as a function of CEE threshold. This is performed in order to examine

the impact of CEEs at each time-scale; that is, at which timescale do the CEEs have the most impact. Unlike the results in Fig. 3.7(a), which show a peak at the $j = 6$ mode associated with approximately 30 min, the ratios show a peak at the $j = 3$ mode which is associated with a time-scale of approximately 4 min. This suggests that while the clouds that are responsible for creating CEEs tend to introduce variability on the order 30 min, the CEEs themselves tend to operate on time-scales about one eighth as long ($\sim$4 min).

3.6 Conclusions

This study investigates the observational frequency of CEEs and the associated coherent RRs. A statistical analysis showed that nearly 4% of the observations at Merced qualify as potential CEEs corresponding to nearly 3.5 days of CEEs per year. The increases above the predicted clear-sky ceiling for these CEEs ranged from 10 to 520 W m^{-2} and maximum GHI values on the order of 1300 W m^{-2} were observed at all three observatories. The maximum CEE was observed in San Diego on the 25th of May, 2012, with a value of nearly 1400 W m^{-2} , which was 43% higher than the modeled clear-sky ceiling.

Cumulative Distribution Functions (CDFs) show that CEEs are associated with elevated RRs. For days with no CEEs RRs greater than 76 W m^{-2} min^{-1} occur only 5% of the time. On the other hand, for days containing CEEs RRs exceeding 633 W m^{-2} min^{-1} occur 5% of the time. In addition, Probability Distribution Functions (PDFs) were used to illustrate the CEE RR distributions' symmetry, which suggests that each CEE RR is associated with a ramp of similar magnitude and opposite sign.

Finally, wavelet decomposition coupled with fluctuation power index analysis shed light on the time-scales on which cloud induced variability and CEEs operate. An examination of the magnitude of the fluctuation power indices showed that regardless of the presence of CEEs, cloud induced variability tents to have a maximum fluctuation power index at the 30 min time-scale.

However, upon inspection of the ratios of the fluctuation power indices for both CEE and non-CEE at each time-scale showed a maximum increase at the 4 min time-scale, regardless of CEE threshold. In other words, this result suggest that while clouds tend to induce variability most strongly at the 30 min time-scale, they have the potential to cause CEEs that induce variability on time-scales of several minutes. This analysis clearly demonstrates that CEEs are an indicator for periods of high variability and therefore provide useful information for solar forecasting and integration.

3.7 Acknowledgement

This chapter, in full, is a reprint of R. H. Inman, Y. Chu, and C. F. M. Coimbra (2016) "Cloud Enhancement of Global Horizontal Irradiance in California and Hawaii," *Solar Energy* (130) pp. 128–138. The dissertation author is the first author of this publication.

Chapter 4

Experimental investigation of contra-flow pool evaporation at low Rayleigh numbers

4.1 Introduction

Evaporation of water into quiescent air from horizontal planar interfaces has been experimentally studied for nearly a century with various motivations and applications. Fishenden and Saunders [91] conducted one of the first experimental studies of thermally driven Horizontal Natural Convection (HNC) which was popularized by its inclusion in the work of McAdams [92]. This study correlated data from horizontal square plates exposed to air by employing the dimension of a side as the characteristic length scale. While the correlations from Fishenden and Saunders are historically relevant, it is worth noting that these correlations apply to pure heat transfer; i.e., concentration gradients were absent, and, as a result, no mass transfer occurred. Previous to these well known heat transfer studies, Sharpley and Boelter [93] performed a detailed experimental study of evaporation driven HNC. This study focused on the evaporation of distilled water from an approximately 30-cm-diameter surface flushed horizontally with the surrounding floor into stagnant air maintained near 295 K, for water temperatures ranging from 290-307

K and relative humidity (RH) values ranging from 50-54%. Notably, that study provided two correlations separated by a *buoyancy critical* region where buoyant effects at the water surface and far away were equal, resulting in a zero-valued Rayleigh (or Grashof) number. While this study contains some of the only experimental data with Rayleigh (or Grashof) numbers approaching and less than zero, the lack of detailed surface temperature measurements and the subsequent use of bulk liquid temperature in Rayleigh number calculations obviates direct comparison here. Later, Boelter, Gordon, and Griffin [5] presented data to supplement those in [93]; the updated correlations covered the evaporation of distilled water from the same 30-cm-diameter surface, except this time within the temperature range of 290-365 K, into air at 290-300 K and covering 54-98% relative humidity values. This second study primarily explored the *super-critical buoyancy range* of Grashof numbers and aimed to extend the analogy between thermal free convection and mass free convection to higher driving potentials and increasingly parabolic flows.

The intentional modulation of water temperatures relative to the ambient temperature allowed these studies [93, 5], to report mass transfer data on both sides of the critical buoyancy region, which is particularly relevant to the understanding of competing effects on this complex thermal process. These studies reported a reduced dependence of transfer rates on the density differences below the buoyancy critical region relative to those above the critical region, and the lowest transfer rates were attributed to the competing orientation of the driving potentials, see Fig 4.1. Explicitly, when the liquid was heated above a critical temperature, transfer rates had a stronger dependence on density differences because the thermal and concentration driving potentials acted in the same direction, i.e., away from the surface. In that case, the vapor flux at the interface dominated the flow, which the authors referred to as *parallel flow* evaporation. As concentration differences were reduced by lowering the liquid's temperature, evaporation rates also decreased, until the density of the mixture just above the interface was equal to the far stream, and the interface temperature reaches the critical value, which is lower than the far stream temperature for water evaporating into moist air at experimental conditions. The absence of

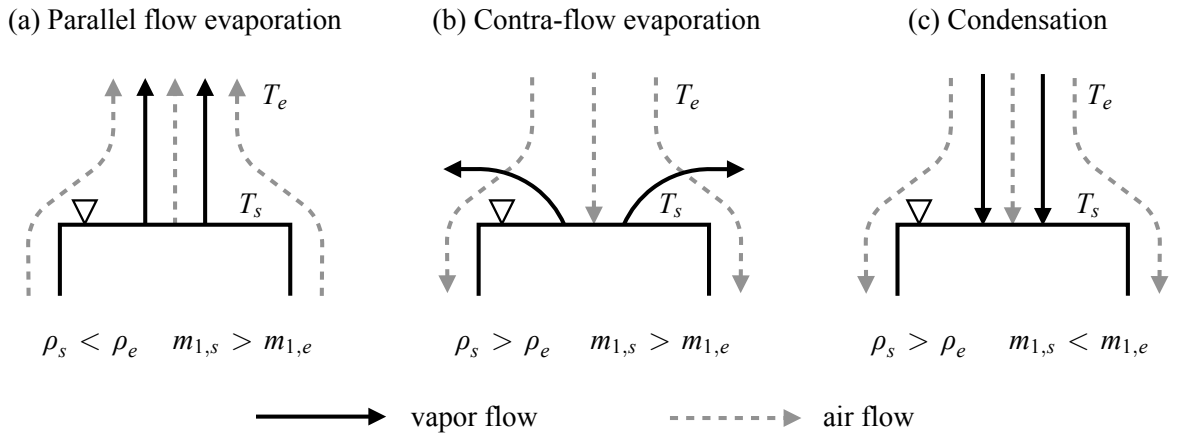

Figure 4.1: Schematic of mixture flow diagrams above the pool (adapted from [5]). Solid black lines indicate vapor flow, while dashed gray lines denote the air flow. (a) *Parallel flow evaporation* where the mixture density at the surface is less than the ambient mixture density and the vapor concentration is greater at the surface than the ambient concentration. This well studied regime is not the focus of this work. (b) In contract, *contra-flow evaporation*, which is the focus of our experiments, occurs when the mixture density at the surface becomes greater than the ambient mixture density, while the vapor concentration remains highest at the surface. This flow regime typically occurs when no external heat is added to the liquid. The decrease in temperature from the latent heat of vaporization causes a corresponding decrease in mixture density that is greater in magnitude than the conflicting decrease in mixture density resulting from vapor saturation. (c) *Condensation*, which we avoided in experiments, occurs where the mixture density at the surface is greater than the ambient, and the vapor concentration at the surface is less than the ambient vapor concentration.

density differences does not imply the absence of thermal or concentration gradients, which would continue to drive this weakly convective flow. At temperatures below the critical value, but above the dew point, evaporation rates showed weaker dependence on the density difference because the mixture was denser at the liquid surface. The thermal potential opposed the concentration potential, which previous authors referred to as *contra-flow* evaporation. These two regimes, *parallel flow* and *contra-flow* evaporation, will help discussions that follow and, accordingly, we adopt the same terminology for the remainder of this work.

While these pioneering studies provided valuable insights, the results were limited to circular or else square geometries with the diameter or else side of the interface as the characteristic length. Regarding the nature of the flow field resulting from free convection, with a particular emphasis on the influence of the shape of the surface that generates the flow, Husar and Sparrow [94], captured images of flow patterns adjacent to horizontal heated surfaces of various geometries. These images suggested that the length scale, $\mathscr{L} = A/P$, where A is the area of the interface and P is the perimeter of the interface, closely approximated the average horizontal distance traveled by fluid particles moving from the outer flow to the inner flow for flows directed away from the surface. Before the work of Husar and Sparrow, the use of geometry-independent length scales was not widespread; e.g., contemporary literature used the short side of a rectangle for correlations [95], where the authors suggested that the generalization of existing (albeit conflicting) square plate heat-transfer correlations to other planforms may benefit from such a geometry-independent length scale.

Later, Goldstein, Sparrow, and Jones [96] published the first correlations for natural convection mass transfer adjacent to horizontal plates that employed the characteristic length suggested by Husar and Sparrow [94]. Notably, the authors used this length scale to produce generalized correlations for circular, square, and 7:1 aspect ratio rectangular interfaces. The study in question employed the naphthalene sublimation technique, which, by the Chilton-Colburn analogy, corresponds to pure heat transfer from a heated isothermal upward-facing plate or

a cooled isothermal downward-facing plate. Despite the absence of additional buoyant and evaporative mechanisms, and at Schmidt numbers ($Sc = \nu_{air}/\mathscr{D}_{12}$) near 2.5, this study used the characteristic length of Husar and Sparrow [94] to advance data reduction for various horizontal geometries. In addition to the naphthalene sublimation experiments performed by Goldstein, Sparrow, and Jones [96], several analog electrochemical techniques were published around the same time [97, 98, 99] for fluids characterized by Schmidt numbers near 2200. The most relevant of those for the present work was the contribution by Lloyd and Moran [99], who also employed the characteristic length recommended by Husar and Sparrow [94] to derive generalized correlations for circular, square, rectangular, and right triangular planforms.

Nearly a decade later, Sparrow, Kratz, and Schuerger [100] performed the first rigorous experimental treatment of evaporation driven natural convection from horizontal surfaces with oppositional driving potentials since the work in [93, 5]. For the first time in nearly forty years, experiments were published in the sub-critical region where *contra-flow* thermal effects drove the mixture toward the interface rather than away from it. The authors used circular interfaces with the interface's radius as the correlating parameter despite the more generalizable approach by Husar and Sparrow [94]. Significantly, this study varied the length scale of the interface rather than the ambient conditions to modify the correlating parameter, as was done in [93, 5]. Specifically, Sparrow, Kratz, and Schuerger [100] employed five pans with diameters of 8.89, 12.82, 16.32, 22.18, and 30.68 cm, with relative humidities ranging from 16-40%, while the ambient temperature ranged from 268-275 K. Energy from the far stream was required to sustain evaporation since the water was not heated. Consequently, the interface's temperature was always less than the ambient with a temperature suppression ranging from 3-6 K. This method of modifying the correlating parameter is fundamentally different from the *contra-flow* evaporation experiments in [93, 5], which used the same interface geometry but modified the temperature of the interface via external heating or cooling.

Bower and Saylor [101, 102] performed the most recent *contra-flow* evaporation ex-

periments and employed sixteen square tanks having four depths and four widths. Similar to Sparrow, Kratz, and Schuerger [100], this most recent study modified the interface's length scale to extend the coverage of correlations rather than modifying the ambient as was done in [93, 5]. The authors also compared their results to those obtained by researchers outlined above [93, 5, 96, 99, 100]. Unfortunately, the study in question mismatched results that employed disparate length scales, which resulted in an inconsistent comparison of previous results; see Table 4.1 for an updated comparison of results with the correct length scales. Table 4.1 also includes several correlations for purely thermally driven flows above cooled and upward-facing isothermal plates [92, 103, 104], which are relevant when vapor concentrations in the ambient approach saturation, and concentration gradient effects are minimized. A correlation not included in Table 4.1 is that from Fujii et al. [103], which is more complicated and is reproduced below for convenience

$$Sh_{\mathscr{L}} = \frac{2.5}{\ln(1+2.5/Sh')} \tag{4.1}$$

where

$$Sh' = 0.391 Ra_{\mathscr{L}}^{0.2} \tag{4.2}$$

valid from $10^3 \leq Ra_{\mathscr{L}} \leq 10^{10}$.

Before moving on, it is important to note an additional parameter necessary to describe the complexity of the mass transfer effect on experimental correlations. That factor is the evaporation flux's influence on modifying gradients near water's surface and, therefore, the mass and heat transfer rates. Authors typically express this factor as $\mathscr{J}/\mathscr{J}^*$ (or Sh/Sh^*) as originally proposed by Spalding: [105]:

$$\dot{m}'' = \mathscr{J}_{m1}\mathscr{B}_{m1}; \quad \mathscr{B}_{m1} = \frac{m_{1,s} - m_{1,e}}{1 - m_{1,s}} \tag{4.3}$$

where

$$\frac{\mathscr{J}_{m1}}{\mathscr{J}^*_{m1}} = f(\mathscr{B}_{m1}). \tag{4.4}$$

Recently, Brewster [106] fit the data from Boelter et al. [5] over a range of water temperatures from 297 K to 367 K. Brewster's analysis was based on Spalding's self-similarity model and included the high mass transfer rate effects, e.g., $\mathscr{J}/\mathscr{J}^*$ (or Sh/Sh^*), for HNC where $\mathscr{B}_{m1}$ extended to approximately 20. Brewster defined the HNC correction as

$$\left(\frac{\mathscr{J}}{\mathscr{J}^*}\right)_{m,h} = \frac{1}{1+1.5\mathscr{B}_{m,h}^{0.8}} \tag{4.5}$$

The rather high values of the driving force $\mathscr{B}_{m1}$ explored in Brewster's analysis correspond to a temperature just below the boiling point of water. The reduction in the Sherwood at the upper limit of Brewster's analysis ($\mathscr{B}_{m1} \sim 20$) is significant, approaching a factor of 20, see Fig.2. While high mass transfer rate theory is relevant to high-Ra parallel flow regimes, such as spent-fuel pools [106], it is typically negligible for low-*Ra* conditions.

It is clear from the previous discussion that, despite the early focus on a point of inflection for mass transfer rates at at buoyancy-critical interface temperatures [93, 5], the majority of research that followed focused on refinements of single-mechanism natural convection or else combined heat and mass transfer in the super-critical buoyancy region associated with *parallel flow* evaporation [107, 97, 94, 98, 96, 99, 101, 102], rather than the sub-critical region where *contra-flow* evaporation prevails [100]. Additionally, we found no experimental studies that included opposing mechanisms at elevated relative humidities without an external energy source, i.e., at low driving potentials. Therefore, this regime is explored in greater detail in the present work, see Figs. 4.2 and 4.3.

We proceed with the classification of previous research efforts into two distinct flow regimes. In general, these regimes are concerned with the orientations and relative magnitudes of the thermal and concentration effects that drive free convection flow. In this classification, we introduce the ratio of dimensionless concentration driving potential to the dimensionless thermal driving potential, denoted N, see Eqn. (4.28), as the determining parameter to characterize flow

regimes as buoyancy sub-critical or super-critical. Readers may also view this parameter as the ratio of concentration Rayleigh (or Grashof) number to the thermal Rayleigh (or Grashof) number. While Pera and Gebhart [108] pointed out the significance of this parameter nearly forty years ago, it has only appeared sporadically in the literature since then. Here, we reintroduce this parameter as a way to characterize flows and illustrate the range of values of this parameter for which data may not exist in the literature. While the N parameter appears later in the context of 4.2.2 Eqn. (4.28), we define the parameter here for clarity:

$$N \equiv \frac{\gamma_i(\rho_{i,s} - \rho_{i,e})}{\beta(T_s - T_e)},$$

where, at the extremes, N is zero for pure heat transfer flow and approaches infinity (positive or negative) for mass transfer driven flows. Additionally, when both thermal and concentration effects are similar in magnitude, N approaches unity. While these limits are useful, as alluded to above, intermediate values provide additional context. Specifically, the sign of N indicates whether the thermal and mass transfer potentials added up (*parallel-flow*) or oppose each other (*contra-flow*), and the farther the value of N is from unity, the more dominant each contribution is.

As a result, four potential flow regimes exist, separated by three flow boundaries (with only three of the four regimes currently described in the literature), as depicted in Fig. 4.2.

Experiments at low concentration or thermal differences are challenging to perform because many smaller effects contribute to the overall rate of evaporation. Historically, most authors have designed experiments at approximately constant ambient vapor content but varied the length scale or surface temperature to modify the correlating parameter [93, 5, 96, 100, 101, 102]. Successively increasing the length scale, or surface temperature, necessarily extends the coverage of correlations to higher Rayleigh (or Grashof) numbers, all other relevant parameters being equal. However, this manipulation seldom justifies the extrapolation of results to lower Rayleigh numbers (driving potentials); i.e., no experimental manipulation of length scale or temperature

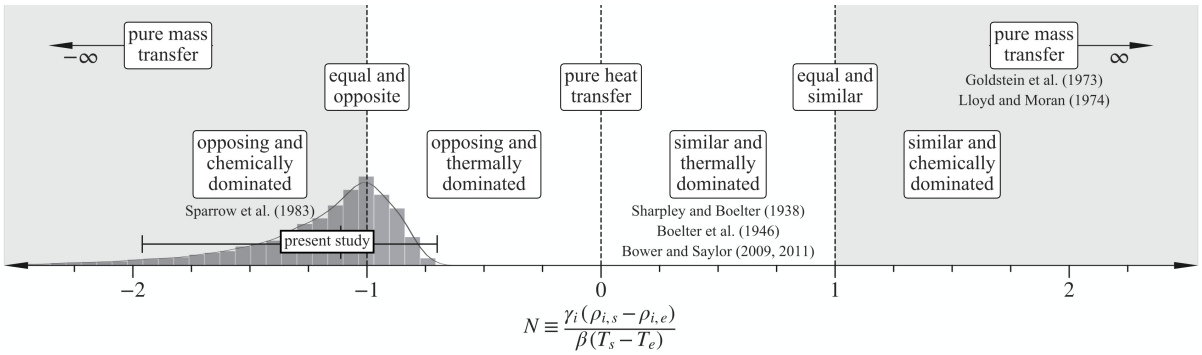

Figure 4.2: The dimensionless value of N as a parameter to categorize buoyant flows from horizontal surfaces into distinct regimes. The horizontal axis indicates values of N, which is defined as the ratio of dimensionless concentration to thermal driving potentials. The magnitude of N indicates either the concentration potential or the thermal potential as the dominant mechanism for flow direction. Gray regions denote areas for which the magnitude of N is greater than unity, associated with a dominant concentration potential, with limiting cases for isothermal processes indicated as *pure mass transfer* regimes. Contrarily, the region where $-1 < N < 1$ is un-shaded and indicates values of N associated with dominant thermal potentials for the flow direction. The sign of N indicates whether the potentials act in similar or opposite directions. Pure heat and mass transfer dominated flows occur when the magnitude of N approach zero or infinity. We have indicated all of the regions discussed above in boxes throughout the figure. We group some critical studies based on the values of N and place them in their corresponding location in the figure. Finally, a distribution of the values of N realized in the present study is shown along the lower-left portion of the figure.

alone can replace the modification of N via changes of the vapor content in the mixture. While the approaches employed in previous works are scientifically sound and are, in large part, responsible for our present experimental understanding of evaporation driven heat and mass transfer from horizontal surfaces, these approaches render the observation of evaporation rates at elevated ambient humidity values increasingly challenging to achieve. The reason for this becomes clear after considering how such an experiment might take place. One could imagine an experimenter observing transfer rates while somehow adjusting the experimental vapor content above/below the ambient laboratory conditions. Therefore, in contrast to the well-studied (and stable) flows discussed above, flows driven by comparatively low driving potentials require much a more sensitive apparatus that is considerably more sophisticated than those previously employed.

With the above in mind, we control the environmental conditions of our experiments using a custom-designed, temperature-controlled, stainless steel chamber to conduct *contra-flow* evaporation experiments that reproduce conditions often found in laboratory and industrial processes. We place a small open reservoir filled with distilled water inside the larger control volume (chamber) and first remove vapor from the control-volume using a forced-air mass exchanger containing a bed of desiccants. Once the bed of desiccants removes the desired quantity of vapor from the chamber, we commence gravimetric observation of mass transfer rates at low relative humidity values. As evaporation converts liquid water into water vapor, the ambient vapor concentration increases in this controlled environment. This procedure enables us to achieve detailed experimental results by allowing the transfer process to slowly vary the ambient vapor concentration while measuring the mass of liquid water in the cylindrical vessel *in-situ* at time scales much shorter than those associated with the transfer processes. In other words, there is practically no need to vary the size of the vessel to expand the range of Grashof numbers due to the wide variation of other parameters. Each experiment ends as a result of one of the three following conditions: either the surface of the water is no longer 'flat' due to the evaporation of liquid water from the pool resulting in meniscus-related effects, or the ambient

Table 4.1: Comparison of *Sh* – *Ra* power law coefficients and exponents from previous experimental studies. While not all of the original studies listed used the length scale $\mathscr{L}$, see Eqn. (4.9) we have, where necessary, scaled the coefficients accordingly. This conversion allows a unified comparison of previous results, regardless of the geometry of the employed interface. For consistency, in some cases, a constant factor of $Sc^{1/3} = 0.61^{1/3}$ is also absorbed into the numerical coefficient. The present work is excluded from this table because here we attempt to find a single correlation for a non-zero value of *Sh* that crosses the $Ra = 0$ value, and as a result, the form of the correlation in this regime requires an additional term. Specifically, $Sh(Ra) = B(Ra + C)^n)$, where we have added the offset *C*, see Eqn. 4.39.

Parameterization	$Sh_{\mathscr{L}} = A\,(Ra_{\mathscr{L}})^n$			
	A	n	Sc	$Ra_{\mathscr{L}}$ range
1. Fishenden and Saunders [91]	0.14	1/3	0.6	$2 \times 10^7 < Ra_{\mathscr{L}} < 3 \times 10^{10}$
2. Sharpley and Boelter [93]	0.541	0.213	0.6	$1.6 \times 10^4 < Ra_{\mathscr{L}} < 7.0 \times 10^5$
3. Boelter et al. [5]	0.371	0.241	0.6	$1.5 \times 10^5 < Ra_{\mathscr{L}} < 7.2 \times 10^6$
4. Goldstein et al. [96]	0.590	1/4	2.5	$2.0 \times 10^2 < Ra_{\mathscr{L}} < 5.0 \times 10^3$
5. Goldstein et al. [96]	0.960	1/6	2.5	$1.0 < Ra_{\mathscr{L}} < 90$
6. Lloyd and Moran [99]	0.150	1/3	2200	$8.0 \times 10^6 < Ra_{\mathscr{L}} < 1.6 \times 10^9$
7. Lloyd and Moran [99]	0.540	1/4	2200	$2.2 \times 10^4 < Ra_{\mathscr{L}} < 8.0 \times 10^6$
8. Sparrow et al. [100]	0.493	0.205	0.6	$2.5 \times 10^3 < Ra_{\mathscr{L}} < 1.1 \times 10^5$
9. Bower and Saylor [101, 102]	0.238	0.306	0.6	$1.5 \times 10^4 < Ra_{\mathscr{L}} < 8.9 \times 10^6$
10. Radziemska and Lewandowski [104]	0.538	0.2	0.6	$2.5 \times 10^3 < Ra_{\mathscr{L}} < 1.25 \times 10^6$

relative humidity reaches 85%, which is a physical limitation imposed by choice of instruments, or else the dew point inside the temperature is near the laboratory temperature which is avoided to prevent condensation onto sensitive instrumentation connected to the outside of the chamber. In the present work, we describe experiments at atmospheric pressure with the chamber temperature held constant at 285, 290, 295, 300, 305, and 310 K, with relative humidity ranging from 5 to 85%.

Section 4.2 covers the data and methods we employ in this study, including the choice of dimensionless parameters and length scale, conservation equations, a detailed description of the experimental apparatus as well as the novel algorithm used to derive experimental transfer rates. Section 4.3 contains the main results from the paper, including a justification for the statistical relevance of our transfer rate derivation and the dimensionless mass transfer correlations regressed from the experimental data. Sections 4.4 and 4.5 include a discussion of the results and a summary of the main conclusions, respectively.

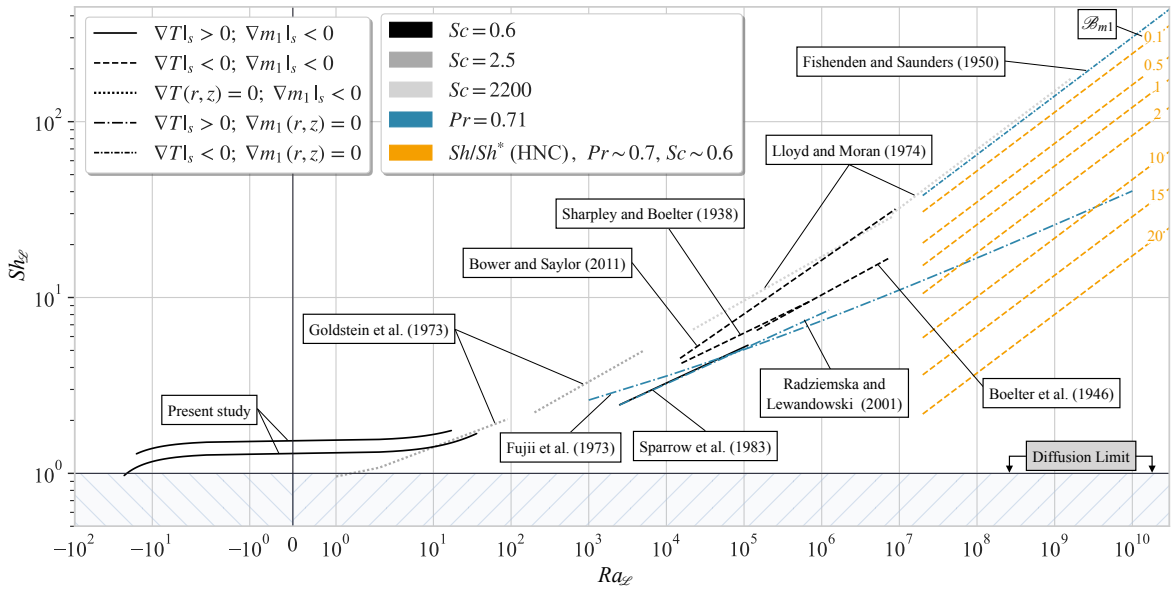

Figure 4.3: Graphical representation of previous $Sh_{\mathscr{L}} - Ra_{\mathscr{L}}$ correlations and their applicable ranges. We present correlations from the present study in context with those from previous studies. This figure is a visual supplement to Table 4.1. The abscissa and ordinate denote values for $Ra_{\mathscr{L}}$ and $Sh_{\mathscr{L}}$, respectively. The length of each curve denotes the valid range of the associated correlation. Shades of gray denote the value of the Schmidt number of the fluid used in each study with black indicating $Sc = 0.6$ for moist air, dark-gray for $Sc = 2.5$ for naphthalene sublimation, and light-gray denoting $Sc = 2200$ for electrochemical studies. We use the color blue to denote pure heat transfer correlations for upward-facing heated/cooled plates that we converted using the Chilton-Colburn analogy between heat and mass transfer. The color orange denotes corrections to the correlation from Fishenden and Saunders [91] for high mass transfer rate theory (Sh/Sh^*) based on the Horizontal Natural Convection (HNC) correction proposed by Brewster [106], with values of $\mathscr{B}_{m1}$ up to 20, which coincides with incipient boiling. Finally, the type of line indicates the sign of the temperature or concentration gradients at the interface. Solid lines for positive temperature gradients, dashed lines for negative temperature gradients, dash-dotted for isothermal systems, and dotted in the absence of concentration gradients. The sign of the thermal/concentration gradients assume the z coordinate is away from the s-surface. See B for a tabulation of the correlations' original coefficients, length scales, and ranges.

4.2 Data and Methods

Integer subscripts denote species; hereafter, a subscript 1 refers to H_2O, a subscript 2 refers to a standard dry air mixture, and the absence of a subscript denotes a binary mixture of water vapor and dry air. Furthermore, the composition of dry air throughout the lower-troposphere is assumed constant and equal to the U.S. Standard Atmosphere at sea level [109]. Accordingly, the molecular weight of dry air, denoted M_2 [kg/kmol], is approximated as

$$M_2 = \sum x_i M_i \approx 28.96 \text{ kg/kmol} \tag{4.6}$$

where i denotes each species in the U.S. Standard Atmosphere and x_i denotes the dimensionless mole fraction of each species.

Moreover, given the mean free path values for air under the experimental conditions covered, and the low water vapor concentrations characteristic of low mass transfer rates, the ideal gas law is applicable. Consequently, each species satisfies the well known relations

$$P_i \approx \rho_i \frac{\mathscr{R}}{M_i} T = \rho_i R_i T \tag{4.7}$$

where P_i [Pa] is the partial pressure of species i, ρ_i [kg/m^3] is the specific mass of species i, $\mathscr{R}$ is the universal gas constant (8,314.46 [J/kmol K]), M_i [kg/kmol] is the molecular weight of species i, R_i [J/kg K] is the specific gas constant for species i, and T [K] is the mixture temperature. For convenience, R_1 and R_2 are given below

$$R_1 \approx 461.5 \text{ J/kg K}; \quad R_2 \approx 287.1 \text{ J/kg K} \tag{4.8}$$

4.2.1 Dimensionless numbers

A note regarding length scales

Before discussing convection correlations, a brief exchange regarding the nomenclature of dimensionless parameters employed in these correlations is necessary. Expressly, it is our opinion that dimensionless parameters whose definitions include a length scale, particularly the Sherwood (or Nusselt) number, the Rayleigh number, and the Grashof number, should always appear with their length scale explicitly, as is Sh_L where L is some relevant length scale.

While the inclusion of the length scale in representations of dimensionless parameters is beneficial for several reasons, a single fundamental motivation drives the choice to include it here; this approach explicitly indicates when scaling is required to facilitate a meaningful comparison of results that employ disparate length scales. For this reason, in this work, expressions of dimensionless parameters defined with a length scale invariably include their length scale with a single exception; when signifying the general functional form of correlations (that are independent of the length scale), we omit the scale, at which point we assume the scale is consistent across the association. For example, when discussing general $Sh - Ra$ correlations of the form $Sh(Ra)$, which would encompass all consonant length scales.

Now that we are clear regarding the nomenclature of dimensionless parameters, we are free to discuss our choice of correlating parameter(s) when presenting results. As mentioned before, some discrepancies exist in the literature regarding this choice, particularly when comparing earlier studies [93, 5, 94, 96, 99, 100] with more recent ones [101, 102]. To provide context surrounding the form of the correlations presented here, what follows is a discussion of the motivation for choosing the correlating parameter used in this work. The ensuing deliberation includes a justification for our choice of the characteristic length scale and a derivation of the correlating parameter.

Choice of characteristic length scale

The previous discussion regarding the significance of the explicit expression of characteristic length scales associated with dimensionless parameters implies several length scales in the literature. Some authors prefer conspicuous scales such as the radius [100] or diameter [93, 5] when the planform is circular, or the length of a side when the planform is square [101, 102]; each of which applies to a specific geometry with unity aspect ratio. In contrast, others favor more general scales suitable to a broader range of geometries with generally non-unity aspect ratios, such as the surface area to perimeter ratio [96, 99]. Fundamentally, there is no conflict with the choice of a given length scale because simple scaling enables the conversion from any given length scale to any other length scale. However, the use of more than one length scale coupled with a non-explicit expression of each length scale may result in an unintentional comparison of correlations containing varying length scales [101, 102].

In an attempt to circumvent such an incompatible comparison and facilitate uniformity, we define the characteristic length as the ratio of the surface area of the interface to the perimeter that encompasses this area, hereafter defined as

$$\mathscr{L} \equiv \frac{A}{P}, \tag{4.9}$$

where readers familiar with fluid mechanics will recognize this ratio as the equivalent (or hydraulic) radius and, except for a factor of 4, as the equivalent (or hydraulic) diameter. This choice for the characteristic length scale is entirely intentional and driven by three primary factors, subsequently addressed.

First, as mentioned above, this ratio is suitable for a vast number of planforms with potentially non-unity aspect ratios, which will be particularly relevant when comparing results from previous studies, see Table 4.1. Second, physical observations exist that support the relevance of $\mathscr{L}$ in buoyant flows. Categorically, as explained by Goldstein et al. [96] and supported by flow

visualization photographs by Husar and Sparrow [94], the length $\mathscr{L}$ closely approximates the average horizontal distance traveled by air fluid particles moving from the edges of the interface into the interior (for flows directed away from the interface) or from the interior to the edges (for flows directed toward the interface), see Fig 4.1. Finally, the use of $\mathscr{L}$ advances the intersection of unity Rayleigh and Sherwood numbers for pure diffusion, suggesting that the employment of $\mathscr{L}$ provides a parsimonious representation of the physical phenomena, see Fig 4.3.

Choice of correlating parameter

Traditionally, natural convection correlations appear in the form $Sh(Ra)$; this occurs in both archival textbooks [91, 110, 92, 95] and literature [93, 5, 97, 98, 96, 99, 100]. However, more recent studies [101, 102] express correlations in the form $Sh(Ra,Sc)$. The authors of more recent studies include a pre-factor of $Sc^{1/3}$ claiming that such a composition allows for comparison across studies employing various fluids and, as a result, different Schmidt numbers. Here we opt for not including such pre-factor for several reasons.

First, inclusion of a pre-factor is hardly needed to compare results from various working fluids; the Rayleigh number allows for direct comparisons. The Rayleigh number facilitates an immediate comparison because, as pointed out by Goldstein et al. [96], the choice of the Rayleigh number rather than the Grashof number as the correlating parameter minimizes the separate dependence of the Sherwood (or Nusselt) number on the Schmidt (or Prandtl) number. This weaker dependence occurs because the Rayleigh number is already the product of the Grashof and Schmidt (or Prandtl) numbers. Therefore, the correlations in [101, 102] of the form $Sh(Ra,Sc)$ are also, more generally, of the form $Sh(Gr,Sc) = BSc^{n+1/3}Gr^n$, where Sc is constant, implying $Sh(Gr)$.

As a result, the use of Sc-dependent pre-factor is somewhat unnecessary except for perhaps two cases: (1) when the Schmidt number is not approximately constant or (2) when calculating correlations where the Schmidt (or Prandtl) dependence is independent of the Grashhof number

dependence; e.g., for flows where compressibility is important. Considering neither of the former cases apply to this study or any previous studies discussed here, we drop the $Sc^{1/3}$ pre-factor and express the correlation in the form $Sh(Ra)$ for the remainder of this work, re-scaling previous results where necessary. What follows is a brief discussion on the dimensionless parameters we employ in this study.

4.2.2 Definition of the correlating parameter

Vapor mixture conservation equations

Relevant equations for the vapor mixture include conservation of mass, of force-momentum, of energy, and of a diffusing molecular species:

$$\frac{\partial \rho}{\partial t} = -\nabla \cdot (\rho \mathbf{v}), \tag{4.10}$$

$$\rho \frac{D\mathbf{v}}{Dt} = \rho \mathbf{g} - \nabla P + \mu \nabla^2 \mathbf{v} + \frac{1}{3}\mu \nabla(\nabla \cdot \mathbf{v}), \tag{4.11}$$

$$\rho c_p \frac{DT}{Dt} = k\nabla^2 T + \beta T \frac{DP}{Dt} + \mu\Phi + q''', \tag{4.12}$$

$$\frac{D\rho_i}{Dt} = \mathscr{D}_{12}\nabla^2 \rho_i, \tag{4.13}$$

where $\mathbf{v}$ [m/s] is the velocity vector, ρ [kg/m^3] is the specific mass of the mixture, t [s] is time, $\mathbf{g}$ [m/s^2] is the gravity vector, P [Pa] is the pressure, μ [kg/m s] is the dynamic viscosity, c_p [J/kg K] is the specific heat capacity at constant pressure, k [W/m K] is the thermal conductivity, T [K] is temperature, β [1/K] is the thermal coefficient of volume expansion, $\mathscr{D}_{12}$ [m^2/s] is the binary diffusion coefficient, Φ [J/kg m^2] is the viscous dissipation term, and q''' [W/m^3] is the heat generation rate per unit volume. These equations assume μ, k, and $\mathscr{D}_{12}$ to be constant over the range of temperatures and relative humidities under consideration, and they also neglect Sorét (thermo-diffusion), Dufour (diffusion-thermo) and inter-diffusion effects.

Further approximations to the force-momentum balance include the Boussinesq approximation for small density variations [111]. Specifically, because water evaporation in air at lower-tropospheric conditions cannot drive mass transfer rates, we assume that density differences are relevant only in causing a buoyancy force. Therefore, both the time rate of change of density ($\partial\rho/\partial t$) in Eq. (4.10) and the divergence of the velocity field ($\nabla\cdot\mathbf{v}$) in Eqs. (4.10) and (4.11) are assumed to be zero [112, 113]. As a result, the sum of the body force due to gravity and the gradient of static pressure (net body force) $\rho\mathbf{g}-\nabla P$ simplify to the sum of the local buoyant force and the gradient of motion pressure $\mathbf{B}+\nabla P_m$, where $\mathbf{B}=\mathbf{g}(\rho-\rho_e)$ and $P_m=P-P_h$ where P_h is the hydrostatic pressure. We assume that the static pressure P is equal to the hydrostatic pressure P_h so that the motion pressure P_m is zero and, consequently, $\nabla P_m=0$. The previous approximation results in the net body force reducing to the buoyant force $\mathbf{B}$. Subsequent independent determination of density effects arising from thermal and chemical species concentrations then appear in the form

$$(\rho_e-\rho)=\rho\left[\beta(T-T_e)+\gamma_i(\rho_i-\rho_{i,e})\right], \tag{4.14}$$

where we have adopted the Einstein summation convention and, for an ideal gas, β and γ_i are

$$\beta=-\frac{1}{\rho}\frac{\partial\rho}{\partial T}\bigg|_{P,\rho}=\frac{1}{T}, \tag{4.15}$$

and

$$\gamma_i=-\frac{1}{\rho}\frac{\partial\rho}{\partial\rho_i}\bigg|_{P,T}=\frac{1}{\rho}\left(\frac{M}{M_i}-1\right), \tag{4.16}$$

respectively.

It is worth noting that, for a dilute species-1, $M\approx M_2$ so that we may approximate γ_i as

$$\gamma_i\approx\frac{1}{\rho}\left(\frac{M_2}{M_i}-1\right).$$

It is clear from the expression above that γ_2 is approximately zero, and therefore negligible.

Conversely, γ_1 is not negligible and can be approximated by

$$\gamma_1 \approx \frac{1}{\rho}\left(\frac{M_2}{M_1} - 1\right) \approx 0.505 \ \frac{\mathrm{m}^3}{\mathrm{kg}}, \tag{4.17}$$

where we have assumed ρ_2 is equal to the IUPAC standard at 1 atm and 293.15 K. While this approximation is particularly useful for hand calculations, our automated calculations allow for more precise incorporation of property values. For this reason, we calculate γ_1 using Eq. (4.16) for the remainder of this study.

We make three additional simplifications to the energy equation. First, the pressure term $\beta T(DP/Dt)$ is neglected due to the flow's limited vertical extent. Secondly, we neglect viscous dissipation. Finally, we neglect internal heat generation in the system. Therefore, for a steady, laminar, one-dimensional flow with no viscous dissipation, limited vertical extent, and no internal heat generation, the conservation equations simplify to:

$$\frac{dw}{dz} = 0, \tag{4.18}$$

$$w\frac{dw}{dz} = g\left[\beta(T - T_e) + \gamma_i(\rho_i - \rho_{i,e})\right] + \nu\frac{d^2w}{dz^2}, \tag{4.19}$$

$$w\frac{dT}{dz} = \alpha\frac{d^2T}{dz^2}, \tag{4.20}$$

$$w\frac{d\rho_i}{dz} = \mathscr{D}_{12}\frac{d^2\rho_i}{dz^2}. \tag{4.21}$$

Non-dimensionalization proceeds with the following definitions:

$$\zeta = \frac{z}{\mathscr{L}}; \quad \omega = \frac{w\mathscr{L}}{\nu},$$

$$\theta = \frac{T - T_e}{T_s - T_e}; \quad \phi_i = \frac{\rho_i - \rho_{i,e}}{\rho_{i,s} - \rho_{i,e}},$$

yielding

$$\frac{d\omega}{d\zeta} = 0, \tag{4.22}$$

$$\frac{d^2\omega}{d\zeta^2} + Ra_{\mathscr{L}} = Pe_{\phi}\frac{d\omega}{d\zeta}, \tag{4.23}$$

$$\frac{d^2\theta}{d\zeta^2} = Pe_{\theta}\frac{d\theta}{d\zeta}, \tag{4.24}$$

$$\frac{d^2\phi_i}{d\zeta^2} = Pe_{\phi}\frac{d\phi_i}{d\zeta}, \tag{4.25}$$

where the thermal and chemical Péclet numbers are

$$Pe_{\theta} \equiv \frac{\dot{m}''\mathscr{L}}{\rho\alpha},$$

and

$$Pe_{\phi} \equiv \frac{\dot{m}''\mathscr{L}}{\rho\mathscr{D}_{12}}.$$

respectively, and the Rayleigh number is defined the product of the Grashof and Schmidt numbers

$$Ra_{\mathscr{L}} \equiv Gr_{\mathscr{L}}Sc, \tag{4.26}$$

which are both defined below for completeness

$$Gr_{\mathscr{L}} \equiv \frac{g\mathscr{L}^3}{\nu^2}\left[\beta(T_s - T_e) + \gamma_i(\rho_{i,s} - \rho_{i,e})\right],$$

and

$$Sc \equiv \frac{\nu}{\mathscr{D}_{12}}.$$

With those two definition, we arrive at

$$Ra_{\mathscr{L}} = \frac{g\mathscr{L}^3}{\nu\mathscr{D}_{12}}\left[\beta(T_s - T_e) + \gamma_i(\rho_{i,s} - \rho_{i,e})\right]. \tag{4.27}$$

Before moving on, we find it beneficial to address a few points. First of all, our binary species assumption results in $\mathscr{D}_{12} = \mathscr{D}_{21}$ so that a single chemical Péclet number is present. Furthermore, an often-overlooked characteristic of the definition of *Ra* in previous studies is the insight provided by the partitioning of buoyant forces. Specifically, as previously noted by Pera and Gebhart [108], the ratio of $\gamma_i(\rho_{i,e} - \rho_{i,s})$ to $\beta(T_s - T_e)$ is useful in quantifying the relative importance of each of these components in causing density differences that drive the flow,

$$N \equiv \frac{\gamma_i(\rho_{i,s} - \rho_{i,e})}{\beta(T_s - T_e)}. \tag{4.28}$$

The value of the *N* ratio will be useful later when discussing the experimental results. Furthermore, we find it particularly relevant to add a note about the Rayleigh number sign here. Specifically, we assign negative values to Rayleigh numbers when the density of the mixture is greater at the air-water interface than far away, and the flow is directed downwards (towards) the interface, rather than away from it. The negative *Ra* number for this contra-flow regime becomes clear when one considers the balance of the terms in Eqn. 4.14, which holds for all experiments in this study,

$$\frac{\rho_s - \rho_e}{\rho} = -\left[\beta(T_s - T_e) + \rho\gamma_1(m_{1,s} - m_{1,e})\right].$$

4.2.3 Experimental apparatus

Measurement of evaporation rates at various vapor concentrations requires precise control and observation of the ambient temperature, pressure, and concentrations within the control volume where the evaporation is occurring. To this end, we designed a cylindrical stainless steel chamber (hereafter referred to as *chamber*) that has the correct dimensions for the pool

evaporation study. The chamber has an internal radius of $\sim$0.3 m, an internal length of $\sim$0.7 m, and the cylindrical axis is placed horizontally. The chamber also features Kurt Lesker's proprietary Hydra-Cool^{TM} cooling traces for temperature control, see §4.2.3. The chamber also has several ports outfitted with ConFlat$^{®}$ (CF) flanges for the integration of various sensors, actuators, and pumping systems, see Fig. 4.4. The authors choose CF flanges for their superior temperature and pressure ranges of (77, 723) K and (1.3×10^{-11}, 1.01×10^{5}) Pa, respectively. The following sections describe the cooling system, sensors, actuators, and pumping systems used to control and monitor the experimental control volume.

Temperature control and measurement

To control the temperature of the chamber, we circulate a working fluid through a closed loop that includes the chamber and a cooling/heating recirculating chiller. In order to maximize surface coverage and minimize temperature distributions inside the chamber, the chamber features four independent Hydra-Cool^{TM} traces, one on the front and back of the chamber and one on each side of the chamber, see Fig. 4.4. These four traces were welded to the chamber and subsequently injected with a high-pressure fluid to hydro-form the channels. Two nylon manifolds connect the chamber's four traces to the inlet and outlet of a cooling/heating recirculating chiller (Thermo Scientific Accel 500 LT), hereafter referred to as the chiller, via chemical resistant Tygon tubing. The chiller circulates a 50% v/v mixture of deionized water and ethylene glycol ($C_2H_6O_2$) to prevent the working fluid from freezing when operating near/below the freezing point of water. The circulation of the working fluid through the chiller holds the chamber and internal vapor mixture at a constant temperature during experiments. A total of eleven type K thermocouples measure the temperature of the inner walls of the chamber and the internal vapor mixture, each with an uncertainty of $\pm$0.2 K. Specifically, eight thermocouples measure the temperature of the inner walls of the chamber, and three thermocouples measure the temperature of the vapor mixture approximately 8 cm from the inner wall of the chamber.

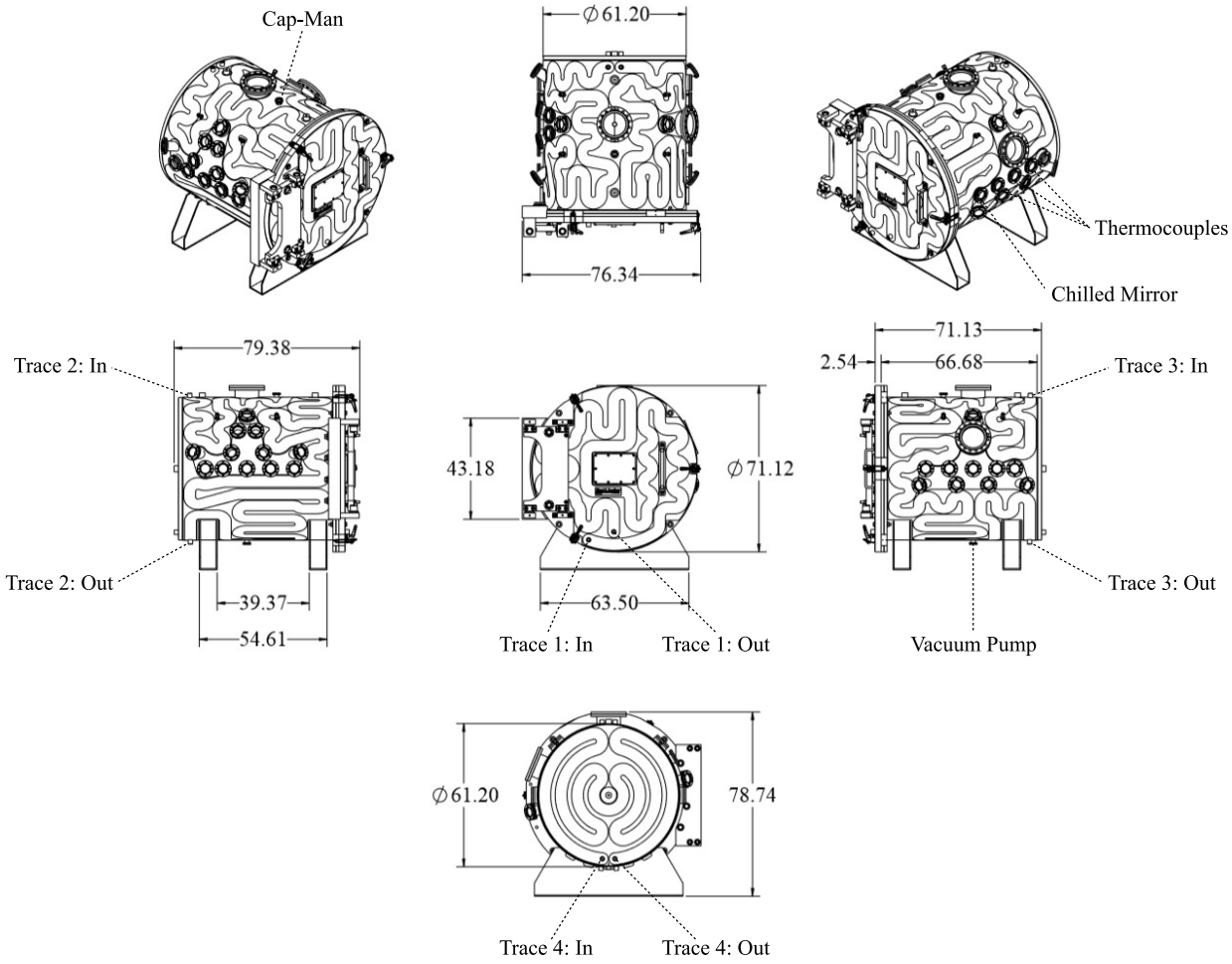

Figure 4.4: Detailed drawing of the chamber used in this study. All units are in cm, and the ø symbol denotes a diameter. This figure also indicates the ports for connecting the capacitance manometer, the eleven thermocouples, the chilled mirror hygrometer, the vacuum pump, and the four Hydra-Cool^{TM} cooling traces.

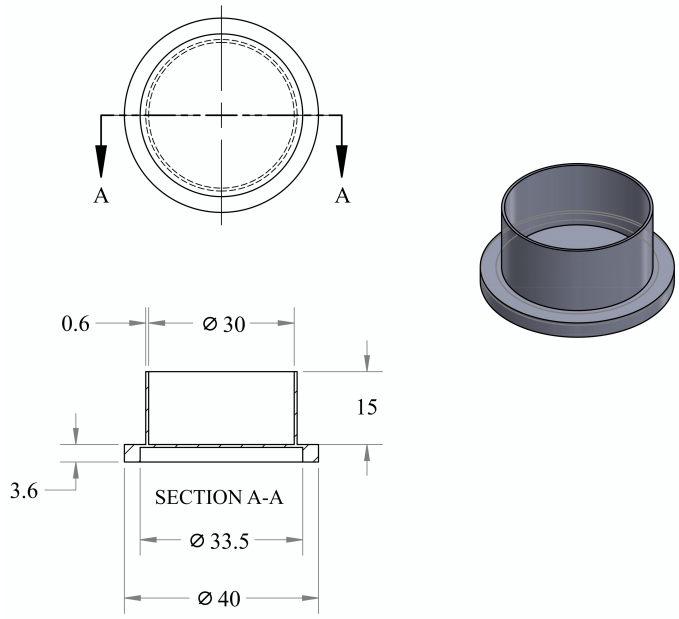

Figure 4.5: Detailed drawing of the POM pool tube used in this study. All units are in mm, and the ø symbol denotes a diameter. The pool has an inside diameter of 30 mm, a wall thickness of 0.6 mm, and a depth of 15 mm. During experiments, water completely filled the pool to a height of 15 mm, corresponding to a water volume and water mass of approximately 10.6 cm^3 and 10.6 g, respectively. In addition, the empty and dry POM pool and mass of 3.4 g. Consequently, when the pool is completely filled with liquid water the total mass of the pool and water is approximately 14 g.

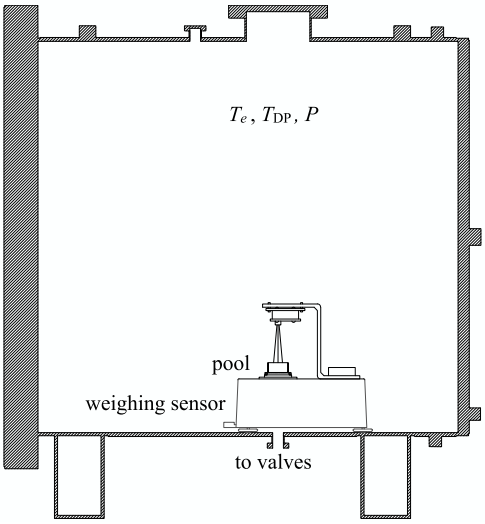

Figure 4.6: Cross-sectional view of the experimental chamber designed and built for this study. We placed the weighing sensor near the center of the chamber floor directly over the flange to the pumping section. The circular pool rests on the pan of the weighing sensor, which measures the change in mass as liquid water evaporates. Furthermore, a non-contact infrared temperature sensor above the pool measures the surface temperature of the liquid. A collection of thermocouples distributed throughout the chamber measure the ambient temperature while a chilled mirror hygrometer observes the dew point. Finally, a heated capacitance manometer mounted to the top of the chamber provides pressure readings.

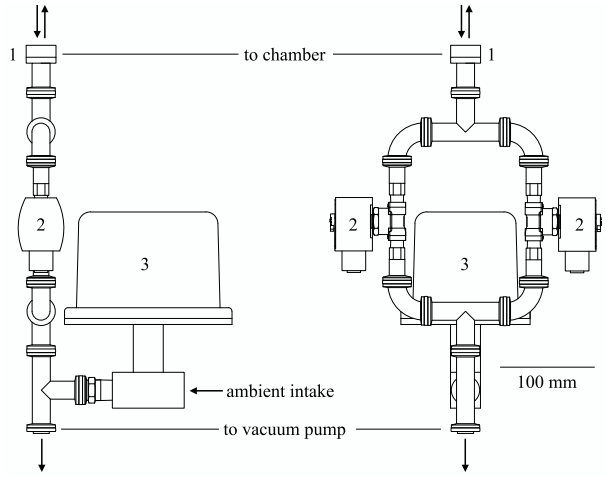

Figure 4.7: Details of the pressure control system used to modify chamber evacuation rates. 1) Isolation section: CF coupled butterfly valve isolates the control volume from potential downstream leaks. 2) Conductance section: Two NPT threaded solenoid valves with flow coefficients of 0.76 m^3/h and 0.18 m^3/h. 3) Bypass section: Single NPT threaded proportioning valve used to throttle the vacuum pump and repressurize the chamber.

Pressure control and measurement

While all experiments described here occurred at approximately atmospheric (laboratory) pressure, the chamber has been outfitted with an evacuation and isolation system designed to facilitate future experiments at reduced pressures. To this end, a heated capacitance manometer (CMX1, Brooks Instrument) mounted vertically on top of the chamber (see Fig. 4.4) continuously monitors pressure in the chamber with an accuracy of $\pm 0.015\%$. This capacitance manometer is heated to 310 K at all times to avoid condensation on the capacitor, which would result in errors. A constant output vacuum pump (E2M28, Edwards) is connected to the chamber through a series of three main valve sections referred to here as isolation, conductance, and bypass; see Fig 4.7. The isolation section consists of a manually operated low-pressure butterfly valve (P104246, Ideal Vacuum) directly coupled to the chamber via CF flanges. This low-pressure valve isolates the control volume from gas that may leak from any downstream fittings during experiments. Next, the conductance layer consists of two parallel solenoid values with different flow coefficients (8262H182 and 8262H230, ASCO Valve Inc). The larger solenoid valve has a flow coefficient

of 0.76 m^3/h, while the smaller solenoid valve has a flow coefficient of 0.18 m^3/h resulting in a combined (parallel) flow coefficient of 0.94 m^3/h. The controller opens and closes these solenoid valves to increase or decrease the overall conductance of the valve configuration in order to manipulate the chamber's evacuation rate. Finally, a computer-controlled proportioning valve (PV516-B, Omega Engineering) serves two purposes, depending on whether the vacuum pump is operating or not. When the vacuum pump is on, this valve throttles the evacuation rate from the chamber by allowing ambient air to enter the pump. When the vacuum pump is off, this valve enables pressure equalization by allowing ambient air to reenter the chamber through the conductance and isolation sections.

Concentration control and measurement

Control of water vapor concentration in the chamber requires both a source and a sink of water vapor. As described in the introduction, §4.1, evaporation from a liquid interface serves as a source of water vapor in the chamber while a desiccant bed serves as a sink. Experimental runs last for several hours, and unforced evaporation of liquid water from a cylindrical reservoir slowly increases the ambient concentration; see §4.2.4 for experimental details. The desiccant bed mass exchanger consists of a 240 mm long section of 25.4 mm inside diameter cylindrical pipe filled with spherical 4x8 mesh 3Å molecular sieves. A compressor (AL-6 B, Alita) with a static pressure head of 20 kPa and rated flow rate of $0.1\bar{3}$ L/s, forces the vapor mixture through the mass exchanger, and the 3Å pores trap polar water vapor molecules but allow other non-polar species to pass through. The mass exchanger can reduce relative humidity values below 1% over all temperatures and pressures considered in this work.

A chilled mirror hygrometer (Optidew Remote, Michell) measures the dew point inside the chamber with an uncertainty of ± 0.2 K. The ambient vapor mixture is allowed to diffuse over the sensor during experiments. The hygrometer is located directly inside a port below the opening of the tube and near the chamber wall, see Fig. 4.4. This placement avoids any plumes they may

develop above the tube and interfere with the observation of ambient conditions.

Cylindrical pool

Experiments used a cylindrical pool machined from a rod of PolyOxyMethylene (POM) (commercially known as Delrin). POM is an engineering thermoplastic used here for its low moisture absorption ($<1\%$ at saturation, 296 K) and thermal conductivity (0.37 W/m K). The pool has an inside diameter of 30 mm, a wall thickness of 0.6 mm, and a depth of 15 mm, with a total mass of approximately 3.4 g; see Fig. 4.5 for a detailed drawing of the pool. During experiments, water completely filled the pool, corresponding to a liquid H_2O volume of approximately 10.6 cm^3 and a total mass of approximately 14 g. Furthermore, with respect to the length scale of the reservoir, McBain, Suehrcke, and Harris [114] showed that when the ratio of enclosure length scale to tube radius is greater than 30, the shape of the enclosure has a negligible effect on the transfer rates. In the present study, the ratio of chamber height to tube radius is approximately 40. Therefore, we assume that the chamber geometry is negligible, and results are valid for any extensive quiescent ambient medium.

A downward-facing infrared temperature sensor with a 10° field of view was placed 82.5 mm above the pool so that the active measurement area served as nearly 95% percent of the water's surface. This IR sensor was calibrated using a well-mixed water bath with a heating/cooling element coupled with a calibrated type K thermocouple for reference. Calibration considered the uncorrelated errors in the bi-variate data during linear regression. Specifically, the regression equations are generalized version of the York equations [115] and we used a MATLAB ^{TM}implementation available in [116].

Mass observation

A weighing sensor (4212B-102, A&D) is used to measure the mass of the pool and liquid water inside the pool during experiments. The weighing sensor is placed on the interior floor

of the chamber with its pan located near the center of the chamber, see Fig 4.6. The 3 mm disk-shaped indent on the bottom of the pool centers the pool on the weighing sensor's plate, see Fig. 4.5. The weighing sensor has a resolution, standard deviation, and linearity of 1×10^{-8} kg, 4×10^{-8} kg, and $\pm1\times10^{-7}$ kg respectively. Because experiments are designed to measure mass flux rather than the magnitude of the body force on the liquid, error propagation assumes a standard deviation of 1×10^{-7} kg for the remainder of this work. In comparison to the standard deviation of the balance $O(10^{-8}$ kg), an increase of 1% RH for a mixture at 300 K, 100 atm, and 50% RH corresponds to an increase in the specific mass of $O(10^{-4}$ kg/m$^3)$. The volume of the chamber is $O(1$ m$^3)$, and it is now clear that the weighing sensor's resolution is several orders of magnitude lower than what would be required to estimate mass flux from measurements of the body force in time.

4.2.4 Procedure

Data acquisition system

The present study employs a custom Data Acquisition System (DAS) to log all raw signals and convert them to observations in their respective units. The custom DAS consists of a Windows PC running LabVIEW with a local network connection to a National Instrument cRIO-9074. The cRIO couples with two hot-swappable I/O units (NI-9205 and NI-9213) and a custom signal conditioning Printed Circuit Board (PCB) designed by the authors. The 9205 allows for the measurement of analog signals, while the 9213 facilitates thermocouples with a cold junction compensation. During each experiment, the chamber's temperature was held constant at 285, 290, 295, 300, 305, and 310 K, while the DAS logged observations at one-second intervals. Each observation consisted of several variables whose names, units, and uncertainties we have outlined in Table 4.2. To minimize sidewall effects, we conducted numerous experiments where the total mass loss during any given experiment was less than two grams. As a result,

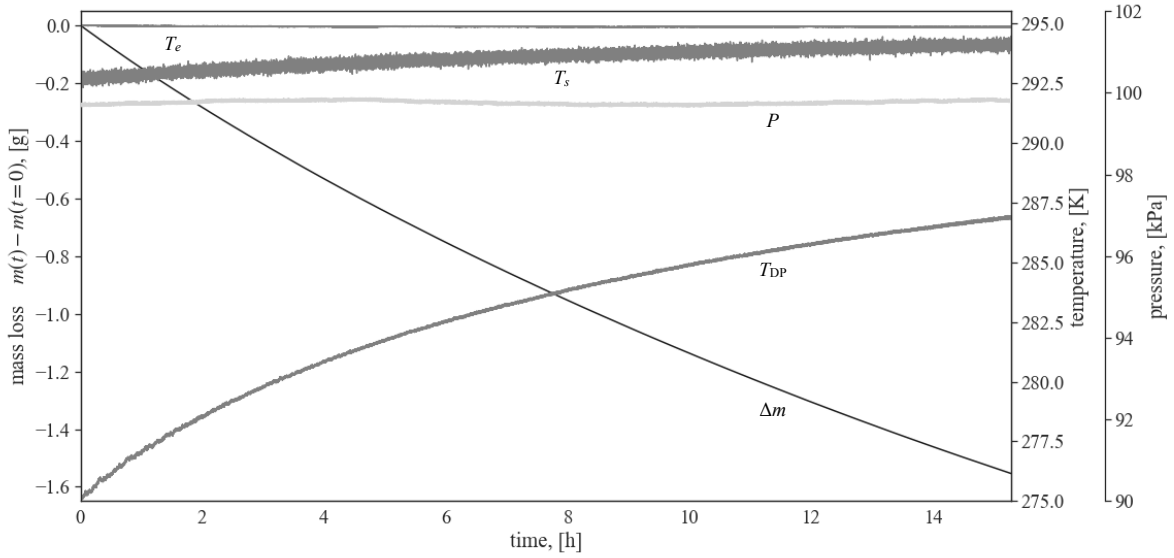

Figure 4.8: Sample of data from a single experiment conducted at a mixture temperature of 295 K, 99.75 kPA, and dew point temperatures ranging from 275 to 287 K. The surface temperature of the liquid ranged from 292.5 K to 294.5 K. This experiment lasted approximately 15 hours. At the end of the experiment, the mass loss was approximately 1.5 grams, which is typical for all of our experiments. We extracted approximately 600 independent mass transfer measurements using the mass flux measurement algorithm, see §4.2.4. *Note: the variable is listed directly under each curve.*

the pool remained full for the duration of data collection. Liquid surface temperatures typically varied by a few degrees K while the dew point varied by 10 to 15 K. Pressure was held constant during experiments. Data for the mass loss in time, the temperature of the liquid's interface, the temperature of the air, the dew point temperature, and the chamber's pressure as a function of time are shown in Fig. 1.4. The evaporation of vapor from the pool increases the dew point temperature in the chamber and, thus, the thermal and concentration driving potentials.

What follows is an outline of the hardware and its integration with the custom DAS. The pressure, P, and dew point, T_{DP}, were measured using the capacitance manometer and chilled mirror hygrometer. We connected both the capacitance manometer and chilled mirror hygrometer to the NI-9205 via the signal conditioning board. The mass, m, was measured using the weighing sensor connected to a PC's serial port. The environmental temperature T_e was measured using

Table 4.2: Raw observation variables. These raw data streams are converted to results via the novel algorithm.

	name	symbol	units	uncertainty	notes
1.	`cap_man_ok`	-	Boolean	-	True when the capacitance manometer is functioning properly.
2.	`dew_point`	T_{DP}	K	± 0.2	Measured with a dew point mirror.
3.	`idx`	t	s	-	Assumed to have zero uncertainty.
4.	`mass`	m	kg	$\pm 1 \times 10^{-7}$	Change in time used to measure mass flux.
5.	`optidew_ok`	-	Boolean	-	True when dew point hygrometer is functioning properly.
6.	`pressure`	P	Pa	$\pm 0.15\%$	Measured with capacitance manometer.
7.	`surface_temp`	T_s	K	± 0.5	Measured with IR-sensor.
8.	`temperature`	T_e	K	± 0.2	Measured with thermocouples.

eleven type-K thermocouples; eight distributed across the chamber wall's interior and three extending approximately 8 cm from the chamber wall connected to the NI-9213. The water's surface temperature, T_s, was measured using a non-contact infra-red sensor temperature sensor connected to a USB port of the central PC and logged in LabVIEW. After the DAS has recorded these raw data streams have, the authors employ a custom gravimetric algorithm to calculate the mass flux (and relevant dimensionless parameters).

Mass flux measurement

We assume that, locally, the variation of mass with time is approximately linear. Thus, we user linear regression to fit our model to

$$m(t) = m(t|a,b) = a + bt. \tag{4.29}$$

The uncertainty associated with each of the mass observations was experimentally determined to be $\sigma_i = 1 \times 10^{-7}$ kg and we assume the times t_i's are known exactly. The chi-square merit function is then written

$$\chi^2(a,b) = \sum_{i=i_0}^{i_0+N} \left(\frac{m_i - a - bt_i}{\sigma_{m,i}} \right)^2 \tag{4.30}$$

which gives the maximum likelihood parameter estimations of a and b assuming that the errors are normally distributed. We use hypothesis testing to establish a goodness-of-fit. The null hypothesis

is that a χ^2 value at least as small as the obtained value could have occurred by chance with a 0.01 significance level (one tailed test). In other words the χ^2 cumulative distribution function for $N-2$ degrees of freedom should be less than or equal to 0.01 for the given χ^2 value in order to reject the null-hypothesis

$$p = P(\chi^2 \leq \chi_0^2) = \Phi_\nu(\chi^2) \leq 0.01 \tag{4.31}$$

where Φ_ν is the cumulative distribution function for a χ^2 distribution with $\nu = N-2$ degrees of freedom. Criteria for a fit is that the $R^2 \geq 0.999$, $p \leq 0.01$ and $\delta_{\dot{m}}5 \leq 0.01$ with a 65% confidence interval.

The authors wrote the algorithm in Python, and linear error propagation was performed using the open-source uncertainties package, [117]. (Once the data has been persisted,) post-processing consists of two-steps: initial data conditioning followed by the application of a novel algorithm for the calculation of mass flux rates. Data conditioning proceeded as follows. First, we estimated the ambient temperature by taking an average of the eleven thermocouples (fixed to and) distributed throughout the interior of the stainless steel chamber. We then applied several Savitzky-Golay filters to smooth the digital data and reduce the signal to noise ratio. Although Savitzky-Golay filters tend to neglect the extremes of oscillations in data, this does not affect data that is varying slowly, but subject to random noise, which is the case here. We found the following filters to give satisfactory agreement with experimental data. We employed a quadratic Savitzky-Golay filter with a five-minute window for the mass. For the pressure, we chose a linear Savitzky-Golay filter with a 60-minute window. Finally, we employed a quadratic Savitzky-Golay filter with a 30-minute window for the dew point.

Next, we employed a novel algorithm for the evaluation of mass flux rates that we designed to minimize the amount of data required for a statistically relevant estimation, which, in turn, maximizes the amount of mass flux data extracted from each experiment. Unlike previous studies that obtain a single data point for each experiment, the method described below generates many data points for each test, locally specific to the conditions, and avoids data reuse in statistical fits.

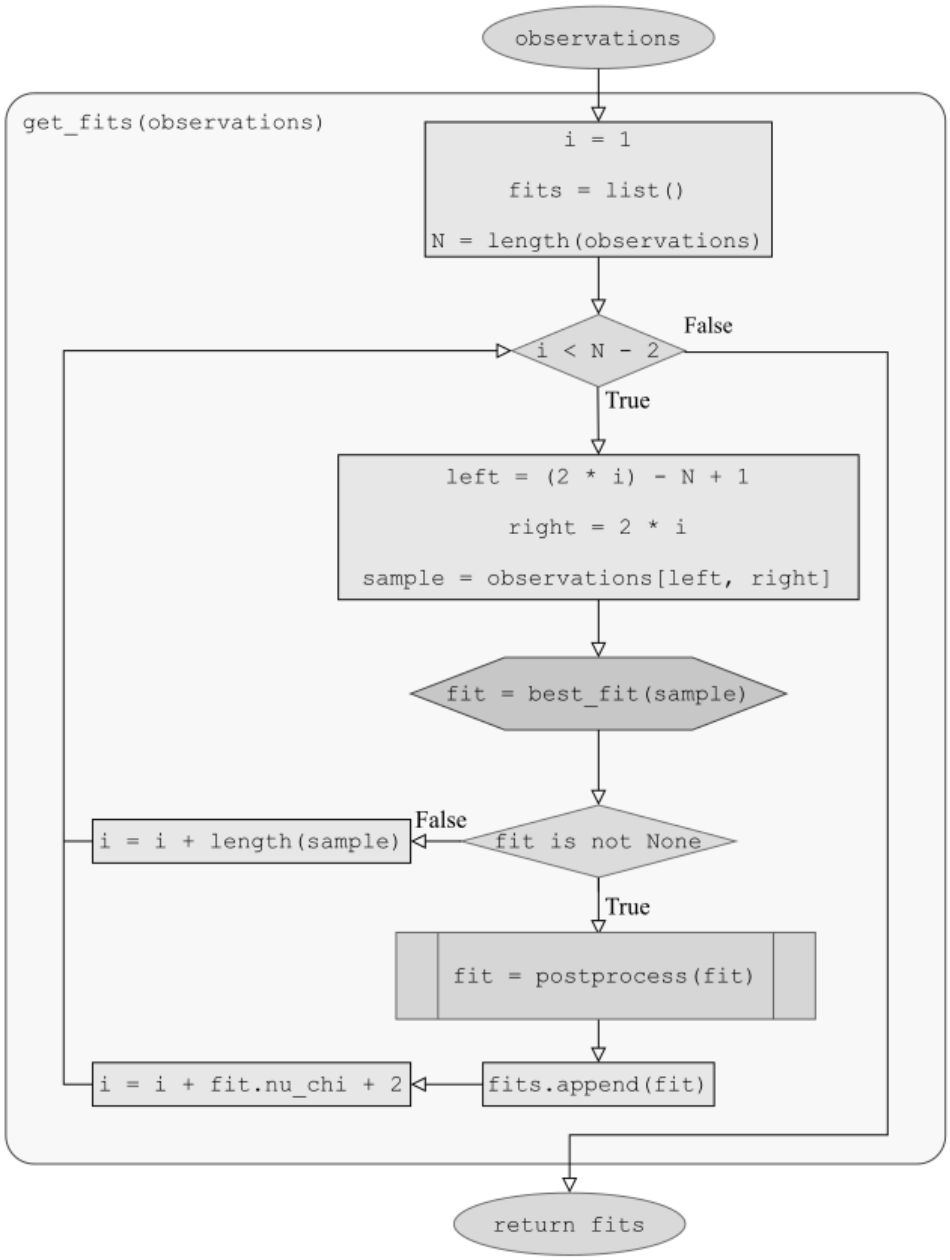

Figure 4.9: Flowchart for the main loop of the gravimetric mass flux algorithm. The algorithm begins with all observations from a given experiment at a constant ambient temperature. The hexagon near the center of the flowchart denotes a sub-process for determining a local best fit, see Fig. 4.10. The algorithm, which begins at the initial observation in time and iteratively steps forward in time, terminates when it has processed all observations associated with a given experiment.

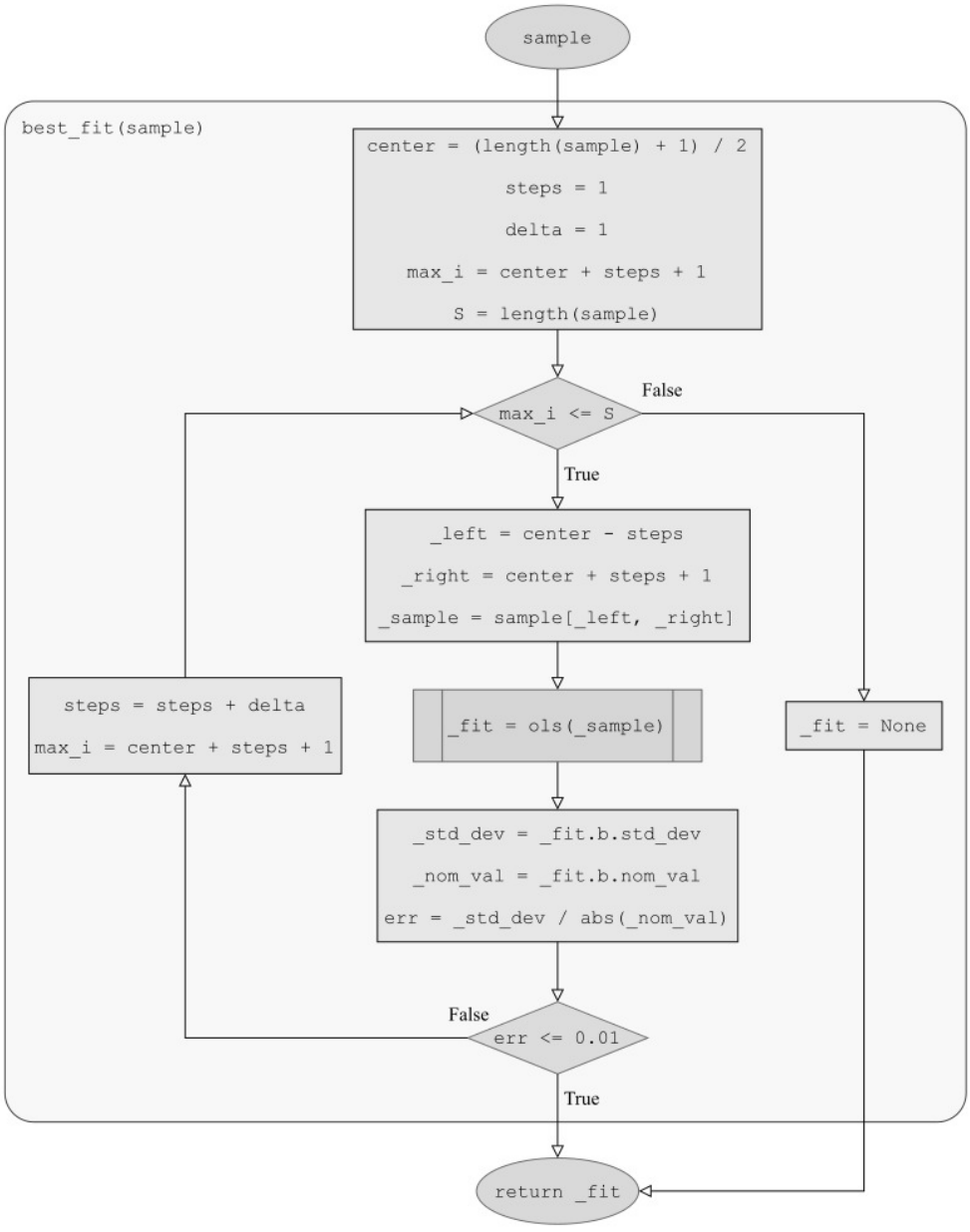

Figure 4.10: Flowchart for the inner loop of the gravimetric mass flux algorithm. The algorithm begins with a sample of observations from the main loop, see Fig. 4.9. The algorithm iteratively increases a centered window until either a satisfactory ordinary least squares fit is obtained, or the window reaches the beginning or end of the experiment. The algorithm persists the degrees of freedom of a potential fit so that the main loop can move to a new center, see Fig. 4.11.

The algorithm, see Fig. 4.9, begins by selecting a potential time for the center of the sample of data. Upon the first iteration, the proposed time is set to one second. This time index will be incremented as long as the time is less than the last valid time minus two seconds. The algorithm then selects a sample determined by the shorter of two: data to the left or data to the right of the selected center. Next, this sample is passed to a sub-process that attempts to perform a linear regression to determine the mass flux.

The local best-fit proceeds as follows: It starts by setting its local steps and delta to one second. While the center + steps < length of the local sample, a proposed sample is created centered at the middle of the sample and has additional data points on either side corresponding to the value of the steps variable. This proposed sample is then fit using ordinary least squares regression, and if the uncertainty in the slope is less than one percent, we persist the fit and proceed. If the slope is zero of no fit is found, which satisfies our statistical criteria, the step variable is incremented by delta, which is one. In this way, delta stays one, but steps increase by one every time. This will include two extra data points every iteration until the entire sample is potentially used.

Finally, once the inner loop returns, if a fit is found, the center time pointer is moved $\nu_\chi + 2$ forward to avoid the reuse of data. If not fit is found, the global index is incremented by the sample's length to ignore this data. In this way, we can see that there are two separate steps in this algorithm. An outer loop that is globally incrementing over the observations to generate samples while the inner loop iterates through each sample from the outer loop and attempts to find a local best fit. This is illustrated in Fig. 4.10

Non-dimensionalization

Once we have the mass transfer rate $\dot{m}$ for all samples in an experiment, we divide the mass transfer rate by the area of the interface to obtain the area-averaged mass flux $\dot{m}''$. This flux

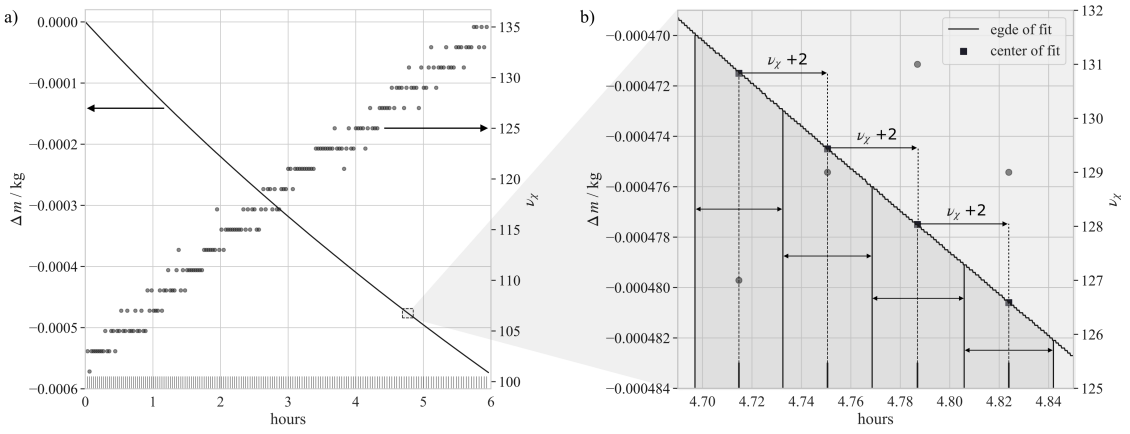

Figure 4.11: Illustration of the gravimetric mass flux algorithm employed in this study. The sub-plot on the left (a) shows the processing of a typical experiment. The horizontal axis denotes time in hours. The left vertical axis indicates the change in mass since the beginning of the experiment, while the right vertical axis registers the degrees of freedom for the sample responsible for a given fit, which is the sample size minus two for linear regression. The solid line corresponds to the change is mass, while the scatter plot corresponds to the degrees of freedom. The rug plot at the bottom indicates the center of each sample corresponding to a satisfactory fit. The sub-plot on the right (b) corresponds to the inset from the sub-plot on the left (a). We provide this sub-plot to illustrate, in detail, the shifting of the proposed center by the previous sample size, i.e., $\nu_\chi + 2$. We chose to increment the proposed center by the sample size to minimize data reuse in statistical fits and, as a result, maximize statistically relevant information from experimental data.

is then combined with relevant observations at the center of the fit to calculate the Sherwood,

$$Sh_{\mathscr{L}} = \frac{\dot{m}'' \mathscr{L}}{\mathscr{B}_{m1} \rho \mathscr{D}_{12}}, \tag{4.32}$$

and Rayleigh (Eq. 4.27) numbers. In the equation above $\mathscr{B}_{m1}$ is defined as

$$\mathscr{B}_{m1} = \frac{m_{1,s} - m_{1,e}}{1 - m_{1,s}}. \tag{4.33}$$

Following a simple dimensional analysis, the Sherwood number must be a function of Reynolds and Schmidt numbers. In general, the dimensionless mass transfer rate is correlated as

$$Sh = Sh_0 + C \left(\frac{UL}{\nu} \right)^m \left(\frac{\nu}{\mathscr{D}_{12}} \right)^n , \tag{4.34}$$

or

$$Sh = Sh_0 + C Re_L^m Sc^n, \tag{4.35}$$

where Sh_0 is the dimensionless mass transfer rate in the pure diffusion limit, U the characteristic velocity and L the characteristic length. For laminar flows, scaling of the transport equations produce values of the exponents n and m equal to 1/3 and 1/2 respectively. The consistency of these two exponent values is very well validated for a variety of flows over flat or spheroidal surfaces [118, 119] when the Sc is of order 1 or higher. Later we will shown that the spatial distribution of water vapor concentration in free evaporation under downward motion has indeed a spheroidal shape.

In free evaporation, the characteristic velocity of the flow depends on the ambient condition into which the process is subjected. In a dry atmosphere, for instance, the velocity of the gas reaches values on the order of 10^{-2} m/s. Since in this problem the characteristic length is on the order of centimeters, the Reynolds number is of order 10, indicating that the inertial forces are only slightly dominant over the viscous forces. Under this circumstance, the buoyancy term in the

conservation of momentum equation scales with the convective term, resulting in a characteristic velocity proportional to the square root of the total Grashof number:

$$O\left(\frac{U^2}{L}\right) \sim O(g\beta_T(T-T_e)+g\beta_m(m-m_{1,e})), \tag{4.36a}$$

or

$$U \sim \frac{\nu}{L} Gr_L^{1/2}. \tag{4.36b}$$

On the other hand, for evaporation occurring at high relative humidity, the velocity of the system tends to zero due to the weaker driving forces. The Reynolds number is now smaller than unity, which consequently leads the buoyant forces to be proportional to the viscous forces, and the characteristic velocity proportional to the total Grashof number:

$$O\left(\nu\frac{U}{L^2}\right) \sim O(g\beta_T(T-T_e)+g\beta_m(m-m_{1,e})), \tag{4.37a}$$

and consequently

$$U \sim \frac{\nu}{L} Gr_L. \tag{4.37b}$$

We then conclude that as long as the buoyancy effect can be neglected, the dimensionless evaporation rate is around the diffusion limit value, with small variations in the Sherwood number initially proportional to the square root of the Grashof number,

$$Sh = Sh_0 + C_{\mathrm{a}}\, Sc^{1/3} Gr^{1/2}, \tag{4.38a}$$

and as the Grashof number further increases, the Sherwood number becomes proportional to the 1/4 power,

$$Sh = C_{\mathrm{b}} + C_{\mathrm{c}}\, Sc^{1/3} Gr^{1/4}. \tag{4.38b}$$

Finally, because the Schmidt number is constant it is absorbed into the Rayleigh number with a 1/2 power as well. As a result, we fit two power laws of the form

$$Sh_{\mathscr{L}}(Ra_{\mathscr{L}}) = C_1 (Ra_{\mathscr{L}} + C_2)^{1/2}. \tag{4.39}$$

where the offset C_2 is required because of the consideration of negative Rayleigh number values. In order to express a single power law with both positive and negative values, a constant is needed in the correlation.

4.3 Results

We begin by discussing the statistical relevance of the curve fits for the different experimental runs. As described above, we perform a linear regression on the mass time series obtained from our weighing sensor at a 1 Hz frequency. We increase the sample size centered at a given point in time iteratively until the standard error in the estimation of the slope ($\partial/\partial t$) is less than or equal to 1%. We subsequently calculate the χ^2 statistic for the given sample and compare it to the degrees of freedom in the given sample ν_χ. We also calculate the coefficient of determination R^2 for each of the proposed fits. Distributions of χ^2, ν_χ, and R^2 are shown in Fig. 4.12. We can see from Fig. 4.12 (a) that a separation exists between the distribution of the χ^2 statistic and the distribution of the degrees of freedom ν_χ. Furthermore, the mean value of the distribution of the χ^2 statistic is significantly less than the mean value of the ν_χ distribution. Such a separation suggests that the maximum likelihood estimators for the regression

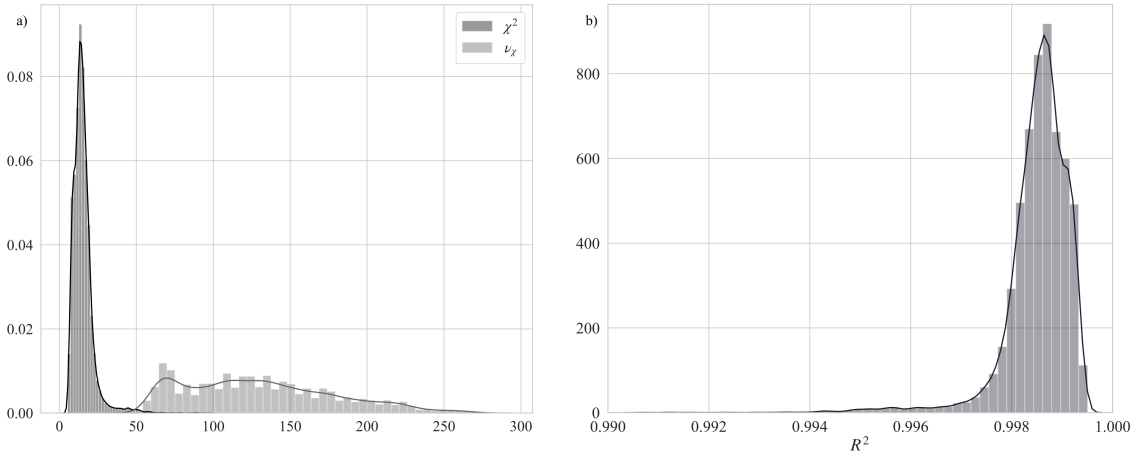

Figure 4.12: Illustration of the statistical relevance of the gravimetric mass flux algorithm. The left sub-plot left (a) depicts distributions of the χ^2 statistic and degrees of freedom ν_χ associated with each fit in this study. The horizontal axis corresponds to the value of both χ^2 and ν_χ, while the vertical axis denotes the probability density. The right sub-plot (b) portrays the probability density of the coefficient of determination R^2.

were statically relevant. Moreover, the peak of the χ^2 distribution is well-defined with a value near ten, while the distribution for the degrees of freedom ν_χ is much broader in comparison with no well-defined peak. However, we would expect a broad distribution in the ν_χ degrees of freedom because, as relative humidity increases, transfer rates decrease with the decreasing driving potentials resulting in longer sampling times to achieve the same χ^2 statistic. Expressly, the algorithm produced a nearly constant χ^2 statistic, which was also independent of the transfer rates and sampling time, further validating our approach. Further supporting the soundness of our regressions, the distribution of the coefficient of determination R^2 has a peak near 0.999, see 4.12. The combination of the characteristics of the χ^2 and R^2 statistics support the statistical relevance of our novel gravimetric regression and suggests that these data are suitable for use in the derivation of mass transfer correlations.

Next, we present data for the calculated Sherwood and Rayleigh numbers from our experiments broken out by ambient temperature and color-coded by relative humidity, see Figure 4.13. As mentioned in §4.2.4, experiments were conducted at six ambient temperatures (285,

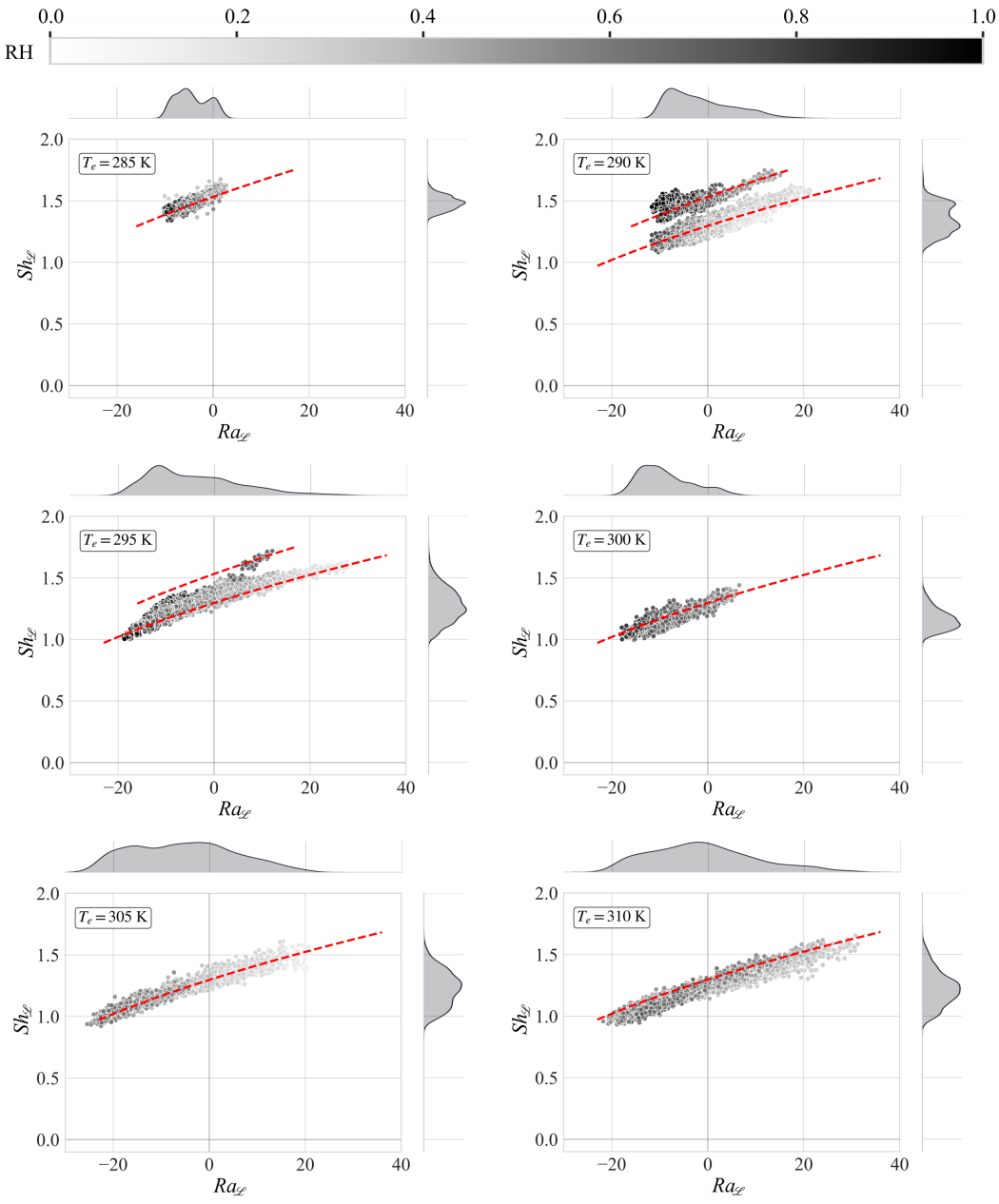

Figure 4.13: Scatter plots for the non-dimensionalized $Sh_{\mathscr{L}}$ – $Ra_{\mathscr{L}}$ data separated by ambient temperature. Each of the six sub-plots contains non-dimensional experimental data from all experiments conducted at a given ambient temperature; each subplot denotes the ambient temperature in the upper left corner of the plot. The horizontal axis denotes $Ra_{\mathscr{L}}$ while the vertical axis indicates $Sh_{\mathscr{L}}$. Furthermore, kernel density estimates of $Sh_{\mathscr{L}}$ and $Ra_{\mathscr{L}}$ appear to the left and above each of the subplots, respectively. Each of the observations is color-coded by relative humidity, with lighter colors corresponding to lower relative humidity and darker colors approaching vapor saturation. Finally, each sub-plot contains one or more experimental power-law fits, see Fig. 4.14.

290, 295, 300, 305, and 310 K) beginning at initially relatively low ambient vapor content with the evaporation from the vessel allowed to increase the ambient relative humidity during experiments. Furthermore, as mentioned at the end of §4.2.2, we have included a prefactor of negative one when ρ_s is less than ρ_e so that transfer rates (*Sh*) increase with density differences (*Ra*). Each subplot shows a scatter plot of the non-dimensionalized mass transfer data ($Sh_{\mathscr{L}}$ — $Ra_{\mathscr{L}}$) color-coded by relative humidity, with lighter colors corresponding to lower relative humidities (higher concentration differences) and darker colors denoting higher relative humidities (lower concentration differences) with the darkest color signifying vapor saturation in the ambient. Kernel density estimates of the Sherwood and Rayleigh numbers at each ambient temperature appear to the right and above each subplot. Red dashed lines appear on each of the plots, which correspond to power laws that we regressed from the data and will discuss in what follows. However, Figure 4.13 possesses several features worth noting before discussing regression results.

First, data presented for experiments performed at ambient temperatures of 290 and 295 K exhibited two distinct branches of data, while all other tests exhibited only a single branch. To distinguish between the two, we denote the branch that exhibits elevated mass transfer rates as the *upper* branch and, by contrast, the branch that exhibits suppressed transfer rates *lower* branch. The upper branch intersects $Ra = 0$ at approximately $Sh_{\mathscr{L}} = 1.5$ while the lower branch intersects $Ra = 0$ at approximately $Sh_{\mathscr{L}} = 1.25$; a difference of nearly 20%. Furthermore, the upper branch was only present in experiments at or below 295 K, while the lower branch was only present in experiments at or above 295 K, suggesting some temperature-driven effect may be responsible for this bifurcation. Finally, in all of the plots in Fig 4.13, we can see that both transfer rates (Sherwood numbers) and driving potentials (Rayleigh numbers) are both inversely proportional to vapor content (relative humidity) at a constant ambient temperature. Again, we expect this because, as vapor content increases, driving potential decreases, and so do transfer rates. The exception is for the data presented for ambient temperatures of 295 and 290 K, for which the upper branch seems to show elevated relative humidity when compared to the same Rayleigh

number on the lower branch. This disjunction in the driving potentials with relative humidity suggests that the two branches exhibit fundamentally distinct transfer processes. The following discussion surrounding the results in these two subplots provides some insight.

At very low relative humidities, the concentration differences dominate, the value of N is less than negative one, and the density is higher at the interface than far away. As a result, we obtain the canonical *contra-flow* pattern with thermal gradients driving a buoyant flow towards the surface while concentration gradients attempt to transport vapor away from the surface. However, the driving potentials, transfer rates, and magnitude of N all decrease with increasing ambient vapor content as liquid evaporates during experiments until the magnitude of N approaches unity. When the magnitude of N is unity, the upwelling concentration potentials no longer dominate and are similar in magnitude to the downwelling thermal potentials. At this point, experimental data shows an increase in driving potentials, manifested as the tendency of the Rayleigh number towards more positive values and transfer rates, i.e., a switch from the lower branch to the upper branch. This increase in transfer rates is associated with a growing dependence on thermal effects, suggesting that the more warm dry air from the ambient is being transferred to the interface as the concentration gradients have diminished.

Finally, we show a bivariate kernel density estimation of all of the experiments from this work in Fig. 4.14. Adhering to the logic of §4.2.4, we seek a power law to fit our data of the form $A(Ra_{\mathscr{L}}+B)^{1/2}$. Specifically, through a minimization of RMSE we found the following correlations for the upper and lower branches, respectively:

$$Sh_{\mathscr{L}}(Ra_{\mathscr{L}}) = 0.206(Ra_{\mathscr{L}}+55.3)^{1/2}, \tag{4.40}$$

$$Sh_{\mathscr{L}}Ra_{\mathscr{L}} = 0.179(Ra_{\mathscr{L}}+52.5)^{1/2}. \tag{4.41}$$

which, appear as solid red lines in Fig. 4.14, and, as mentioned above, are also shown in Fig. 4.13 as dashed red lines. We only added the upper or lower correlations to subplots of Fig. 4.13

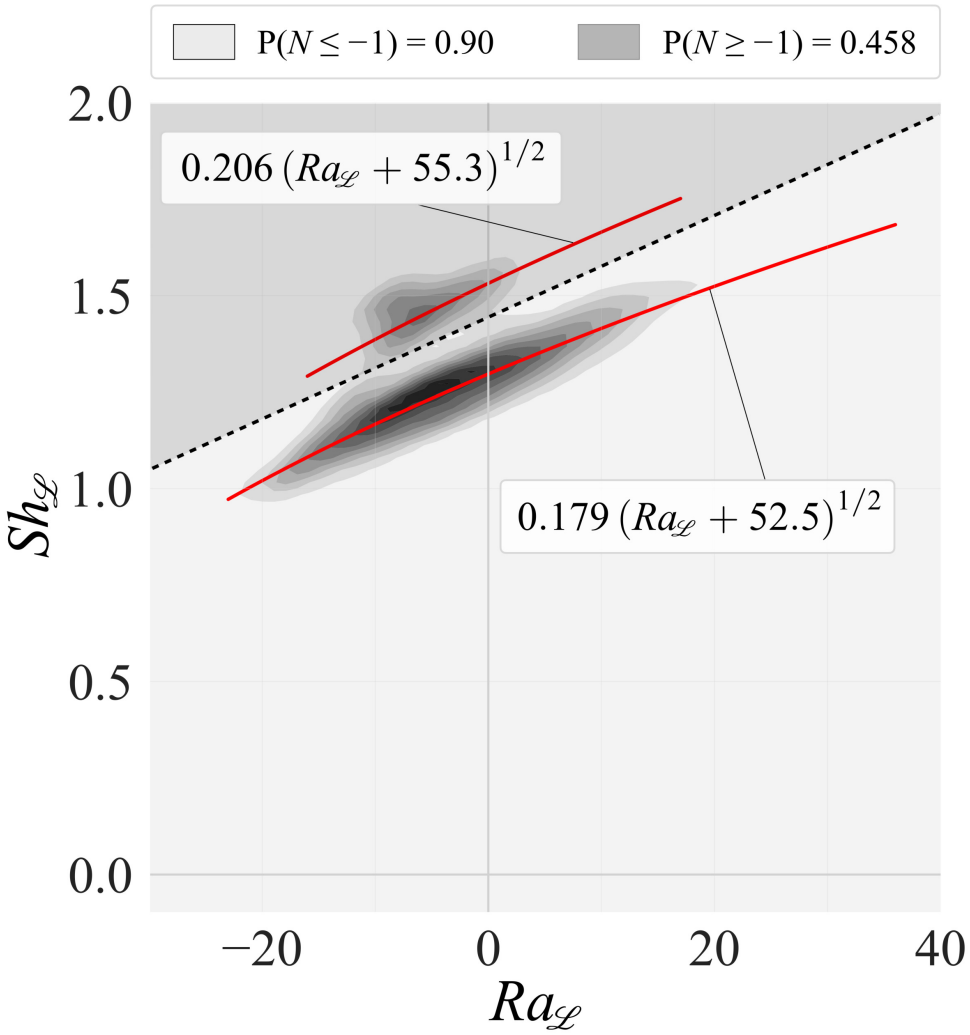

Figure 4.14: Bivariate kernel density estimation of experimental results including experimental power laws and probabilities concerning the magnitude of the N parameter. The horizontal axis denotes $Ra_{\mathscr{L}}$ while the vertical axis denotes $Sh_{\mathscr{L}}$. Darker colors in the shading correspond to a higher density of data. Two power laws appear as red lines. Finally, two regions, divided by a dashed line, indicate conditional probabilities that N is greater than or less than negative one, given that it is present in the given region.

when observations for a given branch were present at a given ambient temperature, which is why some subplots contain a single correlation while others contain two correlations. The scope of the present study limits the application of the upper and lower correlations to $-15 \leq Ra_{\ell} \leq 17$ and $-22 \leq Ra_{\ell} \leq 35$, respectively.

Figure 4.14 also contains two shaded sections separated by a dashed line. The lighter of these two sections correspond to the lower branch, while the darker of the two corresponds to the upper branch. Furthermore, the legend of the figure lists probabilities for the values of N relative to negative one. Explicitly, the shaded regions specify the probability that observations in a region have a value of N that was less than or greater than negative one. As mentioned before, negative one appears because the transfer mechanisms naturally have antithetical orientations when we do not add energy to the liquid during evaporation. This probability adds insight into the expected value of N on a given branch. Specifically, approximately 90% of the lower branch's observations realized values of N that were less than or equal to negative one, meaning that the concentration effects were more substantial in magnitude than the thermal effects. As a result, we are confident that, on the lower branch, the concentration potential is stronger than the temperature potential, even though it is denser at the surface, suggesting some *contra-flow*. On the other hand, nearly half of the upper branch's observations realized values for N that were greater than or equal to negative one. This result again suggests that the thermal potential is beginning to dominate for observations on the upper branch and is responsible for the resulting elevated mass transfer rates.

4.4 Discussion

It is primarily essential to note that we do not believe parallel upward (supercritical) flow occurs for any of the Ra conditions explored, even for positive Ra. In contrast, some may believe that supercritical upward flow occurs in these experiments when $Ra > 0$; this is not the case because the water's surface is always less than the ambient and the density of the mixture is always

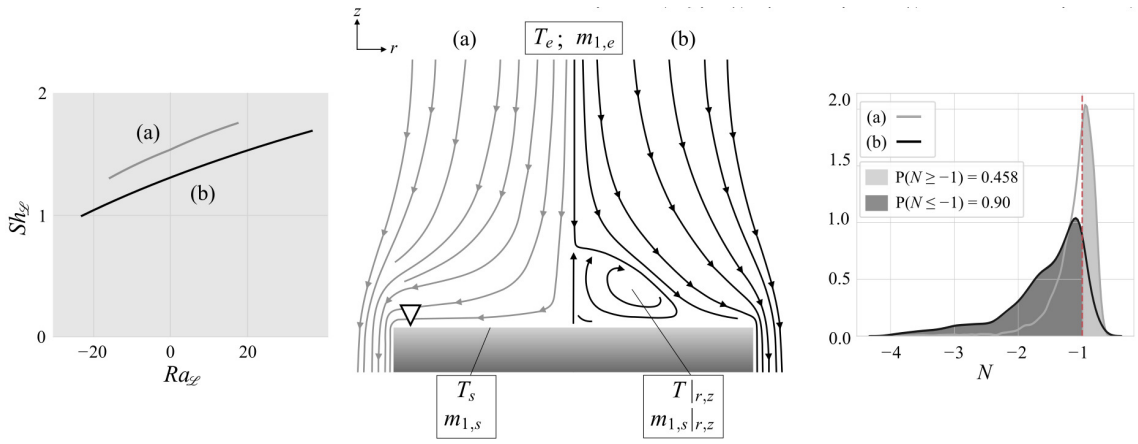

Figure 4.15: Likely flow patterns with associated transfer correlations and distributions of the N parameter. The center illustration contains steady streamlines of two proposed flow regimes above the horizontal air-water interface. The figures on the left and right contain the dimensionless correlations and distributions of the N parameter. The designations (a) and (b) are common across all of the figures. In other words, the gray correlation labeled (a) in the left figure corresponds with the central figure's gray streamlines and, by extension, the lighter correlation in the rightmost figure. The darker illustrations labeled (b) express the same relationships. Finally, we indicate the temperature and concentration at several locations in the center figure to facilitate discussion.

higher at the liquids' surface. While earlier studies [93, 5] suggest, and we found no studies since that refute, that the well studied *contra-flow* pattern, see, Fig. 4.1(b), should persist as the surface temperature approaches the dew point, our results suggest that this is not the case. We observed two distinct, albeit unstable, flow regimes at temperatures between the critical temperature and the dew point. These flow patterns seem to be separated by a dominant mechanism determined by the value of N. The likelihood of either flow pattern to develop depends statistically on the value of N. The observation of more than one possible flow pattern implies that the simple *contra-flow* evaporation pattern alone cannot explain all of the measurements in this study.

As previously mentioned, the *contra-flow* regime dominates the lower branch and results in a flow recirculation near the surface due to the opposing thermal and concentration gradients, as depicted, for example, in Fig. 13 (b). However, the reasons for elevated transfer rates on the upper branch still require some clarification. To that end, we noticed that, on the upper branch, the concentration potentials become negligible, and the flow begins to resemble a purely thermal

flow driven by density differences above an upward-facing cooled plate (see Fig. 13 (a)). The absence of a concentration difference recirculation zone near the surface would explain the shift in the relative humidity values across branches at constant Rayleigh numbers in Fig. 4.13 and the probability of N to approach -1 at the upper branch in Fig. 4.14. In other words, the recirculation zone, Fig. 4.15(b) center, ensures that $T|_{r,z}$ and $m_1|_{r,z}$ are closer to T_s and $m_{1,s}$ than T_e and $m_{1,e}$, respectively, so that overall transfer rates are reduced.

Although the more stable *contra-flow* regime has been reported occasionally in the literature for nearly a century, the absence of the thermally dominated branch (the one that exhibits elevated transfer rates) in the literature is somewhat puzzling. Fig. 4.13 provides a possible reason. Fig. 4.13 illustrates that observation of the upper branch requires simultaneous reduction of ambient temperature and elevation of ambient vapor content relative to laboratory conditions, a set of conditions not achieved in previous experiments. In other words, for air-water pools, observation of transfer rates from natural convection driven by antithetical mechanisms and values of N greater than or equal to -1 requires modification of the far-stream conditions rather than modification of the length scale at repeated temperatures and driving potentials.

The flow regimes described here are particularly relevant to length scales and thermodynamic conditions often found in laboratory, household, and industrial settings. For example, the Rayleigh numbers covered in this study apply directly to glass topped with water left to evaporate under normal conditions of temperature and pressure (NCTP).

4.5 Conclusions

We developed a methodology to measure in-situ evaporation rates at water-air interfaces under controlled conditions for low Grashof number. Dimensionless correlations were proposed for the two distinct flow pattenr branches under consideration. Results for different relative humidity values at a given Rayleigh number suggest that elevated concentration gradients exist

on the upper branch with respect to the lower branch (all else being equal). Furthermore, the probability that concentration differences on the lower branch dominate the process is near 90%. In contrast, the upper branch has a probability distribution for N centered near negative one, further suggesting that the transition to elevated transfer rates may be related to the diminishing concentration differences as relative humidity values increase. The previous discussion points to a stable recirculation zone above the interface on the lower branch. This recirculation zone effectively shields the interface from the drier ambient air. However, once N approaches the value of -1, concentration differences decrease for elevated relative humidity values, and the flow stabilizes as a purely thermal flow with no recirculation zone, resulting in increased gradients and elevated transfer rates. Because mass transfer at low Rayleigh numbers is driven by relatively weak and competing transport mechanisms, the sensitivity to the onset of recirculation zones creates a complex interplay of weak driving potentials. The complex interplay of these weak driving potentials occurs frequently for water evaporation in air under lower-tropospheric conditions.

4.6 Acknowledgement

This chapter, in full, is in preparation as a manuscript for publication with my co-author Jéssica P. T. Medrado and advisor Professor Carlos F. M. Coimbra. The dissertation author is also the first author of this paper.

Appendix A

Remote sensing with AQUA and TERRA

While it is true that remote sensing techniques, such as MODIS onboard NASA's AQUA and TERRA, provide global maps of aerosol optical depth, this does not invalidate the determination of Linke turbidity from ground-based DNI observations. Due to the PLEO of the AQUA and TERRA satellites, they only pass over a given location up to four times a day. Typically half of these occur during the night, leaving only two passes per day for a given location. However, during partly cloudy days, there is no guarantee that the satellite will pass over the location during a clear portion of the day. For that reason, we performed a case study to investigate the probability of a satellite missing an opportunity to sample a clear-sky portion of the day. The question of how likely was it that the circumsolar region was clear (from a ground-based radiometer) before or after a satellite passed over a location and observed cloud cover on the same day. It is important to note here that the extent of the cloud cover is not known. While cloud contamination exists (to some extent) in all of the satellites 'missed' passes, final AOD retrievals from MODIS are typically spatially relaxed (-1° $\times$ 1°), which may solve the issue in cases when the cloud field had a limited horizontal extent.

To provide a lower bound on the probability that a satellite observation would contain cloud cover on a partly clear day, we used data from Folsom as a result of the high fraction of

Table A.1: Table showing the number of total passes for both the AQUA and TERRA satellites for the twelve months spanning May 2013 to May 2014. We subdivided passes into daytime observations and the fraction of the daytime observations that were not clear but occurred on days that ground-based sensing techniques obtained a clear observation either before or after the satellite's pass occurred.

	AQUA	TERRA	Total
Total passes	1495	1502	2997
Night passes (total)	750 (50%)	753 (50%)	1503 (50%)
Day passes (total)	745 (50%)	749 (50%)	1494 (50%)
Clear passes (day)	397 (53%)	407 (54%)	804 (54%)
Not clear passes (day)	348 (47%)	342 (46%)	690 (46%)
Missed clear passes (not clear, day)	166 (48%, 22%)	205 (60%, 27%)	371 (54/%, 25%)

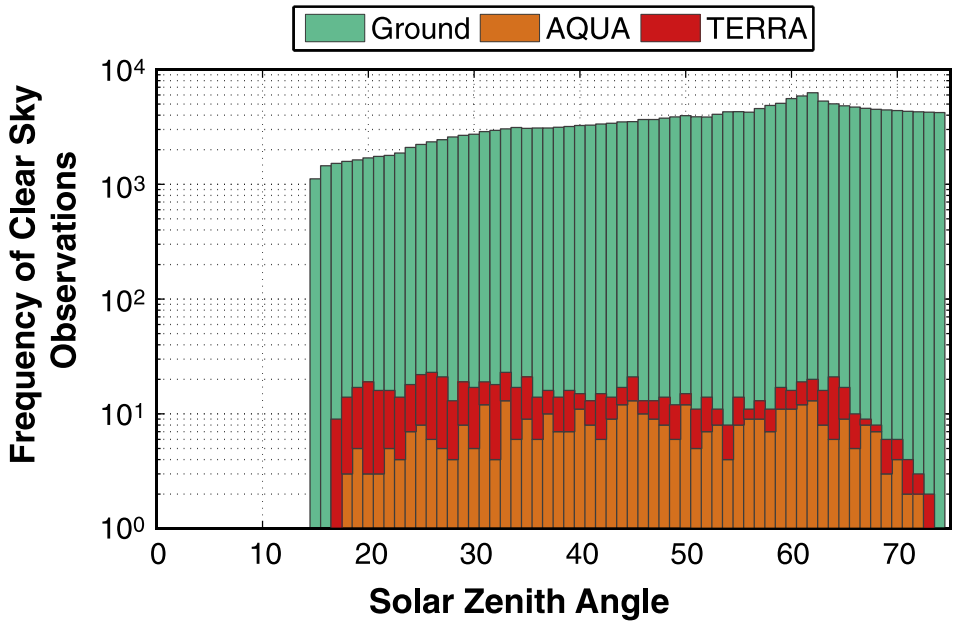

Figure A.1: Histogram showing the raw number of clear-sky observations for the twelve months spanning May 2013 to May 2014. The number of samples achieved by ground sensing techniques was three orders of magnitude larger than remote sensing techniques.

clear-sky observations. We used information regarding the satellite's orbit to calculate when a satellite passed over Folsom and then used the endogenous clear-sky detection algorithm to determine if the entire pass was clear. We present the statistics for the AQUA and TERRA satellites from May 2013 to May 2014 in Table A.1. The histogram of the number of clear-sky observations for both the ground-based sensing and remote sensing is shown in Fig. A.1. It is clear from Table A.1 that the AQUA and TERRA satellites miss the opportunity to sample a clear window in a day nearly 50% of the time that the day was partly cloudy or about 25% of all of its passes. Also, the number of clear-sky observations the ground-based methodology recorded was larger than the remote sensing techniques by three orders of magnitude, suggesting a much more robust sampling of atmospheric turbidity.

Appendix B

Original Correlations

Previous studies have employed various length scales in their definitions of dimensionless parameters used in correlations. This disparity highlights the need for a geometry independent length scale to compare results. The choice of length scale affects both the coefficient for a given correlation as well as the applicable range of Rayleigh numbers. Table 4.1 lists all the correlations' coefficients and applicable Rayleigh ranges using the geometry independent length scale $\mathscr{L}$. However, the original forms of the correlations are listed here for the readers' convenience. The following definitions were used to transform correlations between Table 4.1 and Table B.1: i) $Sh_W = 4Sh_{\mathscr{L}}$, ii) $Ra_W = 64Ra_{\mathscr{L}}$, iii) $Sh_D = 4Sh_{\mathscr{L}}$, iv) $Ra_W = 64Ra_{\mathscr{L}}$, v)$Sh_R = 2Sh_{\mathscr{L}}$, and vi) $Ra_R = 8Sh_{\mathscr{L}}$, where W is the length of a side of a square, D is the diameter of a circle, R is the radius of a circle, and $\mathscr{L} = A/P$ is the geometry independent length scale used in this study.

Table B.1: Comparison of $Sh - Ra$ power law coefficients and exponents from previous experimental studies. While not all of the original studies listed used the length scale $\mathscr{L}$, see Eqn. (4.9) we have, where necessary, scaled the coefficients accordingly. This conversion allows a unified comparison of previous results, regardless of the geometry of the employed interface. For consistency, in some cases, a constant factor of $Sc^{1/3} = 0.61^{1/3}$ is also absorbed into the numerical coefficient. The present work is excluded from this table because here we attempt to find a single correlation for a non-zero value of Sh that crosses the $Ra = 0$ value, and as a result, the form of the correlation in this regime requires an additional term. Specifically, $Sh(Ra) = B(Ra + C)^n)$, where we have added the offset C, see Eqn. 4.39

Parameterization	$Sh_{L_c} = A\,Ra_{L_c}$				
	A	n	Sc	L_c	Ra_{L_c} range
1. Fishenden and Saunders [91]	0.14	1/3	0.6	W	$2\times10^7 < Ra_W < 3\times10^{10}$
2. Sharpley and Boelter [93]	0.892	0.213	0.6	D	$10^6 < Ra_D < 4.5\times10^7$
3. Boelter et al. [5]	0.544	0.241	0.6	D	$9.3\times10^6 < Ra_D < 4.6\times10^8$
4. Goldstein et al. [96]	0.590	1/4	2.5	$\mathscr{L}$	$2.0\times10^2 < Ra_{\mathscr{L}} < 5.0\times10^3$
5. Goldstein et al. [96]	0.960	1/6	2.5	$\mathscr{L}$	$1.0 < Ra_{\mathscr{L}} < 90$
6. Lloyd and Moran [99]	0.150	1/3	2200	$\mathscr{L}$	$8.0\times10^6 < Ra_{\mathscr{L}} < 1.6\times10^9$
7. Lloyd and Moran [99]	0.540	1/4	2200	$\mathscr{L}$	$2.2\times10^4 < Ra_{\mathscr{L}} < 8.0\times10^6$
8. Sparrow et al. [100]	0.645	0.205	0.6	R	$2\times10^4 < Ra_R < 9\times10^5$
9. Bower and Saylor [101, 102]	0.267	0.306	0.6	W	$9.6\times10^5 < Ra_W < 5.7\times10^8$
10. Radziemska and Lewandowski [104]	0.675	1/5	0.6	R	$2\times10^4 < Ra_R < 3\times10^7$

Bibliography

[1] K. K. Steincke, *Farvel Og Tak: Minder Og Meninger, (Farvel Og tak: Ogsaa en Tilvaerelse IV (1935-1939)), Quote Page 227.* København: Forlaget Fremad, 1948.

[2] R. H. Inman, J. G. Edson, and C. F. M. Coimbra, "Impact of local broadband turbidity estimation on forecasting of clear sky direct normal irradiance," *Solar Energy*, vol. 117, p. 125–138, 2015.

[3] J. Remund, L. Wald, M. Lefèvre, and T. Ranchin, "Worldwide Linke turbidity information," in *Prodeedings of ISES Solar World Congress*, 2003.

[4] J. Remund and J. Page, "Advanced Parameters WP 5.2b: Chain of Algorithms: Short- and Longwave Radiation with Associated Temperature Prediction Resources," *Technical Report, SoDa Deliverables*, vol. D5-2-2/3, 2002.

[5] L. M. K. Boelter, H. S. Gordon, and J. R. Griffin, "Free evaporation into air of water from a free horizontal quiet surface," *Industrial & Engineering Chemistry*, vol. 38, no. 6, p. 596–600, 1946.

[6] M. Reno and C. Hansen, "Identification of periods of clear sky irradiance in time series of GHI measurements," *Renewable Energy*, 2016.

[7] R. H. Inman, H. T. C. Pedro, and C. F. M. Coimbra, "Solar forecasting methods for renewable energy integration," *Progress in Energy and Combustion Science*, vol. 39, no. 6, p. 535–576, 2013.

[8] D. Yang, J. Kleissl, C. Gueymard, H. Pedro, and C. Coimbra, "History and trends in solar irradiance and pv power forecasting: A preliminary assessment and review using text mining," *Solar Energy*, vol. 168, p. 60–101, 2018.

[9] C. Analytics, "Web of science: Clarivate analytics," 2021. https://app.webofknowledge.com.

[10] C. A. Gueymard, "Clear-sky irradiance predictions for solar resource mapping and large-scale applications: Improved validation methodology and detailed performance analysis of 18 broadband radiative models," *Solar Energy*, vol. 86, no. 8, p. 2145–2169, 2012.

[11] Y. A. Eltbaakh, M. H. Ruslan, M. A. Alghoul, M. Y. Othman, and K. Sopian, "Issues concerning atmospheric turbidity indices," *Renewable and Sustainable Energy Reviews*, vol. 16, no. 8, p. 6285–6294, 2012.

[12] "Solar energy services for professionals." http://www.soda-pro.com/help/general-knowledge/linke-turbidity-factor, 2022.

[13] M. Lefèvre, L. Albuisson, and L. Wald, "Joint Report on Interpolation Scheme "Meteosat and Database" Climatology I (Meteosat)," *Technical Report, SoDa Deliverables*, vol. D3-8; D5-1-4, 2004.

[14] "Ivanpah Solar Electric Generating System." http://ivanpahsolar.com/, 2017.

[15] A. Krizhevsky, I. Sutskever, and G. E. Hinton, "Imagenet classification with deep convolutional neural networks," *Communications of the ACM*, vol. 60, no. 6, p. 84–90, 2017.

[16] G. Kopp and J. L. Lean, "A new, lower value of total solar irradiance: Evidence and climate significance," *Geophysical Research Letters*, vol. 38, no. 1, 2011.

[17] R. H. Inman, Y. Chu, and C. F. Coimbra, "Cloud enhancement of global horizontal irradiance in california and hawaii," *Solar Energy*, vol. 130, p. 128–138, 2016.

[18] "Noaa earth system research laboratory: Surface radiation budget (surfrad) network observations." https://gml.noaa.gov/grad/surfrad/, 2018.

[19] K. Young and E. Tomlinson, "Microphysical Effects of Irradiated Fog with a 10.6-μ CO_2 Laser," *Journal of the Atmospheric Sciences*, vol. 50, no. 7, pp. 941–950, 1993.

[20] M. T. Tyszkiewicz and S. Daggett, "Turboclair Fog Dispersal Method: Development and Testing of Underground Blower Unit (1965-1969)," *U.S. Defense Technical Information Center*, vol. AD0711605, pp. 1–72, 1998.

[21] E. Walker and D. Fox, "The dispersal of fog from airport runways, a record of work of technical branch f of the petroleum warfare department 1942-1946," *Ministry of Supply, London*, p. 321, 1946.

[22] E. Walker and D. Fox, "Fog Dissipation using a CO_2 Laser," *Applied Physics Letters*, vol. 13, no. 4, pp. 145–147, 1968.

[23] V. O.A., Y. A. Sedunov, and L. Semenov, *Propagation of Intensive Laser Radiation in Clouds*. Washington, DC: American Institute of Aeronautics and Astronautics, 1992.

[24] E. Caramana, R. Webster, G. Quigley, and R. Morse, "Theoretical and Experimental Studies of CO_2 Laser Evaporation of Clouds," *Journal of Applied Physics*, vol. 70, no. 8, pp. 4601–4616, 1991.

[25] M. Q. Brewster, "Water Evaporation and Condensation in Air With Radiation: The Self-Similar Spalding Model," *Journal of Heat Transfer*, vol. 139, pp. 081501–1, 2017.

[26] M. Q. Brewster, "Evaporation and condensation of water mist/cloud droplets with thermal radiation," *International Journal of Heat and Mass Transfer*, vol. 88, pp. 695–712, 2015.

[27] H. Bahar and P. Bojek, *IEA (2020), Concentrating Solar Power (CSP)*. International Energy Agency, 2020.

[28] C. S. Wen, *The fundamentals of aerosol dynamics*. River Edge, NJ: World Scientific, 1996.

[29] J.-J. Morcrette, O. Boucher, L. Jones, D. Salmond, P. Bechtold, A. Beljaars, A. Benedetti, A. Bonet, J. W. Kaiser, M. Razinger, M. Schulz, S. Serrar, A. J. Simmons, M. Sofiev, A. M. Tompkins, and A. Untch, "Aerosol analysis and forecast in the european centre for medium-range weather forecasts integrated forecast system: Forward modeling," *Journal of Geophysical Research*, vol. 114, no. D6, 2009.

[30] D. G. Kaskaoutis and H. D. Kambezidis, "Comparison of the ångström parameters retrieval in different spectral ranges with the use of different techniques," *Meteorology and Atmospheric Physics*, vol. 99, no. 3-4, p. 233–246, 2007.

[31] M. Chin, P. Ginoux, S. Kinne, O. Torres, B. N. Holben, B. N. Duncan, R. V. Martin, J. A. Logan, A. Higurashi, and T. Nakajima, "Tropospheric aerosol optical thickness from the GOCART model and comparisons with satellite and sun photometer measurements," *Journal of the Atmospheric Sciences*, vol. 59, no. 3, p. 461–483, 2002.

[32] A. Louche, G. Peri, and M. Iqbal, "An analysis of linke turbidity factor," *Solar Energy*, vol. 37, no. 6, p. 393–396, 1986.

[33] C. Gueymard and F. Vignola, "Determination of atmospheric turbidity from the diffuse-beam broadband irradiance ratio," *Solar Energy*, vol. 63, no. 3, p. 135–146, 1998.

[34] J. Cañada, J. M. Pinazo, and J. V. Bosca, "Determination of ångströms turbidity coefficient at Valencia," *Renewable Energy*, vol. 3, no. 6-7, p. 621–626, 1993.

[35] P. Ineichen, "Conversion function between the Linke turbidity and the atmospheric water vapor and aerosol content," *Solar Energy*, vol. 82, no. 11, p. 1095–1097, 2008.

[36] J. Polo, L. F. Zarzalejo, L. Martín, A. A. Navarro, and R. Marchante, "Estimation of daily Linke turbidity factor by using global irradiance measurements at solar noon," *Solar Energy*, vol. 83, no. 8, p. 1177–1185, 2009.

[37] C. Gueymard, "Aerosol turbidity derivation from broadband irradiance measurements: Methodological advances and uncertainty analysis," in *Solar 2013, American Solar Energy Society*, 01 2013.

[38] C. A. Gueymard, "Impact of on-site atmospheric water vapor estimation methods on the accuracy of local solar irradiance predictions," *Solar Energy*, vol. 101, p. 74–82, 2014.

[39] J. Bilbao, R. Román, and A. Miguel, "Turbidity coefficients from normal direct solar irradiance in Central Spain," *Atmospheric Research*, vol. 143, p. 73–84, 2014.

[40] M. Masmoudi, M. Chaabane, K. Medhioub, and F. Elleuch, "Variability of aerosol optical thickness and atmospheric turbidity in Tunisia," *Atmospheric Research*, vol. 66, no. 3, p. 175–188, 2003.

[41] J. A. Ruiz-Arias, J. Dudhia, C. A. Gueymard, and D. Pozo-Vázquez, "Assessment of the Level-3 MODIS daily aerosol optical depth in the context of surface solar radiation and numerical weather modeling," *Atmospheric Chemistry and Physics*, vol. 13, p. 675–692, 2013.

[42] M. H. Unsworth and J. L. Monteith, "Aerosol and solar radiation in britain," *Quarterly Journal of the Royal Meteorological Society*, vol. 98, pp. 778–797, 1972.

[43] F. Linke, "Transmission-koefficient und trübungsfaktor," *Phys. fr. Atmos.*, vol. 10, pp. 91–103, 1922.

[44] F. Linke, "Messungen der sonnenstrahlung beivier freiballonlahrten," *Beitr. Phys. fr. Atmos.*, vol. 15, p. 176, 1929.

[45] C. A. Gueymard, "Turbidity Determination from Broadband Irradiance Measurements: A Detailed Multicoefficient Approach," *Journal of Applied Meteorology*, vol. 37, no. 4, p. 414–435, 1998.

[46] P. Ineichen and R. Perez, "A new airmass independent formulation for the Linke turbidity coefficient," *Solar Energy*, vol. 73, no. 3, p. 151–157, 2002.

[47] J. Page, "Algorithms for the Satel-Light programme," *Technical Report, Satel-Light*, 1996.

[48] D. Dumortier, "Monitoring clobal and diffuse horizontal irradiances under cloudless skies with different turbidities," *Technical Report, Daylight II Project*, vol. JOU2-CT92-0144, 1995.

[49] C. Rigollier, O. Bauer, and L. Wald, "On the clear sky model of the ESRA — European Solar Radiation Atlas — with respect to the heliosat method," *Solar Energy*, vol. 68, no. 1, p. 33–48, 2000.

[50] R. Perez, P. Ineichen, K. Moore, M. Kmiecik, C. Chain, R. George, and F. Vignola, "A new operational model for satellite-derived irradiances: description and validation," *Solar Energy*, vol. 73, no. 5, p. 307–317, 2002.

[51] M. Schroedter-Homscheidt and A. Oumbe, "Validation of an hourly resolved global aerosol model in answer to solar electricity generation information needs," *Atmospheric Chemistry and Physics Discussions*, vol. 12, no. 12, p. 31917–31953, 2012.

[52] V. Lara-Fanego, J. A. Ruiz-Arias, D. Pozo-Vázquez, F. J. Santos-Alamillos, and J. Tovar-Pescador, "Evaluation of the WRF model solar irradiance forecasts in Andalusia (southern Spain)," *Solar Energy*, vol. 86, no. 8, p. 2200–2217, 2012.

[53] R. Marquez and C. F. M. Coimbra, "Forecasting of global and direct solar irradiance using stochastic learning methods, ground experiments and the NWS database," *Solar Energy*, vol. 85, no. 5, p. 746–756, 2011.

[54] C. A. Gueymard, "Temporal variability in direct and global irradiance at various time scales as affected by aerosols," *Solar Energy*, vol. 86, no. 12, p. 3544–3553, 2012.

[55] P. Ineichen, "Comparison of eight clear sky broadband models against 16 independent data banks," *Solar Energy*, vol. 80, no. 4, p. 468–478, 2006.

[56] Y. A. Eltbaakh, M. H. Ruslan, M. A. Alghoul, M. Y. Othman, and K. Sopian, "Issues concerning atmospheric turbidity indices," *Renewable and Sustainable Energy Reviews*, vol. 16, no. 8, p. 6285–6294, 2012.

[57] F. Kasten, "A simple parameterization of two pyrheliometric formulae for determining the Linke turbidity factor," *Meteor. Rdcsh.*, vol. 33, pp. 124–127, 1980.

[58] K. Feussner and P. Dubois, "Trübungsfaktor, precipitable water," *Staub. Gerlands Beitr. Geophys.*, vol. 27, pp. 132–175, 1930.

[59] F. Kasten, "Parametriesierung der globalstrahlung durch bedekungsgrad und trübungsfaktor," *Annalen der Meteorol. Neue Folge*, vol. 20, pp. 49–50, 1984.

[60] A. Gueymard, C and D. R. Myers, "Evaluation of conventional and high-performance routine solar radiation measurements for improved solar resource, climatological trends, and radiative modeling," *Solar Energy*, vol. 83, no. 2, p. 171–185, 2009.

[61] C. N. Long and T. P. Ackerman, "Identification of clear skies from broadband pyranometer measurements and calculation of downwelling shortwave cloud effects," *Journal of Geophysical Research: Atmospheres*, vol. 105, no. D12, p. 15609–15626, 2000.

[62] A. Smirnov, B. N. Holben, T. F. Eck, O. Dubovik, and I. Slutsker, "Cloud-screening and quality control algorithms for the AERONET database," *Remote Sensing of Environment*, vol. 73, no. 3, p. 337–349, 2000.

[63] T. E. Hoff, R. Perez, J. Kleissl, D. Renne, and J. Stein, "Reporting of irradiance modeling relative prediction errors," *Progress in Photovoltaics: Research and Applications*, vol. 21, no. 7, p. 1514–1519, 2012.

[64] R. Tapakis and A. G. Charalambides, "Enhanced values of global irradiance due to the presence of clouds in Eastern Mediterranean," *Renewable Energy*, vol. 62, p. 459–467, 2014.

[65] R. M. Goody and Y. L. Yung, *Atmospheric radiation: theorical basis*. New-York: Oxford university press, 1995.

[66] N. H. Schade, A. Macke, H. Sandmann, and C. Stick, "Enhanced solar global irradiance during cloudy sky conditions," *Meteorologische Zeitschrift*, vol. 16, no. 3, p. 295–303, 2007.

[67] G. A. Franceschini, "The influence of clouds on solar radiation at sea," *Deutsche Hydrographische Zeitschrift*, vol. 21, no. 4, p. 162–168, 1968.

[68] G. Wen, R. F. Cahalan, S. Tsay, and L. Oreopoulos, "Impact of cumulus cloud spacing on landsat atmospheric correction and aerosol retrieval," *Journal of Geophysical Research: Atmospheres*, vol. 106, no. D11, p. 12129–12138, 2001.

[69] K. Wyser, W. Ohirok, C. Gautier, and C. Jones, "Remote sensing of surface solar irradiance with corrections for 3-D cloud effects," *Remote Sensing of Environment*, vol. 80, no. 2, p. 272–284, 2002.

[70] G. Pfister, R. L. Mckenzie, J. B. Liley, A. Thomas, B. W. Forgan, and C. N. Long, "Cloud coverage based on all-sky imaging and its impact on surface solar irradiance," *Journal of Applied Meteorology*, vol. 42, no. 10, p. 1421–1434, 2003.

[71] P. Emck and M. Richter, "An upper threshold of enhanced global shortwave irradiance in the troposphere derived from field measurements in tropical mountains," *Journal of Applied Meteorology and Climatology*, vol. 47, no. 11, p. 2828–2845, 2008.

[72] L. K. Berg, E. I. Kassianov, C. N. Long, and D. L. Mills, "Surface summertime radiative forcing by shallow cumuli at the Atmospheric Radiation Measurement Southern Great Plains site," *Journal of Geophysical Research*, vol. 116, no. D1, 2011.

[73] P. G. Mccormick and H. Suehrcke, "Cloud-reflected radiation," *Nature*, vol. 345, no. 6278, p. 773–773, 1990.

[74] J. Luoma, J. Kleissl, and K. Murray, "Optimal inverter sizing considering cloud enhancement," *Solar Energy*, vol. 86, no. 1, p. 421–429, 2012.

[75] N. Kawasaki, T. Oozeki, K. Otani, and K. Kurokawa, "An evaluation method of the fluctuation characteristics of photovoltaic systems by using frequency analysis," *Solar Energy Materials and Solar Cells*, vol. 90, no. 18-19, p. 3356–3363, 2006.

[76] M. Hazewinkel, *Daubechies Wavelets*. Springer Science & Business Media, 2001.

[77] A. Woyte, R. Belmans, and J. Nijs, "Fluctuations in instantaneous clearness index: Analysis and statistics," *Solar Energy*, vol. 81, no. 2, p. 195–206, 2007.

[78] A. Haar, "Zur theorie der orthogonalen funktionensysteme," *Math. Ann.*, vol. 71, no. 1, pp. 38–53, 1911.

[79] O. Perpiñán and E. Lorenzo, "Analysis and synthesis of the variability of irradiance and PV power time series with the wavelet transform," *Solar Energy*, vol. 85, no. 1, p. 188–197, 2011.

[80] O. Perpiñán, J. Marcos, and E. Lorenzo, "Electrical power fluctuations in a network of DC/AC inverters in a large PV plant: Relationship between correlation, distance and time scale," *Solar Energy*, vol. 88, p. 227–241, 2013.

[81] M. Lave, J. Kleissl, and E. Arias-Castro, "High-frequency irradiance fluctuations and geographic smoothing," *Solar Energy*, vol. 86, no. 8, p. 2190–2199, 2012.

[82] M. Lave, J. Kleissl, and J. S. Stein, "A Wavelet-Based Variability Model (WVM) for solar PV power plants," *IEEE Transactions on Sustainable Energy*, vol. 4, no. 2, p. 501–509, 2013.

[83] A. Peled and J. Appelbaum, "Evaluation of solar radiation properties by statistical tools and wavelet analysis," *Renewable Energy*, vol. 59, p. 30–38, 2013.

[84] M. Segal and J. Davis, "The impact of deep cumulus reflection on the ground-level global irradiance," *Journal of Applied Meteorology*, vol. 31, no. 2, p. 217–222, 1992.

[85] A. Cede, M. Blumthaler, E. Luccini, R. D. Piacentini, and L. Nuñez, "Effects of clouds on erythemal and total irradiance as derived from data of the Argentine Network," *Geophysical Research Letters*, vol. 29, no. 24, 2002.

[86] G. H. Yordanov, O. Midtgard, T. O. Saetre, H. K. Nielsen, and L. E. Norum, "Overirradiance (cloud enhancement) events at high latitudes," *2012 IEEE 38th Photovoltaic Specialists Conference (PVSC) PART 2*, 2013.

[87] G. H. Yordanov, T. O. Saetre, and O. Midtgard, "100-millisecond resolution for accurate overirradiance measurements," *IEEE Journal of Photovoltaics*, vol. 3, no. 4, p. 1354–1360, 2013.

[88] M. P. Almeida, R. Zilles, and E. Lorenzo, "Extreme overirradiance events in São Paulo, Brazil," *Solar Energy*, vol. 110, p. 168–173, 2014.

[89] S. G. Mallat, *A wavelet tour of signal processing*. Amsterdam: Academic Press, 2009.

[90] E. Kassianov, C. N. Long, and M. Ovtchinnikov, "Cloud Sky Cover versus Cloud Fraction: Whole-Sky Simulations and Observations," *Journal of Applied Meteorology*, vol. 44, no. 1, p. 86–98, 2005.

[91] M. W. Fishenden and O. A. Saunders, *An Introduction to Heat Transfer*, pp. 95–97. London: Oxford, Clarendon Press, 1950.

[92] W. H. McAdams, *Heat transmission*. McGraw-Hill, 1954.

[93] B. F. Sharpley and L. M. K. Boelter, "Evaporation of water into quiet air from a one-foot diameter surface," *Industrial & Engineering Chemistry*, vol. 30, no. 10, p. 1125–1131, 1938.

[94] R. Husar and E. Sparrow, "Patterns of free convection flow adjacent to horizontal heated surfaces," *International Journal of Heat and Mass Transfer*, vol. 11, no. 7, p. 1206–1208, 1968.

[95] M. Mikheyev, *Fundamentals of Heat Transfer*, pp. 77–78. Moscow: Peace Publishers, 1968.

[96] R. Goldstein, E. Sparrow, and D. Jones, "Natural convection mass transfer adjacent to horizontal plates," *International Journal of Heat and Mass Transfer*, vol. 16, no. 5, p. 1025–1035, 1973.

[97] A. Wragg, "Free convection mass transfer at horizontal electrodes," *Electrochimica Acta*, vol. 13, no. 12, p. 2159–2165, 1968.

[98] A. Wragg and R. Loomba, "Free convection flow patterns at horizontal surfaces with ionic mass transfer," *International Journal of Heat and Mass Transfer*, vol. 13, no. 2, p. 439–442, 1970.

[99] J. R. Lloyd and W. R. Moran, "Natural convection adjacent to horizontal surface of various planforms," *Journal of Heat Transfer*, vol. 96, p. 443–447, Jan 1974.

[100] E. M. Sparrow, G. K. Kratz, and M. J. Schuerger, "Evaporation of water from a horizontal surface by natural convection," *Journal of Heat Transfer*, vol. 105, p. 469–475, Jan 1983.

[101] S. Bower and J. Saylor, "A study of the sherwood–rayleigh relation for water undergoing natural convection-driven evaporation," *International Journal of Heat and Mass Transfer*, vol. 52, no. 13-14, p. 3055–3063, 2009.

[102] S. Bower and J. Saylor, "Erratum to "a study of the sherwood–rayleigh relation for water undergoing natural convection-driven evaporation" [int. j. heat mass transfer 52 (2009) 3055–3063]," *International Journal of Heat and Mass Transfer*, vol. 54, no. 1-3, p. 749, 2011.

[103] F. Tetsu, H. Hiroshi, and M. Itsuki, "A theoretical study of natural convection heat transfer from downward-facing horizontal surfaces with uniform heat flux," *International Journal of Heat and Mass Transfer*, vol. 16, no. 3, p. 611–627, 1973.

[104] E. Radziemska and W. Lewandowski, "Heat transfer by natural convection from an isothermal downward-facing round plate in unlimited space," *Applied Energy*, vol. 68, no. 4, p. 347–366, 2001.

[105] D. Spalding, "A standard formulation of the steady convective mass transfer problem," *International Journal of Heat and Mass Transfer*, vol. 1, no. 2-3, p. 192–207, 1960.

[106] M. Q. Brewster, "Evaporation of water at high mass-transfer rates by natural convection air flow with application to spent-fuel pools," *International Journal of Heat and Mass Transfer*, vol. 116, p. 703–714, 2018.

[107] E. Fenech and C. Tobias, "Mass transfer by free convection at horizontal electrodes," *Electrochimica Acta*, vol. 2, no. 4, p. 311–325, 1960.

[108] L. Pera and B. Gebhart, "Natural convection flows adjacent to horizontal surfaces resulting from the combined buoyancy effects of thermal and mass diffusion," *International Journal of Heat and Mass Transfer*, vol. 15, no. 2, pp. 269–278, 1972.

[109] U. C. on Extension to the Standard Atmosphere, *U.S. standard atmosphere, 1976*. Washington, D.C.: U.S. G.P.O., 1977.

[110] R. C. L. Bosworth, *Heat Transfer Phenomena*, pp. 102–104. New York: John Wiley, 1952.

[111] J. Boussinesq, *Théorie analytique de la chaleur*, vol. 2. Paris: Gauthier-Villars, 1903.

[112] B. Gebhart, Y. Jaluria, R. L. Mahajan, and B. Sammakia, *Buoyancy-induced flows and transport*. Cambridge: Hemisphere, 1988.

[113] A. F. Mills and C. Coimbra, *Basic heat and mass transfer*. San Diego, CA: Temporal Publishing, 2015.

[114] G. Mcbain, H. Suehrcke, and J. Harris, "Evaporation from an open cylinder," *International Journal of Heat and Mass Transfer*, vol. 43, no. 12, p. 2117–2128, 2000.

[115] D. York, "Least-squares fitting of a straight line," *Canadian Journal of Physics*, vol. 44, no. 5, p. 1079–1086, 1966.

[116] K. Thirumalai, A. Singh, and R. Ramesh, "A matlab^{TM} code to perform weighted linear regression with (correlated or uncorrelated) errors in bivariate data," *Journal of the Geological Society of India*, vol. 77, no. 4, p. 377–380, 2011.

[117] E. O. Lebigot, "Uncertainties: a Python package for calculations with uncertainties," 2010–. [Online; accessed 26 Nov. 2018].

[118] A. H. P. Skell and A. R. H. Cornish, "Mass transfer from spheroids to an air stream," *AIChE Journal*, vol. 9, no. 1, pp. 73–76, 1963.

[119] J. H. Masliyah and N. Epstein, "Numerical solution of heat and mass transfer from spheroids in steady axisymmetric flow," in *Proceedings of the International Symposium on Two-Phase Systems*, pp. 613–632, Pergamon, 1972.